

POSITION/FORCE CONTROL OF MANIPULATORS  
USED FOR DEBURRING AND GRINDING

By

DULI HONG

Diploma

Nanjing Navigation Engineering College

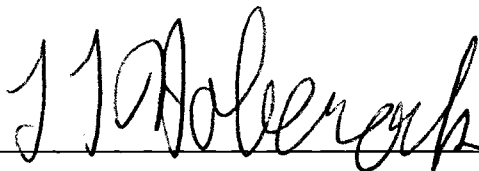
Nanjing, China

1982


Submitted to the Faculty of the  
Graduate College of the  
Oklahoma State University  
in partial fulfillment of  
the requirements for  
the Degree of  
MASTER OF SCIENCE  
May, 1995

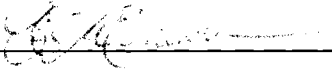
POSITION/FORCE CONTROL OF MANIPULATORS  
USED FOR DEBURRING AND GRINDING

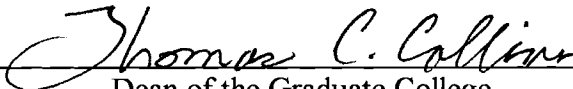
Thesis Approved:

  
\_\_\_\_\_

Thesis Adviser

  
\_\_\_\_\_

  
\_\_\_\_\_

  
\_\_\_\_\_

Dean of the Graduate College

## ACKNOWLEDGMENTS

I wish to express sincere appreciation to Dr. Lawrence L. Hoberock, my major advisor, for his encouragement, advice, and the many hours of guidance throughout my graduate program. Many thanks also go to Dr. Eduardo Misawa and Dr. Ronald D. Delahoussaye for serving on my graduate committee. Their suggestions and support were very helpful throughout this study. Financial support during my graduate study was provided by the Oklahoma Center for Integrated Design and Manufacturing, together with the Oklahoma Center for the Advancement of Science and Technology.

This work is dedicated to my wife Hui Deng and my parents for their love, understanding, and encouragement over the years.

## TABLE OF CONTENTS

Chapter	Page
I. INTRODUCTION.....	1
Background.....	1
Robotic Deburring and Grinding.....	3
Deburring with Compliant Devices .....	6
Hybrid Position/Force Control.....	8
Impedance Control.....	11
Hybrid Impedance Control.....	14
Stability Analysis .....	15
Objectives of This Study.....	17
II. DYNAMIC MODELING OF A MANIPULATOR ENGAGED IN ROBOTIC GRINDING .....	19
Grinding Mechanics.....	19
Mechanics of Robotic Grinding .....	23
Dynamics of Manipulators .....	32
SCARA Robot .....	34
Jacobian Matrix.....	38
III. CONTROL DESIGN AND ANALYSIS.....	42
Manipulator Performance .....	42
Control Architecture.....	46
Impedance Control.....	49
Hybrid Impedance Control.....	52
Simultaneous Position and Force Control .....	57
IV. SIMULATION AND ANALYSIS .....	62
Simulations.....	62
Simulations for Impedance Control.....	68
Results and Analysis for Impedance Control .....	69
Simulations for Hybrid Impedance Control .....	77

	Results and Analysis for Hybrid Impedance Control.....	77
	Simulations for Simultaneous Position/Force Control.....	81
	Results and Analysis for Simultaneous Position/Force Control.....	87
V.	CONCLUSIONS AND RECOMMENDATIONS.....	102
	Conclusions.....	102
	Recommendations.....	104
	REFERENCES.....	105

## LIST OF FIGURES

Figure	Page
1.1 Schematic Diagram of a SCARA Robot Engaged in Grinding.....	4
1.2 Interaction of a System and an Environment.....	16
2.1 Schematic Diagram of Conventional Grinding.....	20
2.2 Schematic Diagram of Robotic Grinding Process.....	24
2.3 The Geometry of Grinding.....	26
2.4 Schematic Diagram of Two-Arm SCARA Robot.....	35
2.5 Schematic Diagram of Three Spaces for an Arbitrary Curved Edge.....	37
3.1 Diagram of Control Structure.....	48
3.2 Block Diagram of Impedance Control with Spring-Like Environment.....	52
3.3 Diagram of Hybrid Impedance Control.....	56
3.4 Control Diagram of Simultaneous Position/Force Control.....	60
4.1 Motion History of Two-arm Berkeley SCARA Robot.....	63
4.2 Schematic Diagram of Geometry of Burrs.....	66
4.3 Schematic Diagram of Robot Configuration in Deburring.....	67
4.4 Results of Simulation 1 with Impedance Control: (a) Position Error.....	71
4.5 Results of Simulation 1 with Impedance Control: (b) Forces.....	72
4.6 Results of Simulation 2 with Impedance Control: (a) Position Error.....	73
4.7 Results of Simulation 2 with Impedance Control: (b) Forces.....	74
4.8 Results of Simulation 3 with Impedance Control: (a) Position Error.....	75
4.9 Results of Simulation 3 with Impedance Control: (b) Forces.....	76
4.10 Results of Simulation 4 with Hybrid Impedance Control: (a) Position Error.....	79
4.11 Results of Simulation 4 with Hybrid Impedance Control: (b) Forces.....	80
4.12 Schematic of Large Burrs.....	85
4.13 Results of Simulation 5 with Simultaneous Position/Force Control: (a) Position Error.....	88
4.14 Results of Simulation 5 with Simultaneous Position/Force Control: (b) Forces.....	89
4.15 Results of Simulation 6 with Simultaneous Position/Force Control: (a) Position Error.....	90

4.16	Results of Simulation 6 with Simultaneous Position/Force Control:	
	(b) Forces.....	91
4.17	Results of Simulation 7 with Simultaneous Position/Force Control:	
	(a) Position Error .....	93
4.18	Results of Simulation 7 with Simultaneous Position/Force Control:	
	(b) Forces.....	94
4.19	Results of Simulation 8 with Simultaneous Position/Force Control:	
	(a) Position Error .....	95
4.20	Results of Simulation 8 with Simultaneous Position/Force Control:	
	(b) Forces.....	96
4.21	Results of Simulation 9 with Simultaneous Position/Force Control:	
	(a) Position Error .....	98
4.22	Results of Simulation 9 with Simultaneous Position/Force Control:	
	(b) Forces.....	99
4.23	Results of Simulation 10 with Simultaneous Position/Force Control:	
	(a) Position Error .....	100
4.24	Results of Simulation 10 with Simultaneous Position/Force Control:	
	(b) Forces.....	101

## NOMENCLATURE

$B$	Target damped matrix
$B_e$	Environmental damped matrix
$b$	Width of cut
$C$	Centrifugal and Coriolis term matrix in joint space
$C_t$	Centrifugal and Coriolis term matrix in Cartesian or task space
$D$	Diameter of grinding wheel
$d$	Depth of cut
$F$	Interaction force vector
$F_{act}$	Actuator force vector
$F_n, F_t$	Normal and tangential (cutting) grinding force
$F_s$	Static friction vector in joint space
$F_{s_t}$	Static friction vector in Cartesian or task space
$G$	Gravity term vector in joint space
$G_t$	Gravity term vector in Cartesian or task space
$J$	Jacobian matrix
$J_c$	Jacobian matrix mapping from joint space to Cartesian space
$J_{ct}$	Jacobian matrix mapping from Cartesian space to task space
$K$	Target stiffness matrix
$K_e$	Environmental stiffness matrix
$K_p, K_i, K_d$	Proportional, integral, derivative gain matrices
$K_f$	Force gain vector
$l$	Chip length
$l_1, l_2$	Length of link 1 and link 2
$M$	Inertial matrix in joint space
$M_d$	Target inertial matrix
$M_t$	Inertial matrix in Cartesian/task space
$q$	Joint coordinate vector.
$s$	Laplace operator



$u$	Specific energy for grinding process
$V_w$	Speed of workpiece
$V_s$	Peripheral wheel speed
$v_n, v_t$	Velocity along normal and tangential direction
$X$	Position vector in ask space
$Z$	Impedance matrix
$Z_e$	Environmental impedance vector
$Z_m$	Volume removal rate
$\tau$	Torque vector, control input
$\mu$	Coefficient of grinding friction
$\sigma_n, \sigma_t$	Grinding Coefficient in normal and tangential direction
$\Lambda_m$	Metal removal parameter

## **CHAPTER I**

### **INTRODUCTION**

#### **Background**

A burr is an undesired projection of material formed as the result of cutting, shearing or casting processes. It is unavoidable in many machining operations. Since burrs can cause interference in the fit of components in assembly, defects in finished components, and injuries to workers, they must be removed. Very often, deburring is not sufficient for some parts, and more precise finishing, called edge finishing must be done to achieve desired contours. At present, deburring and edge finishing are costly and labor-intensive. It is common to deburr or grind edges or surfaces manually in off-line processes, resulting in extra material handling, increased processing time, and lower quality products. In some highly automated machining processes, deburring or edge grinding operations may require a significant portion of the time and cost, compared with other machining operations. It is desirable to develop automatic deburring and edge grinding to reduce manual work as much as possible, integrating deburring or edge grinding operations with automated on-line process to streamline machining operations. Because of its success in other manufacturing operations, the use of robotics appears to offer potential for automatic deburring and edge grinding.

Automation in manufacturing industries has made extensive use of industrial robots [1], particularly in those cases where operations are repetitious and require moderate

position accuracy superior to that of an unaided human. A basic operation in many robot applications is to pick up an object from one location and move to another for machining, storing or assembly [2], [3]. This is called a "pick-place" operation. Other common applications of industrial robots are in spot welding, arc welding, and spray painting. Carrier Transicold, Athens, GA, a part of United Technologies' Carrier Corp, used a five-axis gantry-mounted MR5 robot in an arc-welding process to reduce labor hours by 67%, performing approximately the work of three manual welders [4]. Moreover, the production rate of 32 units per day increased to 50 units daily by using the arc-welding robot. In painting automation, the use of spray robots has become commonplace, as spray robots not only significantly increase painting speed, but also save paint and improve the finish quality[5]. Successfully employing industrial robots is particularly effective in increasing speed and efficiency in the automotive industry.

The essential feature in most successful robot applications is that manipulators are commanded to perform only unconstrained maneuvers. There typically is no interaction between manipulators and environments, and the motion of manipulators is free in the workspace, that is, any external force on the manipulator is considered an unwanted disturbance. The objective in controlling unconstrained manipulators is typically to achieve precise motion tracking or pick-and-place accuracy under highly robust control. Substantial development in the dynamics and control of manipulators with unconstrained motion has occurred in the last two decades [6].

In contrast to most robotic applications, robotic deburring or edge grinding involves interaction of manipulators and manipulator tools with their environments, namely the workpieces processed. Accordingly, manipulator dynamics must be treated as constrained maneuvers, in which motion along some path may be constrained by the environment. While robot end effectors are commanded to move along a desired trajectory, contact forces are generated both normal and tangential to the contact surface. In such case, both the robot and the environment must be considered part of the total

dynamic system. Manipulators in constrained maneuvers require control of both motion and force, or regulation between motion and force. Control of interaction force and motion simultaneously is fundamental to robotic deburring and grinding. Because control of a constrained manipulator requires high precision, force and position feedback, and advanced control strategies, it is often difficult to implement. Developing an effective and efficient scheme for force control of robots associated with deburring and edge grinding is therefore an attractive research problem.

### Robot Deburring And Edge Grinding

Robot deburring and edge grinding consists of a robot carrying a finishing tool traveling along a desired path while the finishing tool, driven by an independent actuator, rotates at high speed for metal removal. Figure 1 shows a simple example of a deburring or edge finishing process using a SCARA (selective compliance articulated robotic arm) robot with a grinding wheel mounted on the end effector of the robot. While the robot is commanded to follow a desired trajectory, it traverses the grinding wheel along the edge of a workpiece. Material removal occurs as the grinding wheel or finishing tool cuts into the workpieces. While traditional grinding machines may be limited to motion of the tool along simple geometric curves, such as straight lines or circles, a finishing tool mounted on a robot can easily travel along complex spatial curves. This allows more flexibility for robot deburring or grinding in complex tasks.

The aim of robot deburring and edge finishing is to produce, by metal removal, finished surfaces along commanded trajectories within allowed dimensional tolerances and surface roughness. The cutting performance of deburring and grinding tools is primarily dependent on three process parameters [7]: rotation speed of the cutting tools, depth of cut, and relative traverse speed of grinding tool and workpiece. For a given geometric configuration and type of tool, the rotation speed of the finishing tool primarily influences

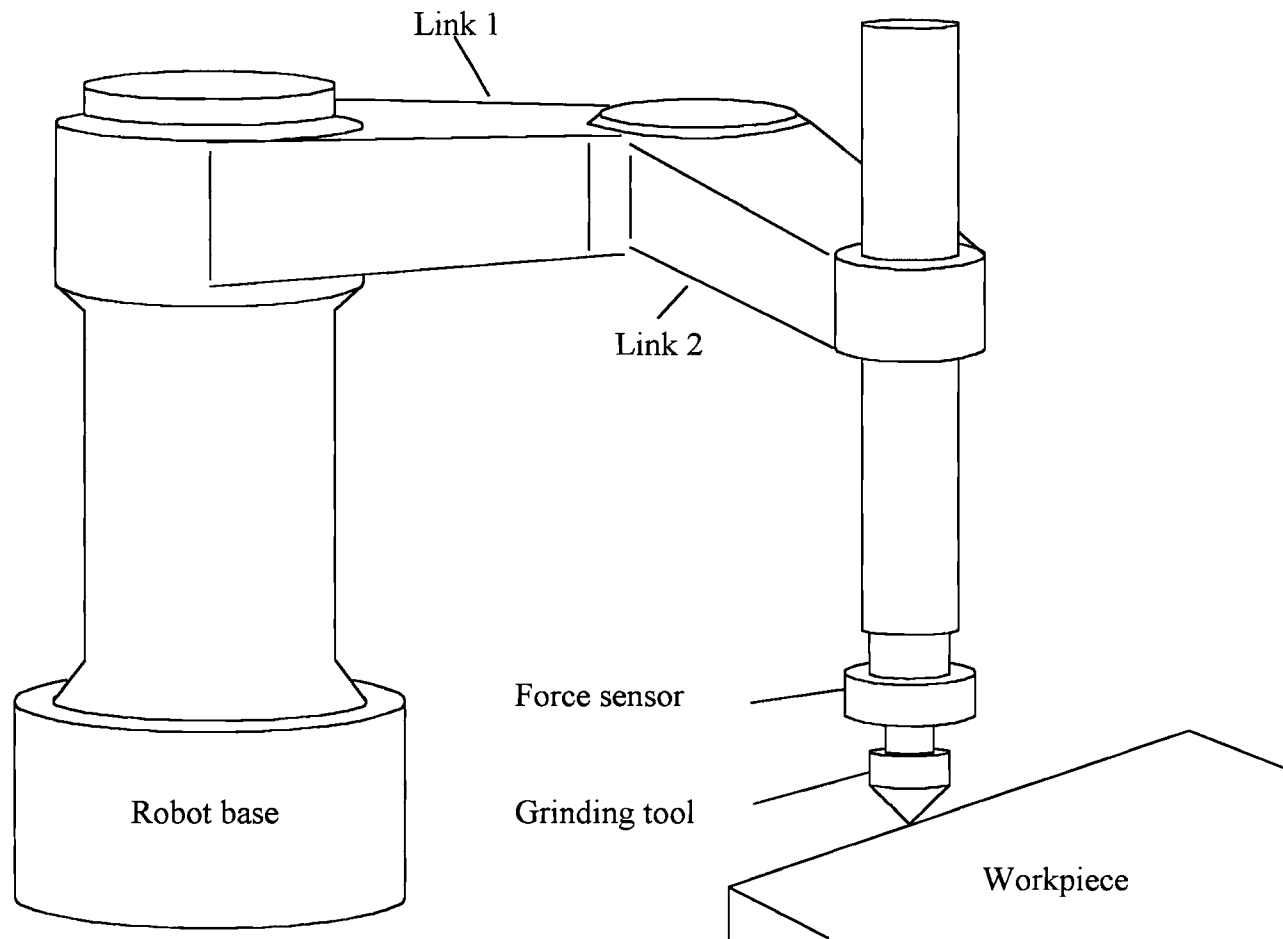


Figure 1.1 Schematic Diagram of a SCARA Robot Engaged in Grinding

the finish of edges or surfaces. Within the stable grinding stage, increasing the rotation speed of grinding tools usually improves the finish, provided other grinding conditions remain constant. On the other hand, the depth of cut and relative traverse speed of the grinding tool govern the material feed rate of the grinding process, and therefore determine the grinding force generated [7].

Similar to other automated processes, robot deburring and grinding will perform best when the disturbance or input is constant, such as a "continuous" bur with constant width, height, and shape. This would imply a uniform material feed rate and depth of cut. On the other hand, a robotic deburring or grinding process should be robust to maintain acceptable performance under fluctuations of inputs and disturbances within allowable ranges. In many cases, workpieces are fixed, such that material feed rates must be controlled by adjusting the robot's position and traversing speed along desired edges or surfaces.

Force control is central to robot deburring and edge grinding, and the forces generated by the cutting process can be resolved into components normal and tangential to the trajectory at an idealized "point" of contact between the tool and workpiece. Maintaining the normal force within desirable limits usually will also maintain the tangential force within limits, both of which are essential for satisfactory cutting performance. Zero normal force implies loss of contact, with no cutting action; excessive normal or tangential force may cause stall of the grinding tool, or damage to the tool, workpiece, or robot. In fact, for many applications, when the interacting force exceeds specific limits, chattering may occur before tools or the robot system are damaged. Chattering is an undesired high frequency oscillation between contact and loss-of-contact between tool and workpiece. It degrades the quality of the edge or surface finish and ultimately will damage the tool. It can be avoided with appropriate force control.

There are two principal strategies for force control currently employed in robot deburring or edge grinding processes. One is to utilize a compliant device connecting the

robot end-effector to the cutting tool to compensate for interacting forces and position uncertainty of environments [8],[9]. Use of such compliant devices allows commercial robots to be used directly without modification of built-in controllers. The second strategy is to directly mount the finishing tool on the end effector of the robot and employ force control by means of an advanced robot controller that integrates end effector motion control with a force feedback loop.

In the first strategy, the compliant device absorbs much of the contact force variation, such that the required robot motion compensation control is less demanding. Depending upon requirements, this may allow commercial robots to be directly employed without much modification. Some innovative designs of compliant devices, such as the RCC(Remote Center Compliance)[10], have been applied to deburring. However, any type of passive or active compliant devices may increase the end effector inertia of the robot system, adversely affecting performance. Allowable inertia should be carefully designed, considering the grinding tool, part contour, feed rate, and desired accuracy. Typically, large inertia of compliant devices limit the applications of such devices. Without compliant devices, the second approach usually requires more accurate and robust control algorithms than are available on commercial robots. Although this strategy is complex and difficult to implement, it is flexible and versatile. As robot controllers and sensors improve, this method will become more feasible.

### Deburring with Compliant Devices

Early research in robotic deburring employed compliant elements at the end effector. Kramer et al. [8] first explored the fundamental mechanisms of robot deburring. Based on the stiffness of an end effector required for a specific deburring task, Kramer, et al. designed a passive single-degree-of-freedom end effector(PSDF) to hold a finishing rotary file. This device provided initial compliance for force variation and position

uncertainty occurring during the deburring process. With the PSDF end effector mounted, a robot with open loop position control was able to achieve stable deburring results. However, deburring without force feedback, such as initially used by Kramer, et al., may result in surface finishes that are insufficiently smooth. Thus, a new strategy was proposed to integrate a force feedback signal. This approach employed a robot position control loop and a fine motion control loop. The fine motion control loop was robot-independent and utilized a micromanipulator to adjust the relative position of a workpiece relative to the end effector based on a feedback signal from a force sensor. For the robot position control loop, the robot performed the programmed function with no communication from the end effector force signal. This allows a robot to be directly applied to the process without knowledge of the robot's dynamics and controller architecture. An active x-y positioning table mounting with a force sensor was developed in the experiment to implement the performance of the micromanipulator in the fine motion loop.

Kazerooni, et al. [9] investigated this strategy in the frequency domain and pointed out that for a deburring robot, stiffness in the normal and tangential directions should be designed to be low and high, respectively, so that the system is robust relative to robot oscillations, robot inaccuracy, and fixturing errors. On the other hand, the deburring process requires a large robot stiffness in the normal direction and small stiffness in tangential direction to achieve good deburring performance. This requirement causes the end effector to ignore the interaction force in the normal direction and stay close to the desired trajectory. These conflicting design requirements raise the control problem for this strategy together with difficulty in practical implementation. A compliant device for the end effector and an active x-y positioning table were designed and implemented to overcome these difficulties.

Recently, Koelsch [11] reported that General Dynamics used flexible-abrasive brushes with a "constant force" device mounted on the end effector of an industrial robot



to debur and chamfer bulkheads and other complex parts for the F-16 fighter. The combination of the innovative tooling and robot control allowed robot deburring to successfully achieve the desired results. From a control viewpoint, the wire brushes function as a highly compliant device to compensate for position uncertainty and fixturing errors.

### Hybrid Position/Force Control

Traditional approaches dealing with free motion control of manipulators without contact with the environment focus mainly on the inertial effects on performance. In contrast, force control for manipulators constrained by environments must deal with the combined influence of robot inertia and compliances of robot and workpiece.

Effective force control of manipulators requires integration of task modeling, trajectory generation, force and position feedback, control, and stability. It requires good understanding of task goals and good modeling, such that an effective control strategy and trajectories may be planned. It also requires control such that stable and precise performance of the manipulator is achieved. Since measurement of force and position may be noisy, effective filtering techniques may be needed. An effective force and position control algorithm should fulfill all these requirements.

Much research has been done on the force control of manipulators involved in constrained motion, and an overview of available force control algorithms is given in [12]. Whitney classified force control approaches, based on the relation of the control input and output, into several types of methodologies, including: stiffness control, damping control, impedance control, hybrid force/position control, and explicit/implicit force control.

The fundamental differences in various force control methods associated with manipulators may be classified into two types of control architectures: hybrid force/position control [13],[14],[15] and impedance control [16] - [24]. In hybrid

force/position control, force is commanded and controlled along those directions constrained by the environments, while position is commanded and controlled along those directions in which manipulators is unconstrained and free to move. Usually, the force and position control directions are orthogonal, and a particular control law may be applied in the individual direction for the regulation of force errors or position errors. On the other hand, impedance control focuses on the relationship between the interaction force and the end-effector position. Instead of controlling force or position individually, impedance control attempts to regulate the interaction force by controlling the amount of compliance or impedance in the manipulator. Using impedance control, a designer can specify a target impedance, the desired relationship between the interaction force and end-effector position, and control the position to maintain the desired interaction force. We first review hybrid position/force control strategies.

Hybrid position/force control is used for control tasks requiring force control in some directions and motion control in other directions. It requires the task description to be decoupled into elemental subtasks, which are defined by a particular set of constraints. Typically, a position constraint exists in the direction normal to the contact surface, and a position control subtask is formulated with a force constraint along the tangential direction of the contact surface. Thus, control is partitioned into a set of orthogonal constraint directions. With each subtask, pure force control or pure position control algorithms may be applied. For instance, in the force control direction, force is commanded and controlled explicitly. The key to hybrid control is the specification of a task constraint frame, either a natural constraint frame or an artificial constraint frame. Mason [13] discussed kinematic constraints imposed on manipulator motion due to a particular task geometry. The discussion in this paper is quite general and includes many types of constraints that can occur during a variety of tasks.

Raibert and Craig [14] first developed hybrid force/position control, with the position and force loops operating under different control laws (PID for position and PI

for force) to control a manipulator. Position was measured with joint-mounted sensors and a force signal was obtained by a wrist-mounted force sensor. A selection matrix was introduced to indicate the particular constraint in each degree-of-freedom, and this was used to apply compensation functions to determine the actuator drive signal for each joint. Experiments were conducted using a two-axis Scheinman robot to test the designed controller. Different levels of forces were commanded in the normal direction while motion was controlled simultaneously in the tangential direction. While the results showed stable control, force error developed, together with overshoot and unspecified position errors in the normal direction.

Yoshikawa et al. [15] extended Raibert and Craig's hybrid control approach to a more general case where the full dynamics of the manipulator were considered, and the end effector constraint was explicitly described by constraint hypersurfaces. To design a hybrid controller, nonlinear state feedback was introduced to linearize the manipulator dynamics. Then servo-controllers were designed for both position and force control based on the linearized model. A two degree-of-freedom assumption was employed to design the servo controllers, which took account of both command response and robustness for the modeling errors and disturbances.

The disadvantage of hybrid force/position control algorithms is the neglect of manipulator impedance, and thus inability to regulate the relation of force to position. In the position control direction, forces are either neglected or considered as disturbance, while in the force control direction motion errors are left uncontrolled. On the other hand, hybrid force/position control requires explicit and accurate descriptions of environmental dynamics in term of position and force constrains. For some complex tasks, this will present difficulties in formulation and computation.

## Impedance Control

The impedance of a dynamic system is defined from a linear relationship between displacement and force given by:

$$F = Z\Delta X \quad (1.1)$$

where  $\Delta X$  is an  $m \times 1$  displacement vector of the system from its equilibrium position,  $F$  is an  $n \times 1$  vector of external forces applied to the system, and  $Z$  is an  $n \times m$  impedance matrix. For the static case,  $Z$  is simply the stiffness  $K$ , a real-valued nonsingular stiffness matrix with constant elements. The stiffness matrix primarily characterizes the behavior of a system in constrained maneuvers. Large entries in the stiffness matrix imply large interaction forces, while small entries in the matrix allow for a considerable amount of motion of the system in response to interaction forces.

The dynamic impedance characterizing the behavior of an  $n$ -dimensional linear dynamic system contains inertial, damping, and stiffness elements. It may be defined using Laplace transform notation as:

$$Z = M_d s^2 + B s + K \quad (1.2)$$

where  $s$  is the Laplace variable and  $M_d$ ,  $B$ , and  $K$  are  $n \times n$  positive matrices representing inertial, damping, and stiffness elements of the system, respectively.

Impedance control regulates the impedance of a system, instead of controlling the motion of the manipulator or the interaction force individually, as in hybrid force/position control. By controlling the manipulator motion and specifying the impedance, a designer can ensure that the manipulator will be able to maneuver in a constrained space while maintaining appropriate contact force. Impedance control is considered a combination of pure position control and pure force control. It approaches pure position control when stiffness approaches infinity. In contrast, if the stiffness approaches zero, it approaches pure force control.

The initial idea of impedance control derives from Salisbury's stiffness control [16], which used a static form of impedance. The desired relationship of contact force and manipulator motion was modeled as the stiffness of a spring. Active force control was applied to make the manipulator behave as the desired spring. By specifying the desired spring stiffness, designers were able to achieve the desired interaction force. Essentially, Salisbury's stiffness control is a PD (proportional plus derivative) type control law with force feedback, which is mapped to modify manipulator position.

Whitney [17] developed another approach, called damped force control, as another form of impedance control. In damped force control, the desired relationship of the interaction force to manipulator motion was modeled as a dashpot. The difference between damped control and stiffness control is that the former uses manipulator position as commanded input, while the later uses manipulator velocity as the commanded input.

Hogan's impedance control [18], [19] generalized the work of Salisbury and Whitney by forcing the dynamic behavior of any manipulator to approximate a generic linear second-order system with inertia, damping, and stiffness. The concept of impedance control is to reshape the dynamics of the manipulator such that the closed loop system behaves as a mass-dashpot-spring system, whose parameters (inertial, damping, and stiffness matrix) can be specified by the designer based on the desired behavior of the total system. Hogan's paper series [18] explained the fundamental theory of impedance control. Using causality and bond graph theories, he presented a thorough study of the mechanics of interaction between physical systems. He demonstrated the necessity of controlling the impedance of manipulators so that the desired dynamic interaction between a manipulator and its environment could be achieved. Hogan also investigated control both with force feedback and without force feedback. Finally, a simple control law for impedance control was developed for a manipulator with a desired Cartesian impedance. In his later work [19], Hogan conducted experiments with a robot to follow a simple edge to verify the

validity of impedance control. The results showed that proper design of an impedance controller can guarantee the stability of manipulators in contact with environments.

A sophisticated design method for impedance control was developed by Kazerooni et al. [21], in which both target dynamics and stability robustness in the presence of bounded model uncertainties are considered. Full state feedback and feedforward force was investigated to achieve the target dynamics and global stability. The control approach, however, was established based on a linearized model of a manipulator in a small neighborhood around the equilibrium position, with an assumption of small perturbations in position; the nonlinear velocity term in the manipulator dynamics was ignored. A controller for a plane position table was designed by this method, and experiments were conducted to study the interaction between the table and a stiff wall.

Recently, experiments [27] were carried out on a direct drive robot manipulator to investigate the impedance control method with both a linear (Kazerooni, 1986) and a nonlinear controller (Colgate and Hogan, 1988). The results from both controllers were compared, showing that the behavior of the manipulator with a linear controller was inferior when the manipulator engaged in constrained maneuvers. However, the experiments investigated only cases in which the input was a constant, that is, set-point control. Controlled behavior with a dynamic input is needed for more general cases, such as deburring and grinding.

Impedance control has attracted much study, both theoretically and experimentally. It is considered a general control method for manipulators with constrained and unconstrained motion. However, the design and implementation of impedance control is not as intuitive as hybrid position/force control. It is also difficult to map the desired dynamic behavior and performance of the controlled system into the target impedance relationship. In addition, almost all of the literature dealing with impedance control is limited to linear environments. Nonlinear environments raise significant complexities in designing and implementing impedance control. Furthermore, it is difficult to design a

impedance controller to achieve desired performance and preserve stability with robustness for bounded uncertainties.

### Hybrid Impedance Control

Hybrid impedance control is a combination of hybrid position/force control and impedance control. It breaks down a task into two subtasks in orthogonal directions, along which either impedance force control or impedance position control is applied. Noticing the advantages both hybrid control and impedance control, Anderson and Spong [24] first proposed the concept of hybrid impedance control. They modeled manipulators, environments and their interaction as an electrical network and used the Norton and Thevenin equivalents in the network to establish a duality principle, leading to a rule to construct target impedances of manipulators and select appropriate control schemes. The dynamics of an environment were modeled as a linear impedance, and the manipulator interacting with the environment was controlled as the dual of the environmental impedance. According to their proposals, impedance relationships could be classified into three types of impedance: inertial, resistive, and capacitive, given by

$$|Z_v(0)| = \begin{cases} 0 & \text{Inertial impedance} \\ c & \text{Resistive impedance} \\ \infty & \text{Capacitive impedance} \end{cases} \quad (1.3)$$

where  $0 < c < \infty$ . In Laplace notation, these types of impedances take following forms respectively [24]:

$$Z_v(s) = \begin{cases} M_d s & \text{Inertial impedance} \\ B & \text{Resistive impedance} \\ M_d s + B + K / s & \text{Capacitive impedance} \end{cases} \quad (1.4)$$

If the environmental and manipulator impedances are modeled or chosen to be one of the above impedance relations, then the duality principle can be applied. That is, if the

environmental impedances are capacitive, then there will be force control with noncapacitive manipulator impedances; if the environmental impedances are inertial, then position control with noninertial manipulator impedances will be applied; if the environmental impedances are resistive, either force control with inertial manipulator impedances or position control with capacitive manipulator impedances is applied.

Hybrid impedance control is more similar to hybrid position/force control than to impedance control. Force and position can be commanded explicitly once the impedance of the environment is defined or modeled. The duality principle is useful for designers to choose the control approach and target impedance for a desired task requirement. We will investigate hybrid impedance control further in our deburring study in Chapter III.

### Stability Analysis

Stability analysis is a difficult issue in designing a controller for manipulators with constrained motion. This is because guaranteeing stability of manipulators in unconstrained maneuvers does not guarantee stability of manipulators after they interact with environments. Few discussions in the literature address stability analysis for hybrid position/force control primarily because the design strategies are so intuitive. In Yoshikawa's work [15], stability of manipulators was ensured by considering the robust design of a two degree-of-freedom control law.

For impedance control, as Kazerooni pointed out [22], the stability must address two important issues: stability of target dynamics and the global stability of the dynamic system and its environment. Stability of target dynamics is ensured by the proper choice of target impedance parameters,  $M_d$ ,  $B$ , and  $K$ . If these target impedance matrices are real, symmetric, and positive definite, the target dynamics are stable.

Stable target dynamics are necessary for the global stability of the complete dynamic system; however, this does not guarantee stability of the total system after



contact. It is much more difficult to guarantee global stability of the complete dynamic system, including nonlinear dynamics of manipulator and environment.

For linear, stable environments, Kazerooni et al. [21] gave a sufficient condition with informal proof, showing the stability of the complete system can be achieved provided linear, stable target dynamics are designed with symmetric, positive definite inertial, damping, and stiffness matrices. However, An and Hollerbach [25] showed that a forth-order linear system, consisting of a manipulator with a force sensor and environment, employing impedance control for contact tasks with a very stiff environment became unstable.

Colgate and Hogan [26] presented a necessary and sufficient condition to guarantee the stability of a linear model of manipulators coupled at a single interaction port to a linear, passive environment. Using the Nyquist criterion for a system depicted in Figure 1.2, they concluded that the controlled system  $A(s)$  being positive real is a necessary and sufficient condition to ensure stability when coupled to any passive, Hamiltonian environment  $B(s)$ . A simulation with a proposed linear model for a manipulator together with actuator and transmission dynamics was used to verify the proposed design method and stability condition.

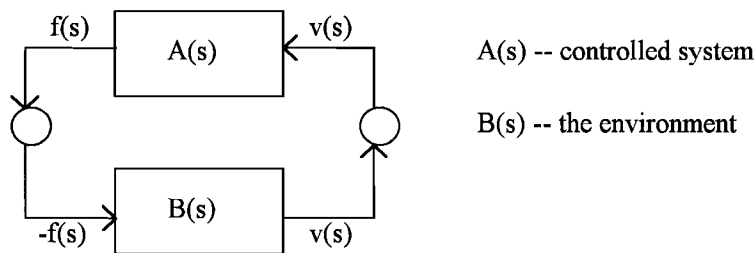


Figure 1.2 Interaction of a System and an Environment

However, McCormick and Schwartz [27] used such a controller in a direct drive robot and discovered experimentally that the manipulator coupled with an environment became

unstable when the force feedback was high no matter how hard (steel) or soft (rubber) the environment. This may have been caused by modeling the interaction as directly coupled linear systems in the derivation of stability conditions.

For the general case, stability mechanisms in impedance control are poorly understood, such stability is dependent upon manipulator dynamics, the nature of the contact environment, and target impedance parameters.

### Objectives of This Study

Previous work reported in the literature on robotic deburring and edge grinding has utilized a separate force control loop to monitor the interaction between manipulators and environments. Force errors obtained from this control loop were mapped into motion modifications, which were added to the command input of the robot position control loop. Speed of response was limited by several issues associated with this strategy, such as mechanical resonance, communication time delay, and programming compatibility. In contrast, integrated robotic position/force control offers the advantages of a more efficient force control computation and coordinated force and motion control. With the advent of faster computers and high performance servos, it has become more attractive to integrate force control into overall robot position control.

This research investigates position/force control of the dynamics of simple SCARA manipulators operating in constrained environments, focusing on the application of manipulators in deburring and edge grinding processes. We employ modeling and simulation to investigate different control algorithms and their achievable results for a sample robot engaged in deburring and edge grinding. Through this study, we propose theoretical control strategies that could later be tested experimentally. In the following chapters, we describe a new approach to the control of robotic deburring and edge grinding to provide more accurate, flexible, and robust control than heretofore possible.

Next chapter first reviews the mechanics of grinding processes in order to develop a more practical force model for robotic deburring and grinding. We use empirical and experimental results from conventional grinding process research, together with some simplifying assumptions to derive interaction force models for robot control purposes.

In chapter 2, we present dynamic models for grinding and manipulator motion in the presence of contact and grinding forces.

Chapter 3 presents a new force and motion control algorithm for robotic deburring and grinding. Impedance control and hybrid impedance control are also investigated in this chapter.

In Chapter 4, edge following and deburring/grinding processes are simulated for selected workpiece edge contours so as to test and compare between the control algorithms discussed in this study. Analysis and discussion of the simulation results are also presented.

We present conclusions of this study and recommendations for future work in Chapter 5.

## CHAPTER II

### DYNAMIC MODELING OF A MANIPULATOR ENGAGED IN ROBOTIC GRINDING

Appropriate modeling of dynamic systems is usually essential for designing and analyzing controllers for these systems. Robotic deburring and grinding incorporates the dynamic behavior of conventional grinding, with complexities added due to the somewhat compliant nature of robotic arms. In this chapter, we develop a model for the interaction forces in robotic deburring and grinding. The control strategy discussed in the remaining part of this thesis is based on the model obtained here. Manipulator dynamics are also developed in this chapter.

#### Grinding Mechanics

Conventional grinding process is a complicated and poorly understood machining process. Usually, a grinding wheel is considered a complex tool with thousands of very small metal cutting "teeth" sprinkled along the periphery of the wheel [7]. The abrasive grains are all different, with irregular shapes, and are randomly oriented on the grinding wheel. Most grains have large negative rake angles causing them to slide rather than cut. Thus, the interaction process between grains and workpiece consists of cutting, plowing, and rubbing[28]. The stochastic nature of the grains makes it very difficult to analyze the grinding process and even more difficult to model the dynamics of grinding. Thus, there is

no good analytically-developed mathematical model for the conventional grinding process. An attempt to suitably model the process will, however, provide us with a better overall understanding and help to interpret the forces produced by this process.

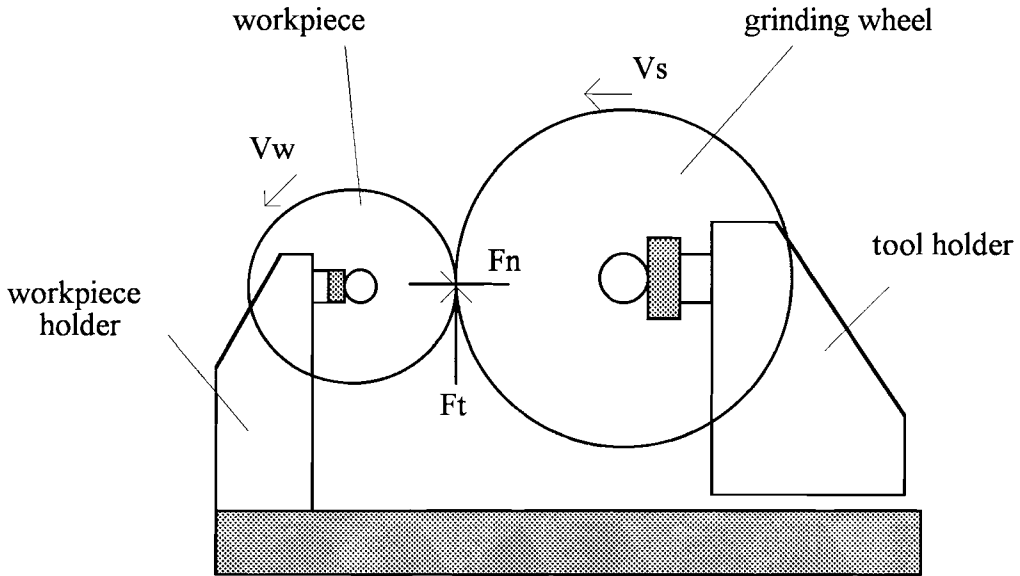


Figure 2.1 Schematic Diagram of Conventional Grinding [28]

Typical studies of grinding processes are based on the analysis of a single grain interacting with a workpiece using energy principles and geometric approximations [7]. Two orthogonal forces can be considered as generated in the grinding process:  $F_n$  normal to the contact surface, and  $F_t$  ( the cutting force ) tangential to the contact surface, as shown in fig. 2.1. From an energy viewpoint, the average cutting force on an individual grain is dependent on the energy consumed to remove material per unit volume, and is given by [7]

$$F_t = u_s V_w b d / V_s \quad (2.1)$$

where

$F_t$  = average cutting force

$u_s$  = specific energy

$V_w$  = feed rate, or work speed

$b$  = width of the grinding path

$d$  = depth of cut

$V_s$  = peripheral wheel speed

In (2.1), all the parameters except  $u_s$  are controllable to some extent and may be adjusted to obtain a desired cutting force. Equation (2.1) offers a theoretical basis for calculation of grinding force. The specific energy  $u_s$ , however, is an experimentally obtained quantity and is dependent upon the grinding and workpiece materials and grinding conditions. It varies considerably with the geometry of chips cut from the workpiece because the energy mode for grinding varies with chip formation. For small chips, energy requirements may be principally due to friction, while for larger chips energy may be principally required for cutting. Attempting to express  $u_s$  analytically as a function of other parameters is based on some assumptions and approximations, such as a straight-line cutting path, idealized grains, evenly distributed grains along a peripheral line, etc.. Most investigators consider the specific energy to be proportional to the inverse of chip thickness, leading to the following approximate proportionality [7]:

$$F_t \propto \sqrt{(rV_w / cV_s)\sqrt{d / D}} \quad (2.2)$$

where

$r$  = ratio of chip width to chip thickness,  $10 \leq r \leq 20$ .

$c$  = number of active grains per square area of grinding wheel

$D$  = the wheel diameter.

Relation (2.2) is at best a guide and does not exactly represent cutting forces due to grinding. Since analysis leading to (2.2) is based on assuming cutting by a single grain, quite different from actual grinding, results from using (2.2) may deviate significantly

from experimental results. Because of this, some investigators insist upon an experimental approach to study the grinding process [28].

Hahn and Lindsay [29] completed many experiments to investigate the grinding process and obtained substantial valuable data. They proposed from experimental results an empirical relationship given by:

$$F_n = \frac{\Gamma_w}{\Lambda_w} \quad (2.3)$$

where

$F_n$  = normal grinding force.

$\Gamma_w$  = rate of material removal, (volume of chips removed per unit time)

$\Lambda_w$  = metal removal parameter

It is easily seen that by definition,

$$\Gamma_w = V_w db \quad (2.4)$$

where as before,  $V_w$ ,  $d$ , and  $b$  are the feed rate, depth of cut and width of cut, respectively.

Using (2.4) in (2.3) gives

$$F_n = \frac{V_w bd}{\Lambda_w} \quad (2.5)$$

such that normal force is directly related to the feed rate and depth of cut.

The metal removal parameter,  $\Lambda_w$ , is a function of grinding wheel speed and material, workpiece material, grinding conditions, and details of the wheel dressing preceding the grinding operation. Usually, the metal removal parameter is determined through experiments. In addition, Hahn and Lindsay [29] found that for easy-to-grind materials,  $\Lambda_w$  remains constant as long as the grinding conditions remain unchanged.

A semi-empirical equation for prediction of  $\Lambda_w$  was also suggested in [29]. However,  $\Lambda_w$  predicted by an equation in [29] yielded errors of +/- 20 %. Moreover, this equation is very complex. In contrast, graphs obtained from experimental results in [29]

offered a straightforward means for determination of the metal removal parameter, such that a simple look-up procedure seems more feasible.

While cutting force  $F_t$  determines the energy, or power, used in grinding, normal force  $F_n$  is considered an independent variable affecting the grinding process. Under a specific grinding condition, normal force and cutting force maintain approximately a constant relationship, called grinding friction, such that

$$\frac{F_t}{F_n} = \mu \quad (2.6)$$

where  $\mu$  is the coefficient of grinding friction. Grinding friction  $\mu$  depends on the grinding wheel abrasive, workpiece material, and grinding conditions, and usually is obtained by experiment. Notice that because the normal force  $F_n$  and the cutting force  $F_t$  are related by the coefficient of grinding friction, specific energy  $u$  and metal removal parameter  $\Lambda_w$  are actually related parameters describing the grinding process.

Equations (2.1), (2.5) and (2.6) provide a basis for analyzing the interaction forces in the grinding process, and will be used for robotic deburring and grinding studied in this thesis. Notice that tool pieces used in automatic deburring are not limited to grinding wheels. Milling tools and files are also popular for automatic deburring. However, the interaction forces in milling processes are similar to those for grinding because the analysis of grinding is based on the metal cutting of chips, similar to the milling process. Grinding can be considered milling with thousands of very small teeth. Study of cutting by a single grain in the grinding wheel is analogous to that of a tooth in a milling cutter.

### Mechanics Of Robotic Grinding

A schematic diagram of robotic deburring and grinding used herein is shown in Figure 2.2. A grinding wheel shaped as a flat cylindrical disk is fixed on the end effector



of the robot , which may easily move the grinding or other finishing tools within the robot workspace. In the figure, the  $x$ - $y$  axes refer to a Cartesian frame or reference frame, in which the robot moves. The  $n$  axis is normal to the workpiece surface positive into the workpiece, while the  $t$  axis is directed tangential to the surface, positive in a right-hand coordinate system. The  $t$ - $n$  coordinate system is designated "task space". In the ideal case, the tool wheel moves in the positive or negative  $t$  direction, while motion in the  $n$  direction is constrained. In this work, we consider only two-dimensional grinding and assume the diameter of the grinding wheel is much larger than the depth of cut.

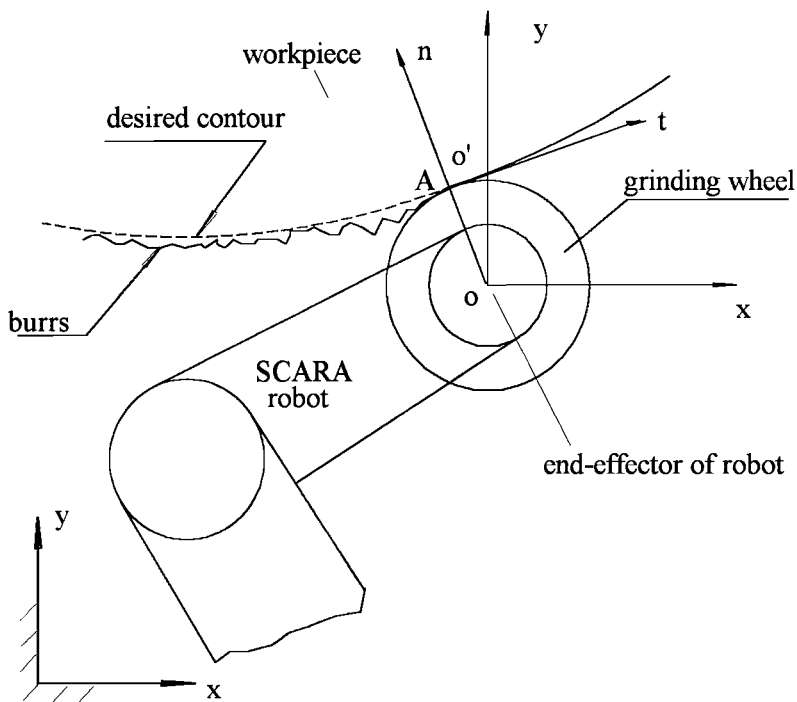


Figure 2.2 Schematic Diagram of the Robotic Grinding Process

Robotic deburring or grinding differs from conventional grinding because of the compliant structure and mobility of the robot. Material feeding is accomplished by moving the robot relative to the workpiece, rather than feed-in of the workpiece, as in the conventional grinding. For conventional grinding machines, the stiffness of the structure molding the cutting tool is very high in all direction, and it is reasonable to assume that

there is no "incidental" or unwanted relative motion between wheel and workpiece to cause spurious changes in material removal rate. Unfortunately, it is not feasible for a robot to have such high stiffness. Deviation from the desired motion due to the compliant robot structure may cause unwanted changes in feed rate and depth of cut. Robot dexterity and mobility may cause unwanted motion against the workpiece, resulting in cutting along a direction different from that desired. Because of this, (2.5) and (2.6) are not sufficient to model the dynamic interaction between tool and workpiece in robotic grinding. Since the normal grinding force is directly proportional to volume removal rate, material feed-in along any direction due to robot motion must be taken into account. This requires expressing the motion of the robotic end effector in task space ( $t, n$  coordinate system) and decomposing the end effector velocity into normal and tangential directions at contact point. The total normal grinding force will be the sum of the individual normal forces proportional to the volume removal rate in each direction.

Fig. 2.3 illustrates the volume of material removal due to motion in the tangential (a) and normal (b) directions. In the force development that follows, we follow the work of [7] and assume that the workpiece is stationary. We also assume that burr heights are small compared to the diameter of the grinding wheel, such that the total depth of cut is small, and that the peripheral speed of the grinding wheel is much higher than the traverse speed. In addition, we assume the grinding wheel is properly dressed and in good condition, and that grinding conditions remain constant during deburring and grinding, such that the diameter of the grinding wheel and the material removal parameter remain constant. Finally, we assume no chattering and that the width of cut  $b$  remains constant. The total volume of chips removed per unit time  $\Gamma_{mt}$  in the tangential direction is clearly

$$\Gamma_{mt} = v_t db \quad v_t \geq 0 \quad (2.7)$$

such that from (2.3), the normal force due to material feed in the tangential direction is

$$F_{n1} = v_t db / \Lambda_m \quad v_t \geq 0 \quad (2.8)$$

where

$v_t$  = the velocity of the grinding spindle or the end effector tangential to the contact surface.

The motion of end effector in the positive  $n$  direction into the workpiece, causes material removal similar to plunge grinding [7]. In general, the feed rate in this direction is small due to large normal forces generated. Thus the total volume of chips removed per unit time  $\Gamma_{mn}$  in the normal direction is approximately

$$\Gamma_{mn} = lv_n b = \theta(D/2)v_n b \quad v_n \geq 0 \quad (2.9)$$

where

$v_n$  = velocity of the end effector, or grinding-wheel, positive into the workpiece.

$l$  = arc length of the tool in contact with workpiece.

$\theta$  = the central angle corresponding to arc  $l$

It can be seen from Figure 2.3(b) that

$$\theta = \cos^{-1}[1 - d / (D/2)] \quad (2.10)$$

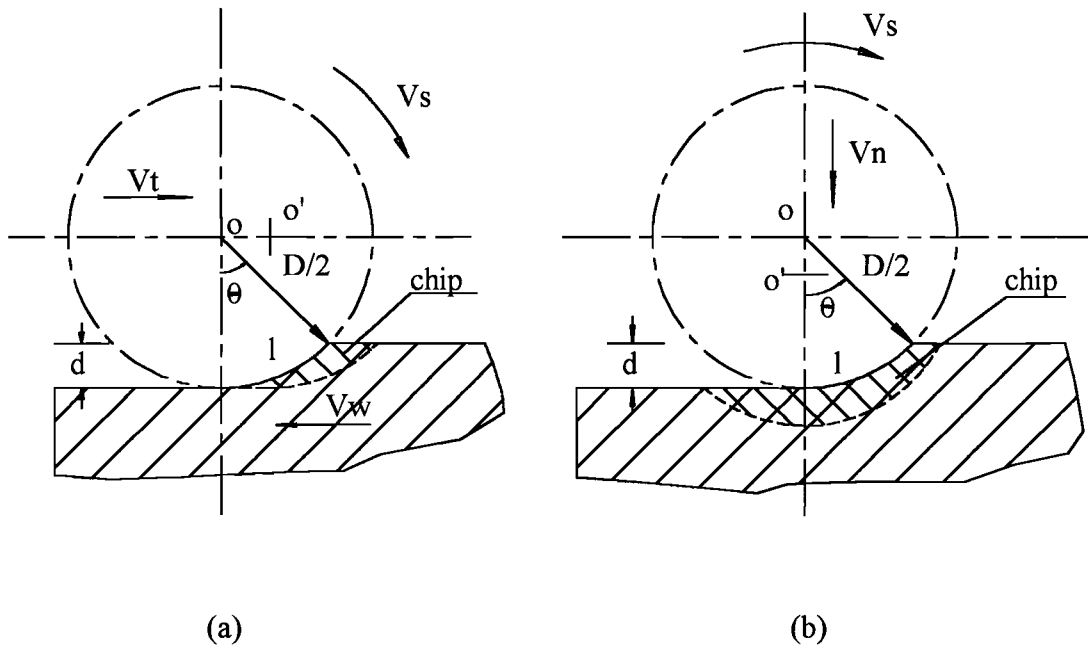


Figure 2.3 The Geometry of Grinding [7]

where  $D$  is the diameter of the grinding wheel. Applying a Maclaurin series expansion for the right side of (10) and eliminating higher order terms yields

$$\theta \approx \pi/2 - (1 - d/(D/2)) \quad (2.11)$$

substituting from (2.11) in (2.9), yields the volume removal rate

$$\Gamma_{mn} = [(\pi/2 - 1)D/2 + d]v_n b, \quad v_n \geq 0 \quad (2.12)$$

Thus from (2.3) the normal force for material removal in normal direction is

$$F_{n2} = [(\pi/2 - 1)D/2 + d]v_n b / \Lambda_m, \quad v_n \geq 0 \quad (2.13)$$

Eq. (2.13) shows that the normal force caused by plunge grinding is related to the dimensions of the grinding wheel. If the depth of cut is much smaller than the diameter of the grinding wheel, such that the term  $d$  in (2.13) can be neglected, then the normal force due to plunge grinding is given by

$$F_{n2} = 0.285Dv_n b / \Lambda_m, \quad D \gg d, v_n \geq 0 \quad (2.14)$$

Combining the non-negative force components from (2.8) and (2.14) gives for the total normal grinding force

$$F_n = F_{n1} + F_{n2} = [v_t + (0.285D/d + 1)v_n]db / \Lambda_m \quad (2.15)$$

Then from (2.6) the tangential grinding force becomes

$$F_t = \mu F_n = \mu[v_t + (0.285D/d + 1)v_n]db / \Lambda_m \quad (2.16)$$

As seen in (2.15) and (2.16), the grinding forces acting on the robot end effector are directly related to the motion in two orthogonal directions, such that coupling will occur when the manipulator dynamics are developed. Furthermore, the dynamic behavior of grinding is highly nonlinear, since products of displacement ( $d$ ) and velocities ( $v_t, v_n$ ) occur in (2.15) and (2.16). Obviously, such forces are generated only when the grinding wheel is in contact with and cutting the workpiece, such that if the depth of cut  $d$  is less than or equal to zero, the wheel has either lost contact or barely contacts the workpiece, generating no forces. Similarly, if grinding wheel motion in the tangential direction is in the negative direction, no grinding forces will be generated. Hence, considering the entire

axes in the  $n$  and  $t$  directions, grinding, or interaction, forces are inherently nonlinear. To express this nonlinearity explicitly, (2.15) and (2.16) may be rewritten as

$$\begin{aligned} F_n &= u(d)[u(v_t)\sigma_t v_t + u(v_n)\sigma_n v_n]d \\ F_t &= \mu F_n \end{aligned} \quad (2.17)$$

where

$$\begin{aligned} \sigma_t &= b / \Lambda_m \\ \sigma_n &= (0.285D / d + 1)b / \Lambda_m \\ u(a) &= \begin{cases} 0 & \text{if } a \leq 0 \\ 1 & \text{if } a > 0 \end{cases} \end{aligned}$$

Eq. (2.17) describes the interaction forces generated between the robot end effector and the workpiece for robotic deburring and grinding. For stable operation with the end effector tracking a desired trajectory, motion in the normal direction is very small compared to that in the tangential direction. Accordingly, the force generated due to cutting along the tangential direction dominates the total grinding force. Even under such operation, however, nonlinear and coupled dynamic behavior characterizes the grinding forces.

In the analysis that follows, we assume that the variables are  $v_t$  and  $v_n$ , and  $d$ , with other parameters characterizing the grinding process remaining constant. We use dot notation in what follows to denote time differentiation. Let quantities  $\dot{x}_{td}$  and  $\dot{x}_{nd}$  represent desired velocities of the end effector in the tangential and normal directions, respectively, and let quantities  $\dot{x}_t$  and  $\dot{x}_n$  represent the actual velocities  $v_t$  and  $v_n$ , respectively. Also, let  $\Delta v_t$  and  $\Delta v_n$  represent small perturbations of  $\dot{x}_t$  and  $\dot{x}_n$  about  $\dot{x}_{td}$  and  $\dot{x}_{nd}$ , respectively. Further, in the normal direction let  $x_{nd}$  represent a desired position of the robot end effector describing the desired contour of the workpiece surface;  $x_n$  represent the actual position; and  $x_e$  represent the actual position of the workpiece edge.

Similarly, let  $d_0$  represent a desired depth of cut, and  $\Delta d$  represent a small perturbation of actual depth of cut  $d$  from  $d_0$ . Then we may write

$$\begin{aligned}\Delta v_t &= \dot{x}_t - \dot{x}_{td} \\ \Delta v_n &= \dot{x}_n - \dot{x}_{nd} \\ d_0 &= x_{nd} - x_e \\ \Delta d &= d - d_0 = x_n - x_{nd}\end{aligned}\tag{2.18}$$

We assume for linearization purposes that the magnitudes of perturbations are no larger than 10 percent of corresponding desired values. Substituting from (2.18) into (2.17), neglecting the small product terms among  $\Delta v_t$ ,  $\Delta v_n$  and  $\Delta d$ , and assuming nonzero positive values for  $v_t$ ,  $v_n$  and  $d$ , we can express the normal grinding force approximately as:

$$\begin{aligned}F_n &= F_{n0} + k_d(x_n - x_{nd}) + k_{vn}(\dot{x}_n - \dot{x}_{nd}) + k_{vt}(\dot{x}_t - \dot{x}_{td}) \\ &\quad \dot{x}_t > 0, \quad \dot{x}_n > 0, \quad x_n > x_e\end{aligned}\tag{2.19}$$

where

$$\begin{aligned}F_{n0} &= k_d d_0 \\ k_d &= \sigma_t \dot{x}_{td} + \sigma_n \dot{x}_{nd} \\ k_{vn} &= \sigma_n d_0 \\ k_{vt} &= \sigma_t d_0\end{aligned}$$

Using (2.6), we may represent the tangential grinding force as

$$\begin{aligned}F_t &= \mu[F_{n0} + k_d(x_n - x_{nd}) + k_{vn}(\dot{x}_n - \dot{x}_{nd}) + k_{vt}(\dot{x}_t - \dot{x}_{td})] \\ &\quad \dot{x}_t > 0, \quad \dot{x}_n > 0, \quad x_n > x_e\end{aligned}\tag{2.20}$$

Now represent (2.19) and (2.20) in matrix form as

$$\begin{aligned}F - F_0 &= B_e(\dot{X} - \dot{X}_d) + K_e(X - X_d) \\ &\quad \dot{x}_t > 0, \quad \dot{x}_n > 0, \quad x_n > x_e\end{aligned}\tag{2.21}$$

where

$$\begin{aligned}
 F &= \begin{bmatrix} F_n \\ F_t \end{bmatrix}, & F_0 &= \begin{bmatrix} F_{n0} \\ \mu F_{n0} \end{bmatrix} \\
 K_e &= \begin{bmatrix} k_d & 0 \\ \mu k_d & 0 \end{bmatrix}, & B_e &= \begin{bmatrix} k_{vn} & k_{vt} \\ \mu k_{vn} & \mu k_{vt} \end{bmatrix} \\
 X &= \begin{bmatrix} x_n \\ x_t \end{bmatrix}, & X_d &= \begin{bmatrix} x_{nd} \\ x_{td} \end{bmatrix}, & \dot{X} &= \begin{bmatrix} \dot{x}_n \\ \dot{x}_t \end{bmatrix}, & \dot{X}_d &= \begin{bmatrix} \dot{x}_{nd} \\ \dot{x}_{td} \end{bmatrix}
 \end{aligned}$$

and where  $x_{td}$  and  $x_t$  are a desired position and actual position of the end effector in the tangential direction, respectively.

At this point, we have linearized the interaction process of robotic grinding for positive values of depth of cut and tangential and normal end-effector velocities, and expressed this process such that dynamic impedances can be obtained. Notice that the "stiffness" matrix  $K_e$  and the "damping" matrix  $B_e$  are positive definite. For the damping matrix, the coupling term  $k_{vt}$  describes the normal force due to the cutting in the tangential direction, while the coupling term  $\mu k_{vn}$  describes the tangential cutting force due to cutting in the normal direction. The set-point force  $F_0$  is dependent on the geometry of the workpiece, desired trajectory, and grinding conditions. It is specified as the force required for cutting the desired trajectory  $X_d$  under ideal machining conditions and a smooth workpiece. Eq. (2.21) describes the relationship between the interaction forces and manipulator motion. If the contact force  $F$  provided by the tool and end effector is equal to the set-point force  $F_0$ , the grinding wheel is able to cut the desired trajectory. Otherwise, cutting force deviations from the set-point force will cause deviation of the end effector from the desired trajectory.

In robotic deburring and grinding, a force sensor is usually available for feedback control. In this study, for simplicity, we assume that a force sensor with ideal behavior and rigid structure is mounted on the end effector. Moreover, we assume that the robot manipulator is rigid, with no joint or motor compliance, backlash, or other nonlinearities.

Accordingly, the environmental impedance alone comprises the impedance of our robotic deburring and grinding process. Assuming such rigidity and robot joint/motor conditions is restrictive, and in work recommended to follow this study, such assumptions should be relaxed.

The impedance of the environment allows us to properly choose a controlled target impedance of the manipulator, together with control schemes along the two orthogonal directions in task space. Now from (2.21), we use the Laplace transforms, with Laplace operator  $s$ , to obtain the impedance matrix  $Z(s)$  as

$$Z(s) = B_e s + K_e = \begin{bmatrix} z_{nn} & z_{nt} \\ z_{tn} & z_{tt} \end{bmatrix} \quad (2.22)$$

where

$$z_{nn} = k_{vn} s + k_d$$

$$z_{nt} = k_{vt} s$$

$$z_{tn} = \mu [k_{vn} s + k_d]$$

$$z_{tt} = \mu k_{vt} s$$

we note that the diagonal terms in (2.22) are the impedance terms relating motion in one of the two orthogonal directions to forces in the respective directions. Moreover, we observe that in the normal direction,  $z_{nn}$  has both capacitive and resistive properties, while in the tangential direction  $z_{tt}$  has only resistive properties.

Having now derived expressions for grinding force-motion impedance, we will employ them in our control studies in Chapter III.



## Dynamics of Manipulators

For generality consider a manipulator composed of a set of  $n$  rigid bodies connected in a serial chain with friction acting at the joints. Using the Euler-Lagrange method, the dynamic system can be expressed as [6]:

$$M(q)\ddot{q} + C(q, \dot{q})\dot{q} + F_s(q) + G(q) = \tau - J^T F \quad (2.23)$$

where  $q$  is an  $n \times 1$  joint variable vector,  $\dot{q}$  is the time derivative of  $q$ ,  $M(q)$  is an  $n \times n$  inertia matrix,  $C(q, \dot{q})$  represents an  $n \times n$  matrix that describes the centrifugal and Coriolis terms in the dynamics of the manipulator,  $G(q)$  is an  $n \times 1$  vector containing terms arising from forces due to gravity,  $F_s(q)$  is the  $n \times 1$  vector that specifies the effects of Coulomb friction force of the joints,  $\tau$  is an  $n \times 1$  vector that defines input torques from the actuator of the manipulator,  $F$  is the  $n \times 1$  vector that defines the task space force or torque acting on the end effector of the manipulator, and  $J(q)$  is the  $n \times n$  manipulator task space Jacobian matrix. This Jacobian matrix is defined by [6]

$$J(q) = \frac{\partial L(q)}{\partial q} \quad (2.24)$$

where  $L(q)$  is a continuous function of the joint space vector found from manipulator kinematics and geometric relationships. It relates the  $n \times 1$  task space vector  $X$  to generalized joint coordinates  $q$  by

$$X = L(q) \quad (2.25)$$

Eq. (2.23) establishes the dynamic model of a manipulator for joint-based control, where the desired trajectory is available in terms of time histories of joint position, velocity, and acceleration, such as in free-motion control of manipulators. On the other hand, for constrained motions, when the end effector trajectories and interaction forces are described in a task space, such as in deburring and edge-following tasks, it is convenient to

use a description of the manipulator dynamics in task space. To obtain the manipulator dynamics in such a space, we first differentiate (2.25) twice with respect to time to obtain

$$\begin{aligned}\dot{X} &= J(q)\dot{q} \\ \ddot{X} &= J(q)\ddot{q} + \dot{J}(q)\dot{q}\end{aligned}\quad (2.26)$$

Solving for  $\ddot{q}$  yields

$$\ddot{q} = J^{-1}(q)(\ddot{X} - \dot{J}(q)\dot{q}) \quad (2.27)$$

Now use (2.26) and (2.27) in (2.23) to obtain

$$M_t(q)\ddot{X} + C_t(q, \dot{q})\dot{X} + F_{st}(q) + G_t(q) = F_{act} - F \quad (2.28)$$

where  $F_{act}$  represents the  $n \times 1$  force vector arising from robot actuator torques reflected at the end effector;  $M_t(q)$  and  $C_t(q, \dot{q})$  are  $n \times n$  matrices corresponding to the inertial matrix and velocity matrix terms in joint space; and  $G_t(q)$  and  $F_{st}(q)$  are  $n \times 1$  vectors reflecting the gravity term and friction force terms in joint space. These terms are given by

$$\begin{aligned}M_t &= J^{-T}(q)M(q)J^{-1}(q) \\ C_t &= J^{-T}(q)[C(q, \dot{q})J^{-1} - M(q)J^{-1}\dot{J}(q)J^{-1}(q)] \\ F_{st} &= J^{-T}(q)F_s(q) \\ G_t &= J^{-T}(q)G(q) \\ F_{act} &= J^{-T}\tau\end{aligned}\quad (2.29)$$

Notice that in (2.28), the dynamic state variables are described in task space. Because the coefficient matrices in (2.28) are dependent on the manipulator joint configurations, it is more convenient to express these matrices as functions of the joint variables  $q$  in Eq. (2.28).

In practical implementations, the task requirement is described in task space, while the control input, usually the robot motor torques  $\tau$ , are described in joint space. Moreover, encoders and tachometers are usually placed on motor shafts, such that

displacement and velocity measurements are completed in joint space. To analytically obtain motion of the end effector, "forward kinematics" is employed and computed. In such situations, the following expression for the manipulator dynamic system is more useful and convenient. It is obtained by directly substituting from (2.27) into (2.23).

$$M(q)J^{-1}(q)(\ddot{X} - \dot{J}(q)\dot{q}) + C(q, \dot{q})\dot{q} + F_s(q) + G(q) = \tau - J^T F \quad (2.30)$$

We will use this form of the manipulator dynamics in the design of control laws for deburring and grinding in Chapter III.

### SCARA Robot

One of the most popular commercial robots adaptable to the task of robotic deburring and grinding is a SCARA robot, illustrated in Figure 1.1. This robot has four degrees of freedom, consisting of rotation about two parallel vertical joints and translation and rotation about the tool axis. For the study herein, we are concerned with end-effector motion and force acting only in a horizontal plane. Accordingly, we employ a model with only two degrees of freedom, namely rotations of the two main arms of the SCARA robot about their vertical axes, as shown in Figure 2.4. Because gravity has no effect in the horizontal plane, the gravity term in (2.23) vanishes, and the dynamic equation in joint space for this simple model reduces to a second-order nonlinear differential equation given by [6]

$$M(q)\ddot{q} + C(q, \dot{q})\dot{q} + F_s(q) = \tau - J^T F \quad (2.31)$$

where  $q$ ,  $\tau$  and  $F$  are  $2 \times 1$  vectors as defined previously, and

$$M = \begin{bmatrix} m_{11} & m_{12} \\ m_{21} & m_{22} \end{bmatrix} \quad C = \begin{bmatrix} c_{11} & c_{12} \\ c_{21} & c_{22} \end{bmatrix}$$

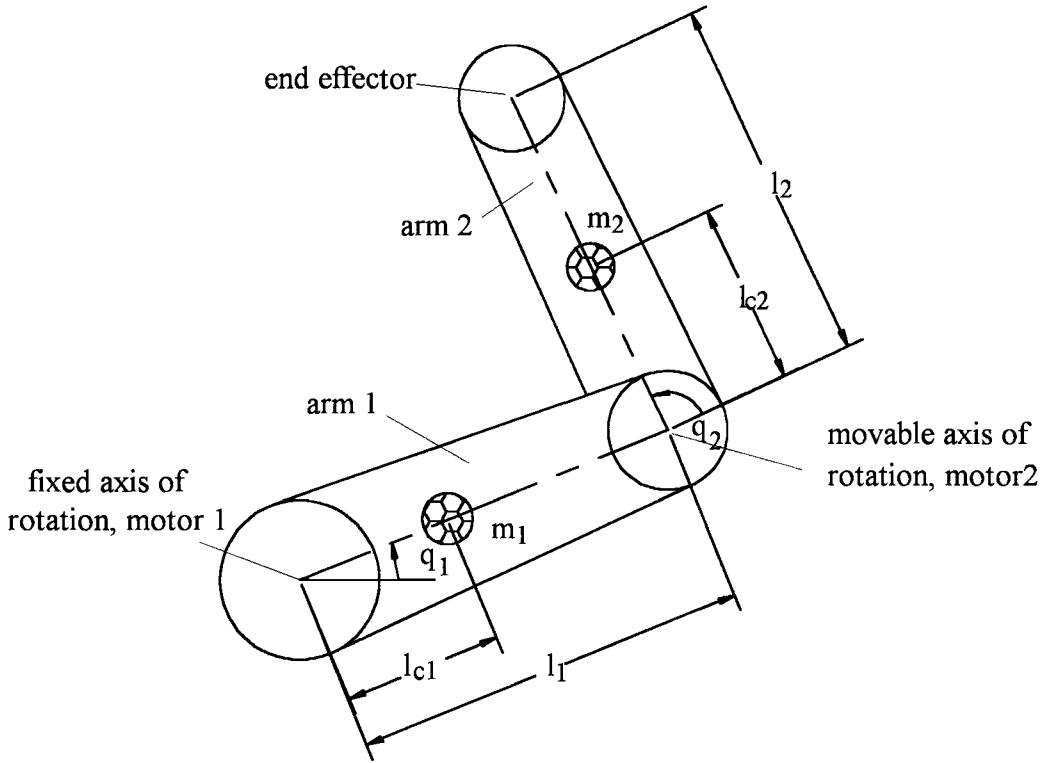


Figure 2.4 Schematic Diagram of Two-Arm SCARA Robot

with

$$m_{11} = p_1 + 2p_2 \cos(q_2)$$

$$m_{12} = m_{21} = p_3 + p_2 \cos(q_2)$$

$$m_{22} = p_3$$

$$c_{11} = -2p_2 \sin(q_2) q_2$$

$$c_{12} = -p_2 \sin(q_2) q_2$$

$$c_{21} = p_2 \sin(q_2) q_1$$

$$c_{11} = 0$$

where  $p_1$ ,  $p_2$ , and  $p_3$  are constant terms dependent on the manipulator's geometric dimensions and masses of components. For this study, we use the Berkeley SCARA robot [31] as a benchmark for our simulations because the parameters of the robot are available and because this robot is of an appropriate size for grinding and deburring. From [31] we have

$$\begin{aligned}
p_2 &= l_1 l_{c2} m_1 + l_1 l_2 m_p \\
p_3 &= I_3 + I_4 + I_p + (l_{2c}^2 m_4 + l_2^2 m_p) \\
p_1 &= I_1 + I_2 + I_{3c} + l_{1c}^2 m_2 + l_1^2 (m_3 + m_4 + m_p) + p_3
\end{aligned}$$

where  $I_1$  and  $I_3$  are rotor inertias of motor 1 and motor 2,  $I_2$  and  $I_4$  are inertias of link1 and link 2 about their own gravity center,  $I_{3c}$  is the stator inertia of motor 2,  $I_p$  is the payload inertia;  $m_1$  and  $m_3$  are the masses of motor 1 and motor 2,  $m_2$  and  $m_4$  are the masses of link 1 and link 2;  $l_1$  and  $l_2$  are the lengths of link1 and link 2, and  $l_{1c}$  and  $l_{2c}$  are the radii of gyration for link1 and link2. The Coulomb friction matrix is described by:

$$F_s = \begin{bmatrix} f_{s1} \\ f_{s2} \end{bmatrix}$$

$$f_{si} = \begin{cases} th_i \times \text{sign}(\dot{q}) & \left| \dot{q} \right| > 0 \\ th_i \times \text{sign}(q) & \left| \dot{q} \right| = 0 \text{ and } |q| > th_i \\ q_i & \left| \dot{q} \right| = 0 \text{ and } |q| \leq th_i \end{cases}$$

where  $th_i$ ,  $i = 1, 2$  is the magnitude of the friction force.

Similarly, from (2-28) the task space dynamics of this robot model is given by the second-order nonlinear differential equation

$$M_t(q) \ddot{X} + C_t(q, \dot{q}) \dot{X} + F_{st}(q) = F_{act} - F \quad (2.32)$$

with coefficient matrices defined by (2.29) and the appropriate matrices and vectors defined as for (2.31). To implement dynamic analysis and control based on (2.32), we define an  $x$ - $y$  horizontal reference system plane and a task space  $t$ - $n$  by two orthogonal axes normal and tangential to the surface at an idealized point of contact of the grinding tool, as shown in Figure 2.5. This is convenient because forces can easily be described and measured in the  $t$ - $n$  directions. Figure 2.5 illustrates joint space  $(q_1, q_2)$ , reference (fixed) space  $(x, y)$ , and task space  $(t, n)$  defined for a manipulator end-effector point

moving along an arbitrary curved edge. Accordingly, we define the task space coordinates and reference Cartesian space coordinate by

$$X = \begin{bmatrix} n \\ t \end{bmatrix} \quad \text{and} \quad Y = \begin{bmatrix} x \\ y \end{bmatrix}$$

where  $n$  is positive into the workpiece and normal to the contour of the edge at the end effector point of contact and  $t$  is orthogonal to  $n$ , positive in a right-hand coordinate system.

Notice that the task space coordinate system changes as the tool contact point moves along an arbitrary curved edge in the reference system. Consequently, we seek mapping relationships between robot joint space and task space in the following section.

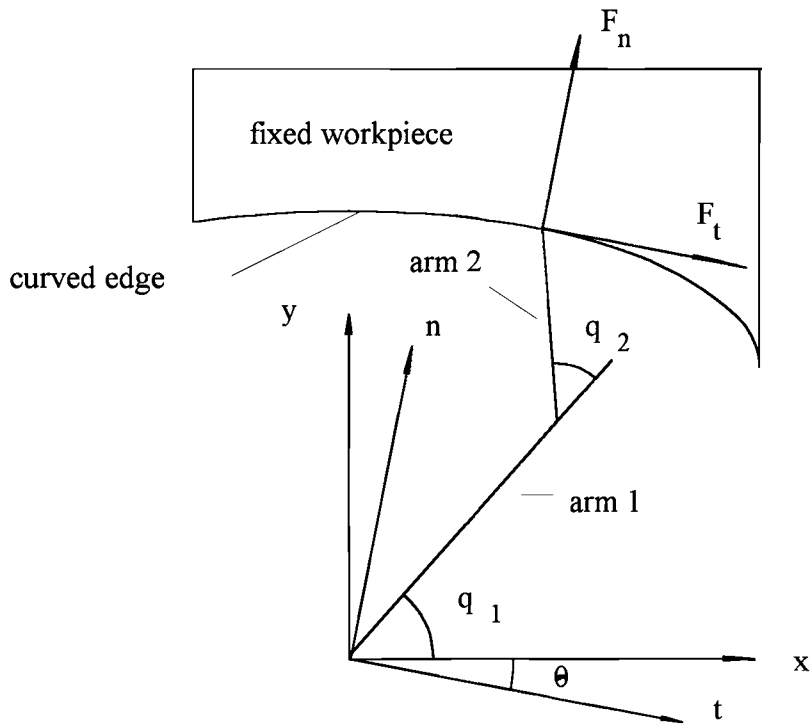


Figure 2.5 Schematic Diagram of Three Spaces for an Arbitrary Curved Edge

## Jacobian Matrix

It is difficult to directly express the task space coordinates as simple functions of joint space coordinates. Accordingly, we develop a two stage transformation, or mapping, first from joint space to reference space, and second from reference space to task space. The mapping from joint space to reference Cartesian space is straightforward and is given by

$$Y = \begin{bmatrix} x \\ y \end{bmatrix} = \begin{bmatrix} l_1 c_1 & l_2 c_{12} \\ l_1 s_1 & l_2 s_{12} \end{bmatrix} \begin{bmatrix} q_1 \\ q_2 \end{bmatrix} \quad (2.33)$$

$$\text{or} \quad Y = L_c q$$

where  $l_1 =$  length of link 1;  $l_2 =$  length of link 2

$$c_1 = \cos(q_1), \quad c_{12} = \cos(q_1 + q_2), \quad s_1 = \sin(q_1), \quad \text{and} \quad s_{12} = \sin(q_1 + q_2).$$

$$L_c = \begin{bmatrix} l_1 c_1 & l_2 c_{12} \\ l_1 s_1 & l_2 s_{12} \end{bmatrix}, \quad q = \begin{bmatrix} q_1 \\ q_2 \end{bmatrix}$$

From (2.24) and (2.33), the reference space Jacobian matrix  $J_c(q)$  is given by

$$J_c(q) = \begin{bmatrix} -l_1 s_1 - l_2 s_{12} & -l_2 s_{12} \\ l_1 c_1 + l_2 c_{12} & l_2 c_{12} \end{bmatrix} \quad (2.34)$$

To derive the task space Jacobian matrix to transform from reference space to task space, we need the geometric description of the curve to be followed in reference space. To illustrate this transformation and for use later in this study, suppose the curve to be followed is an ellipse, described by

$$(x - g)^2 / a^2 + (y - h)^2 / b^2 = 1 \quad (2.35)$$

where  $a$ , and  $b$  are the semi-major and semi-minor elliptical axes lengths and  $g$  and  $h$  are offsets of the center of the ellipse from the origin of reference frame. We assume in (2.35) that either the x-y system or the workpiece has been rotated such that the ellipse axes have been aligned with the x-y axes. At the end-effector contact point, the task space coordinates can be expressed in terms of the reference space coordinates by

$$X = L_{ct}(Y)$$

From Figure 2.5 and analytical geometry, it can be seen that

$$L_{ct}(Y) = \begin{bmatrix} n_0 \cdot i & n_0 \cdot j \\ t_0 \cdot i & t_0 \cdot j \end{bmatrix} \begin{bmatrix} x \\ y \end{bmatrix} \quad (2.36)$$

where  $i, j, n_0,$  and  $t_0$  are defined as unit vectors in the positive  $x, y, n,$  and  $t$  direction, respectively. Thus

$$i = \begin{bmatrix} 1 \\ 0 \end{bmatrix}, \quad j = \begin{bmatrix} 0 \\ 1 \end{bmatrix}$$

To determine the unit vectors  $n_0$  and  $t_0$  for our elliptical curve, we rewrite (2.35) as

$$f(x, y) = (x - g)^2 / a^2 + (y - h)^2 / b^2 - 1 = 0 \quad (2.37)$$

The gradient of an arbitrary curve in  $x, y$  space  $g(x, y) = 0$  is

$$\nabla g(x, y) = \frac{\partial g}{\partial x} i + \frac{\partial g}{\partial y} j \quad (2.38)$$

which is a vector normal to the curve at a point  $(x, y)$ , pointing to the direction of fastest increase of  $g$ . Consequently, the unit normal vectors  $n_0, t_0$  for our ellipse in (2.37) are given by

$$n_0 = \frac{\nabla f(x, y)}{\|\nabla f(x, y)\|} = \frac{1}{\Delta} \left[ i + \frac{a^2(y-h)}{b^2(x-g)} j \right]$$

or

$$n_0 = \frac{1}{\Delta} \begin{bmatrix} 1 \\ a^2(y-h)/b^2(x-g) \end{bmatrix} \quad (2.39)$$

where

$\|\cdot\|$  represents the magnitude of a vector, and

$$\Delta = \sqrt{1 + a^4(y-h)^2 / (b^4(x-g)^2)} \quad (2.40)$$

Since the unit tangential vector  $t_0$  is perpendicular to the unit normal vector, such that  $n_0 \cdot t_0 = 0$ , we may derive  $t_0$  as



$$t_0 = \frac{1}{\Delta} \begin{bmatrix} -a^2(y-h)/b^2(x-g) \\ 1 \end{bmatrix} \quad (2.41)$$

Now using the expressions for  $i$ ,  $j$ ,  $n_0$ , and  $t_0$  in (2.36), yields

$$L_{ct}(Y) = \frac{1}{\Delta} \begin{bmatrix} x + a^2 y^2 / (b^2 x) \\ (1 - a^2 / b^2) y \end{bmatrix}$$

By analogy to (2.24), the Jacobian matrix between task space and reference space

$$J_{ct} = \frac{\partial L_{ct}}{\partial Y} = \begin{bmatrix} j_{ct11} & j_{ct12} \\ j_{ct21} & j_{ct22} \end{bmatrix} \quad (2.42)$$

where

$$j_{ct11} = \frac{1}{\Delta^3} \left[ 1 + \frac{a^2}{b^2} (2 \frac{a^2}{b^2} - 1) \frac{y^2}{x^2} \right]$$

$$j_{ct12} = \frac{1}{\Delta^3} \left[ \frac{a^2}{b^2} (2 - \frac{a^2}{b^2}) \frac{y}{x} + \frac{a^6}{b^6} \frac{y^3}{x^3} \right]$$

$$j_{ct21} = \frac{1}{\Delta^3} (1 - \frac{a^2}{b^2}) \frac{a^4}{b^4} \frac{y^3}{x^3}$$

$$j_{ct22} = \frac{1}{\Delta^3} (1 - \frac{a^2}{b^2})$$

Then from (2.26) we may write

$$\dot{X} = \begin{bmatrix} \dot{n} \\ \dot{t} \end{bmatrix} = J_{ct} \dot{Y} \quad (2.43)$$

and

$$\dot{Y} = J_c \dot{q} \quad (2.44)$$

Now combining results from (2.43) and (2.44), we may complete the transformation from velocities in joint space to velocities in task space as

$$\dot{X} = \begin{bmatrix} \dot{n} \\ \dot{t} \end{bmatrix} = J_{ct} J_c \dot{q} = J \dot{q}$$

where

$$J = J_{ct} J_c$$

Accordingly, for our two degree-of-freedom SCARA robot with end-effector following an elliptical edge curve, we obtain the dynamic system equations (2.31) and (2.32) in the joint space and task space, respectively, by using the following relationships from linear algebra:

$$\begin{aligned} J &= J_{ct} J_c, & J^T &= J_c^T J_{ct}^T, & J^{-1} &= J_c^{-1} J_{ct}^{-1}, & \text{and} \\ \dot{J} &= \dot{J}_{ct} J_c + J_{ct} \dot{J}_c \end{aligned} \quad (2.45)$$

We have modeled the interaction forces for deburring and grinding and developed a dynamic model in task space for a two-link robot arm. In the next chapter we will employ these models to study control design for robotic deburring and grinding.

## **CHAPTER III**

### **CONTROL DESIGN AND ANALYSIS**

In this chapter, we design a controller to achieve good performance in robotic deburring and grinding based on the model developed in Chapter II. Desired performance and associated manipulator behavior will be discussed to understand the control objectives before we introduce a control strategy. Simple impedance and hybrid impedance control will also be investigated. A new controller with simultaneous control of position and force is proposed for robotic deburring and grinding.

#### **Manipulator Performance**

Consider the action of deburring and grinding the edge of a metal part, where a desired smooth edge contour lies beneath a rough edge. The task is to smooth by grinding or other metal cutting means the rough edge to the desired contour at a sufficiently fast rate. It is also desired to control the interacting contact forces for material removal during cutting action.

At the beginning of deburring and grinding, the manipulator carrying a grinding wheel or a finishing tool approaches the workpiece from free space, making contact with the workpiece at the end of this free space motion. Once the tool reaches the workpiece, the cutting process begins, with material removal proceeding continuously along the edges or surfaces of the workpiece. Accordingly, we seek a control structure or law such that

the manipulator maneuvers both in free-motion space and constrained space without any external hardware or software switch to change the control mode. Indeed, free motion may be considered a special case of constrained motion, where contact forces are zero and only reference motion is commanded. In constrained motion task space, control of both motion and force simultaneously is necessary. Position control in task space ensures accurate tracking of the desired trajectory, while force control is necessary for stable and continuous material removal without tool or workpiece damage. It is useful for our design to divide the analysis into two portions, namely motions and forces normal to and tangential to the workpiece edge contour at the contact point.

While deburring and finishing, the end effector is subject to cutting forces both in the normal and tangential directions. Such forces may vary widely due to unknown edge roughnesses of the workpiece. The normal force acts to push the tool and end effector away from the cutting point, such that large normal forces will cause the end effector to deviate from the desired trajectory. The control strategy must adjust the dynamics of the manipulator so that the end effector tracks the commanded trajectory as accurately as possible in the presence of the cutting forces. Such behavior requires the manipulator to have high stiffness, or high impedance, in the normal direction. The larger the impedance, the better the tracking performance.

In the tangential direction, cutting forces generated in deburring and grinding act to balance the energy input of the grinding wheel or cutting tool, which rotates about the tool axis at high speed. These forces also act on the end effector, tending to oppose the feed-in of the tool in the tangential direction. For a grinding wheel with hard bonding, large cutting forces cause either stall of the grinding wheel or damage to the edge or surface of the workpiece. Since the tangential cutting force is related to the normal force by grinding friction, large cutting forces also imply a potential drift of the tool away from the desired trajectory. Moreover, large cutting forces applied to the manipulator may excite tool chatter or oscillation of the manipulator. Consequently, it is desirable for the

manipulator to have high compliance, or low impedance, in the tangential direction. As mentioned in Chapter I, infinite impedance implies pure position control, while zero impedance implies pure force control. Unfortunately, the robot structure limits the ability to obtain good control of both position and force in the same direction at the same time, such that an acceptable tradeoff is needed between position and force control.

In a simple deburring operation, we may need only a bounded cutting force to guarantee stable interaction, and position accuracy may not be critically important. However, in precision deburring and grinding, position control in the normal direction may be more important than precise force control, as long as a stable interaction is maintained. Thus, in the normal direction, position control would have priority, while the force is controlled simply to achieve stable interaction. In the tangential direction, ample cutting force is critical to material removal. Maintaining a constant cutting force is usually important to achieve good finishing quality. Thus, the tangential tool velocity should be adjusted to maintain a nearly constant cutting force, provided the position trajectory is tracked well. Therefore, force control may be more critical than position control in the tangential direction.

In the types of deburring and edge finishing considering in this study, we assume that burrs are irregular, unpredictable, and unmeasurable, such that variations of the cutting force will occur. This can be seen from (2.5) and (2.6) in Chapter II, where the depth of cut  $d$  effectively varies with changes in surface roughness or burr height. Controlling force at a constant level under irregular and unpredictable material volume removal rate is difficult. It may be more feasible to suppress the variation of the cutting force into an allowable range. The allowable variation of the cutting force is dependent on the robot structure and dynamics. In conventional grinding or milling processes, rough edges or surfaces also cause variation of cutting forces. However, because the tool holders and machine spindle are designed with high stiffnesses, such variations of forces are accommodated with little path deviation as long as these forces remain below specified

limits. With a more compliant structure, robotic deburring and grinding typically yields more path deviation with cutting force variation. Maintaining forces above a specified minimum force ensures continuous cutting and no loss of contact with the workpiece. Maintaining force below a specified maximum force avoids degradation of finish quality and undesired phenomena such as chattering and oscillation. Our goal for force control of the manipulator will be to control the variation of cutting forces within an allowable range, rather than maintain a constant force.

The traverse or tangential velocity of the grinding wheel spindle along the edges of the workpiece is limited by the dynamics of the robot and the geometry of the workpiece and its surface roughness. Because the workpiece is fixed during grinding, the frequency content of the rough edge, as seen from the end effector, are dependent on the traverse speed of the end effector, as well as the surface roughness of the workpiece. Increasing the traverse speed increase this frequency. Excessive frequency content in the cutting forces may either separate the end effector from the workpiece, or require excessive normal force to maintain contact. Therefore, tangential speeds for the end effector typically must be maintained below some maximum. On the other hand, lower traverse speeds in conjunction with certain burr frequencies may approach the natural frequency of the system, causing resonance and damage. Hence, certain low and intermediate speeds must be avoided. Since the surface roughness is unknown in general, such speeds would need to be located by trial and error.

From these considerations, we suggest an alternative control strategy by which the interaction or normal force is controlled within an allowable range, the tangential velocity of the end effector is controlled for adequate cutting, and position control in both directions is used to track a specified trajectory.

## Control Architecture

As shown previously, the equations of motion for our two degree of freedom SCARA robot are nonlinear and coupled. Direct analysis of such coupled nonlinear control systems is not possible. Generally, linearization of manipulator dynamics is used to overcome this problem. Thus, before considering the design of position and force controllers, we first linearize the manipulator dynamics to obtain a suitable control structure.

There exist in the literature some effective linearization methods for the control of manipulators. For example, local linearization in a small neighborhood of an operating point [21] is often used so that linear control methodologies may be applied. Alternatively, in robot control, it is more common to use a control algorithm called computed-torque control [6], which is a special application of feedback linearization, to deal with the manipulator dynamic nonlinearities. This approach is considered to be the most well-suited for robot dynamics and can be used to achieve good control performance, provided the dynamics of the system are known accurately. In this thesis, we employ this method to establish our control structure.

For convenience, we repeat below the general manipulator dynamic equation given by (2.30) in Chapter II, namely

$$M(q)J^{-1}(q)(\ddot{X} - \dot{J}(q)\dot{q}) + C(q, \dot{q})\dot{q} + F_s(q) + G(q) = \tau - J^T F \quad (3.1)$$

Following [30], consider a basic feedback control law structure for robot actuator torque given by

$$\tau = \alpha v + N \quad (3.2)$$

where  $v$  is the "servo" portion of the control law and is designed based on an error signal to be defined below;  $\alpha$  is a term which will be later defined to decouple the feedback-

controlled manipulator; and  $N$  is a term defined below to cancel the nonlinear terms in the complete dynamic system. The control law in (3.2) establishes an inner control loop, shown in Figure 3.1, and is designated the model-based portion of our controller. From inspection of (3.1), we use the strategy described by Craig [30] by selecting

$$\alpha = M(q)J^{-1}(q) \quad (3.3)$$

$$N = -M(q)J^{-1}(q)\dot{J}(q)\dot{q} + C(q,\dot{q})\dot{q} + F_s(q) + G(q) + J^T F$$

Then the model-based portion of our control law in (3.2) becomes

$$\tau = M(q)J^{-1}(q)v - M(q)J^{-1}(q)\dot{J}(q)\dot{q} + C(q,\dot{q})\dot{q} + F_s(q) + G(q) + J^T F \quad (3.4)$$

Equation (3.4) is the control law of the manipulator with perfect nonlinear compensation, dynamic decoupling, and contact force compensation. It requires accurate knowledge of the dynamics of manipulators and perfect sensors for the measurement of forces, positions and velocities. Moreover, it requires fast, real-time computation by the control processor of all the terms on the right side of (3.4), which necessitates a fast and powerful computer with efficient software. In practical implementation, modeling and measurement errors always exist. This may cause corresponding errors in (3.4), such that the nonlinear terms will not be completely canceled. These errors will degrade dynamic behavior of the controlled system in rather complicated ways [30], and analysis of such errors was judged to be beyond the scope of this thesis. To overcome this problem, advanced techniques and control strategies such as on-line estimation and adaptive control might be employed [32], [33]. On the other hand, advanced control approaches require solution of significantly more complicated mathematical expressions, leading to significant increases in computation time. In general, faster and more powerful control processors would be required, increasing implementation difficulties. As a trade-off, in this study, we assume the dynamics are known exactly and the sensors are ideal. It is a topic for future research study to investigate advanced and efficient control approaches for robotic deburring and grinding.



Substitution of the right side of (3.4) in (3.1) yields

$$\ddot{X} = v \quad (3.5)$$

According to our assumption in (3.2), (3.5) shows that the acceleration of the manipulator end effector is equal to the error driven portion of the control law. It means that if we properly design the servo controller  $v$  so that (3.5) holds during the time intervals of interest, the desired motion of the manipulator will be achieved from torque acting according to (3.4).

With the total control law consisting of (3.4), and (3.5), we discuss in the following sections the design of an error-driven controller  $v$ , using impedance control and other control theories.

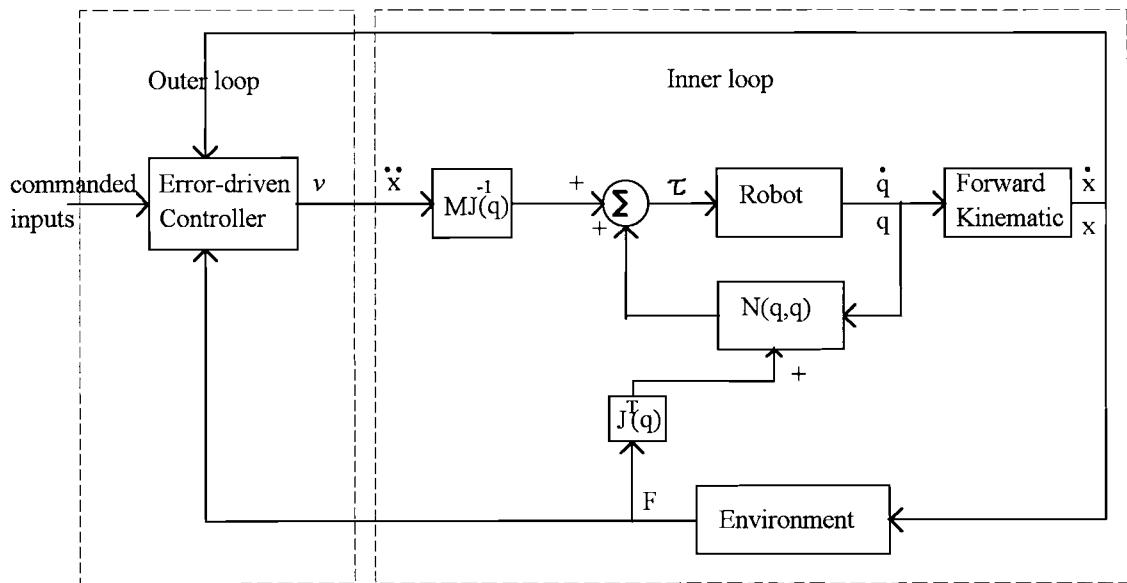


Figure 3.1 Diagram of Control Structure

## Impedance Control

The deburring process requires a controller for the end-effector to track the desired trajectory while accommodating the force produced by the cutting process and maintaining it within limits. On the other hand, impedance control [18] regulates the relation of position to force. By controlling manipulator motion and in addition specifying an impedance relationship between force and deviation from that motion, we may be able to control both motion and force, effecting a tradeoff between position and force control. Changing the impedance can modulate and control the interaction. Thus, conceptually, impedance control would be suitable for control of the deburring process. With impedance control it is unnecessary to specify a command force.

An impedance control strategy suggested by Hogan [18] is to derive a control law directly from the target impedance and dynamic model of the manipulator. Assume the target impedance  $Z(s)$  of the manipulator is

$$Z = M_d s^2 + B s + K \quad (3.6)$$

where  $s$  is the Laplace variable,  $Z(s)$  is a  $2 \times 1$  impedance matrix,  $M_d$ ,  $B$ , and  $K$  are constant  $2 \times 2$  desired inertia, damping, and stiffness matrix, respectively, specified by designers according to the desired dynamic behaviors of the controlled system. In the time domain, the corresponding force-motion relationship is [18]

$$M_d \ddot{X} + B(\dot{X} - \dot{X}_d) + K(X - X_d) = -F \quad (3.7)$$

where

$X$  = position vector in task space

$X_d$  = desired position vector in task space

$F$  = external force acting on the end effector.

The minus sign on the right side of (3.7) occurs because the external force from a passive environment opposes the motion of the end-effector. Solving for  $\ddot{X}$  gives

$$\ddot{X} = -\frac{1}{M_d} [F + B(\dot{X} - \dot{X}_d) + K(X - X_d)] \quad (3.8)$$

Recall the manipulator dynamics equation (2.28) in task space, repeated here as

$$M_t(q)\ddot{X} + C_t(q, \dot{q})\dot{X} + F_{st}(q) + G_t(q) = F_{act} - F \quad (3.9)$$

Substituting from (3.8) into (3.9) and solving for  $F_{act}$  yields control law torque as

$$\tau = J^T F_{act} = J^T [G_1 F + G_2 \Delta \dot{X} + G_3 \Delta X + N_1] \quad (3.10)$$

where we have defined errors  $\Delta \dot{X}$  and  $\Delta X$  by

$$\Delta \dot{X} = \dot{X}_d - \dot{X}$$

$$\Delta X = X_d - X$$

and gains  $G_1$ ,  $G_2$ , and  $G_3$  by

$$G_1 = I - M_t(q)M_d^{-1}, \text{ with } I = \text{unit matrix}$$

$$G_2 = M_t(q)M_d^{-1}B$$

$$G_3 = M_t(q)M_d^{-1}K$$

and have defined the new term  $N_1$  by

$$N_1 = C_t(q, \dot{q})\dot{X} + F_{st}(q) + G_t(q)$$

The control law in (3.10) is nonlinear [27] owing to the dependence of the gains and other quantities on joint position and velocity. Essentially, this control law resembles a proportional plus derivative (PD) position control, plus nonlinear force feedback control with quantity  $N_1$ . As seen from (3.10), the gains in the impedance control law are directly related to the desired mass and the system mass.

Typically, if the manipulator is in contact with an environment whose dynamics together with that of a force sensor are modeled as a spring, then the force generated by interaction with the environment is given by

$$F = K_e(X - X_d) \quad (3.11)$$

where  $K_e$  is a positive matrix representing the stiffness of the environment. Using (3.11) in (3.10), gives for the control law

$$\tau = J^T F_{act} = J^T [(G_1 K_e + G_3) \Delta X + G_2 \Delta \dot{X} + N_1] \quad (3.12)$$

Solving for  $F_{act}$  and substituting in (3.9) gives for the total system with this impedance control law

$$M_d \ddot{X} + B(\dot{X} - \dot{X}_d) + (K + K_e)(X - X_d) = 0 \quad (3.13)$$

The closed-loop system (3.13) is linear with constant parameter matrices and holds for an ideal model with complete knowledge of manipulator and environmental (including sensors) dynamics. If all the parameter matrices in the (3.13) are real and positive-definite, the total system will be stable [21]. Note that in the position gain  $(K+K_e)$ , the environmental stiffness  $K_e$  will typically be much larger than the manipulator desired stiffness  $K$  for deburring and grinding, such that the position gain will be dominated by the environmental stiffness. In such cases, if the desired manipulator damping matrix  $B$  is selected considering only the desired manipulator stiffness  $K$ , the closed-loop system will be underdamped and oscillatory, and will perform poorly [25]. The block diagram for impedance control using (3.9), (3.10) and (3.11) is illustrated in Figure 3.2.

In impedance control with a target impedance described by (3.6), contact forces are determined by position and velocity deviation from desired trajectories through (3.7). Equation (3.7) implies that if the end-effector remains close to the desired trajectory and velocity, then interaction forces are small. Otherwise, large interaction forces occur to prevent the end-effector from moving away from the desired trajectory. In contrast, for manipulators engaged in deburring and grinding, large depths of cut will result in large interaction forces to force the end-effector close to the desired trajectory. To reach a specified desired contour, forces determined by the cutting process, rather than mere contact forces, are required. If (3.7) is directly applied to deburring and grinding, large interaction forces will cause the end-effector to drift from the desired contour. Observing the motion-force relation (2.21) developed in Chapter II, we modified the target impedance relationship (3.7) for deburring and grinding to

$$M_d \ddot{X} + B(\dot{X} - \dot{X}_d) + K(X - X_d) = -(F - F_d) \quad (3.14)$$

where desired force  $F_d$  is a nominal grinding force vector required to remove materials and reach the desired contour. Eq. (3.14) indicates desired forces should be commanded, along with desired position and velocity, in using the target impedance for deburring and grinding tasks. We will evaluate these two versions of impedance control approach in Chapter IV.

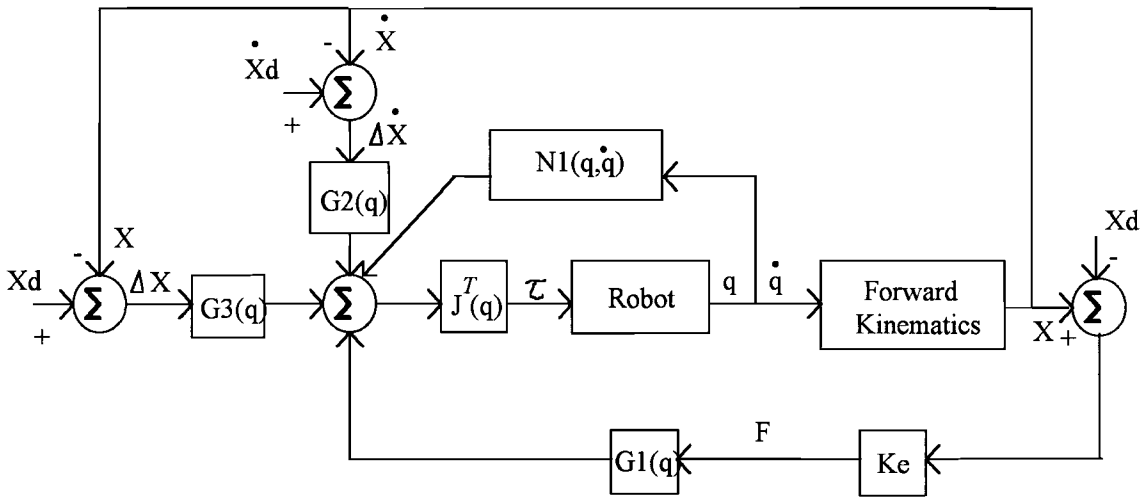


Figure 3.2 Block Diagram of Impedance Control with Spring-Like Environment

### Hybrid Impedance Control

Hybrid impedance control employs characteristics of both hybrid position/force control and impedance control. In implementing this strategy, we consider the normal and tangential directions at the contact point, along which either impedance position or impedance force control is employed.

The key to hybrid impedance control is modeling the impedance of the environment, because the environmental impedance determines the control strategies to be employed. Once the environmental impedance is modeled, it is used to design the target

impedance of the manipulator to ensure stability and achieve the desired closed loop behavior of the manipulator. The manipulator impedance and achievable control strategy are governed by the duality principle proposed by Anderson and Spong [24]. The duality principle of impedances between manipulator and environment states that if the environmental impedances are capacitive, then there should be force control with noncapacitive manipulator impedances; if the environmental impedances are inertial, then position control with noninertial manipulator impedance should be applied; if the environmental impedance is resistive, either force control with inertial manipulator impedances or position control with capacitive manipulator impedances should be applied.

In Chapter II we derived the environmental impedance for deburring and edge finishing processes. Our analysis showed in (2.21) that for both the tangential and normal directions, coupling impedances, or non-zero off-diagonal terms existed in this matrix. In the development that follows, we will ignore these coupling terms, assuming the diagonal terms will dominate the nature of the relationship of motion and force in a given direction. This approximation provides the basis for hybrid impedance control applied in this study. This is consistent with all other investigations found in the literature, none of which considered coupling impedances. In fact, an approach for handling coupling impedance apparently does not exist. Following our approximation, we consider the environmental impedance in the normal direction to be capacitive, while the environmental impedance in the tangential direction is resistive. The capacitive environmental impedance implies a spring-like environment, and by the duality principle [24] requires a noncapacitive impedance for the manipulator and force control in the normal direction. Other choices of the manipulator impedance and control strategy will result in non-zero steady-state error. On the other hand, since the tangential environmental impedance is resistive, the manipulator impedance in the tangential direction should be either inertial or capacitive, and correspondingly, the control strategy in this direction will be force control or position control, respectively. Apparently, because of the nature of the deburring and finishing

task, capacitive impedance and position control is preferred in the tangential direction [9]. According to our definitions of impedance in (1.4) in Chapter I, a capacitive impedance consists of a spring-like term with or without a damping or an inertia term, such that  $Z(0) = \infty$ ; a resistive impedance consists of a damping term with or without an inertia term, such that  $Z(0) = \text{non-zero constant}$  [24]. Accordingly, our target manipulator impedances are given by

$$\begin{aligned} \text{normal direction:} \quad & Z_n = m_{dn}s + b_{dn} && \text{(non-capacitive)} \\ \text{tangential direction:} \quad & Z_t = m_{dt}s + b_{dt} + k_{dt} / s && \text{(capacitive)} \end{aligned} \quad (3.15)$$

The corresponding target relationships of motion and force are

$$\begin{aligned} \text{normal direction:} \quad & m_{dn} \ddot{n} + b_{dn} \dot{n} = -(F_n - F_{dn}) \\ \text{tangential direction:} \quad & m_{dt} (\ddot{t} - \ddot{t}_d) + b_{dt} (\dot{t} - \dot{t}_d) + k_{dt} (t - t_d) = -F_t \end{aligned} \quad (3.16)$$

where  $n$  and  $t$  represent displacements in the normal and tangential directions, respectively;  $m$ ,  $b$ , and  $k$  are positive scalars representing desired mass, damping, and stiffness respectively; subscripts  $n$  and  $t$  denote normal and tangential directions, respectively, and subscript  $d$  indicates desired parameters. Now represent (3.16) in matrix form by

$$M_d (\ddot{X} - S \ddot{X}_d) + B_d (\dot{X} - S \dot{X}_d) + K_d S (X - X_d) = -(F - S' F_d) \quad (3.17)$$

with  $X = \begin{bmatrix} n \\ t \end{bmatrix}$ , and  $S + S' = I$

where

$F$  and  $F_d$  are  $2 \times 1$  external force vector and desired force vectors, respectively.

$X$ ,  $\dot{X}$  and  $\ddot{X}$  are actual position, velocity, and acceleration  $2 \times 1$  vectors, respectively.

$X_d$ ,  $\dot{X}_d$  and  $\ddot{X}_d$  are reference position, velocity, and acceleration  $2 \times 1$  vectors, respectively.

$M_d$ ,  $B_d$  and  $K_d$  are positive diagonal  $2 \times 2$  matrices representing target impedance parameters.

$S$  and  $S'$  are selection matrices defined as diagonal with either ones or zeros on the diagonal. Ones for diagonal entries of  $S$  mean position control is in effect, while zeros indicate force control.  $I$  is the  $2 \times 2$  unit square matrix.

We desire to reshape the dynamics of the controlled manipulator so that its behavior satisfies (3.17). Since the position and velocity of the end effector and the interacting force are measurable, we rewrite (3.17) as

$$\ddot{X} = S \ddot{X}_d - M_d^{-1} [B_d (\dot{X} - S \dot{X}_d) + K_d S (X - X_d) + (F - S' F_d)] \quad (3.18)$$

The right side of (3.18) includes the state variables, interacting force, commanded force and trajectory in task space, and target impedance parameters, which are specified by a designer according to the desired dynamic performance of the manipulator coupling with the environment. Eq. (3.18) gives the manipulator acceleration required for obtaining this target impedance. Comparing (3.18) with the error driven control in (3.5) in the control structure, gives

$$v = S \ddot{X}_d - M_d^{-1} [B_d (\dot{X} - S \dot{X}_d) + K_d S (X - X_d) + (F - S' F_d)] \quad (3.19)$$

Eq. (3.19) describes the outer-loop control in Figure 3.1, where the "error" between commanded inputs and outputs is given by the right side of (3.19). Eq. (3.4) and (3.19) establish the control laws for hybrid impedance control of the manipulator with constrained motion. A block diagram for this hybrid impedance control approach is given in Figure 3.3.

The parameters for noncapacitive manipulator impedance and force control in the normal direction will typically yield overall small impedance values, while the parameter for capacitive manipulator impedance and position control in the tangential direction will typically yield high impedance values. Such choices for manipulator impedances may be suitable for cases such as edge-following or peg-in-the-hole problems, where non-zero



contact force is assumed in the normal direction and zero force assumed in the tangential direction. However, as we discussed previously, the task of robotic deburring or finishing requires large and small, but non-zero, impedances in the normal and tangential directions, respectively, so that the end effector may track close to the desired trajectory in the normal direction while accommodating the cutting force in the tangential direction. Although force control in the normal direction is able to provide stable contact with the environment, motion in this direction is provided indirectly by force adjustment, instead of directly by control of position and velocity. Consequently, large position and velocity errors may occur with this control approach. On the other hand, good motion-tracking in the tangential direction may not be able to adjust the velocity to accommodate the forces in this direction.

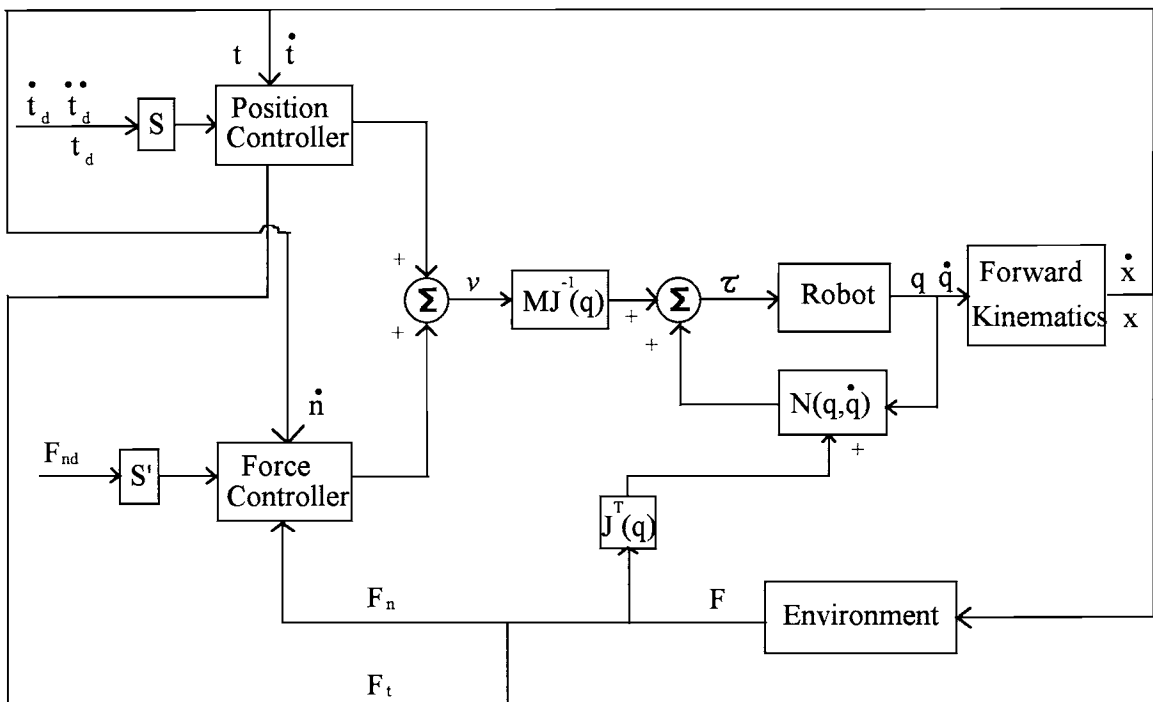


Figure 3.3 Diagram of Hybrid Impedance Control

## Simultaneous Position and Force Control

For the high stiffness environment encountered in robotic deburring and finishing, simple impedance control may cause large contact force or oscillations at the beginning of contact. In practical implementation, large oscillations in transient response, together with any dynamic modeling errors may cause unstable behavior of the manipulator [25].

Hybrid impedance control uses force control in the normal direction to achieve stable behavior of the manipulator. However, the performance may deviate substantially from the required trajectory. We seek a control law by which a manipulator in contact with a high stiffness environment will achieve good performance with highly accurate trajectory tracking while maintaining a suitable force. This means it is necessary to control position and force simultaneously in the same direction.

We assume that the manipulator dynamics are known and that sensors are available to measure all required variables. This implies that the dynamic model of the controlled manipulator can be dynamically decoupled and completely compensated to remove nonlinearities, such that the model-based control law presented in (3.5) is used. We require a design for the linear error-driven portion of the controller such that desired performance can be achieved.

Consider again any impedance-like control law. As observed previously, under the assumption of perfect dynamic decoupling and nonlinear compensation, such controllers are essentially PD-type controls with force feedback. Typically, in impedance-like control, regulation of the interaction force is obtained indirectly by control of position associated with a specified impedance relationship. Measured interaction force is directly fed back to modify the control output. It is this force feedback term that can cause large oscillation and unstable contact. Reviewing the total control law for impedance-like controls, we learned that they consist of linear combinations of motion error terms and force terms.

This analysis motivates our assumption that the controlled force command is composed of the simple addition of a sub-command for the motion portion and a sub-command for the force portion. In the force portion, the actual force should be compared to a desired force to yield force errors, which multiplied by carefully selected gains, will drive the force sub-command of the controller. Accordingly, we compose our controller according to

$$v = v_p + v_f \quad (3.20)$$

where  $v_p$  represents the sub-command for motion compensation and  $v_f$  represents the sub-command for force compensation. A simple and effective approach is to design the sub-controllers using PID (proportional plus integral plus derivative) or other simple controllers. We may consider this control scheme as an extension or modification of impedance control.

Notice that different combinations of proportional, integral, and derivative terms result in different weights for the position sub-control and force sub-control. We found, for example, that good results could be obtained by using PID position plus I (integral) force control in the normal direction, since both position and force should be controlled in this direction, and the accuracy of position control is more important than that of force control. In the tangential direction, since cutting force is directly related to normal force by grinding friction, motion control with a PD controller is used to guarantee the trajectory tracking in this direction. We avoid derivative force control because of the difficulty in obtaining force derivatives from measured force, which typically contains high frequency components. As a result of such choices, we have

$$\begin{aligned} \text{normal direction:} \quad v_n &= \ddot{n}_d + k_{np} e_{pn} + k_{nd} \dot{e}_{pn} + k_{ni} \int e_{pn} dt + kf_{np} e_{fn} + kf_{ni} \int e_{fn} dt \\ \text{tangential direction:} \quad v_t &= \ddot{t}_d + k_{tp} e_{pt} + k_{td} \dot{e}_{pt} + k_{ti} \int e_{pt} dt + kf_{tp} e_{ft} + kf_{ti} \int e_{ft} dt \end{aligned} \quad (3.21)$$

where error terms  $e$  are defined by

$$e_{pn} = n_d - n, \quad e_{pt} = t_d - t$$

$$\begin{aligned}\dot{e}_{pn} &= \dot{n}_d - \dot{n}, & \dot{e}_{pt} &= \dot{t}_d - \dot{t} \\ e_{fn} &= F_{nd} - F_n, & e_{ft} &= F_{td} - F_t\end{aligned}$$

$k_{np}$ ,  $k_{nd}$ , and  $k_{ni}$  are positive scalars representing proportional, derivative, and integral position gains in the normal direction, respectively;  $k_{tp}$ ,  $k_{td}$ , and  $k_{ti}$  are positive scalars representing proportional, derivative, and integral position gains in the tangential direction, respectively;  $kf_{np}$  and  $kf_{ni}$  are positive scalars representing proportional, and integral force gains in the normal direction;  $kf_{tp}$  and  $kf_{ti}$  are positive scalars representing proportional, and integral force gains in the tangential direction.  $F_{nd}$  and  $F_{td}$  are desired forces in the normal and tangential direction, respectively. Eq. (3.4), (3.20) and (3.21) consist of the control law for simultaneous position/force control approach. Figure 3.4 provides a block diagram for the control given by this approach.

Using simultaneous position/force control, we are able to simultaneously control both position and force within specific ranges. To achieve very accurate position control, we must obviously relinquish force control. This may be accommodated by specifying gain values for force control to zero or very small values. Similarly, to achieve accurate force control, we must relinquish accurate position control. This can be accommodated by specifying small gain values for position control while assuring that stable control with good transient performance is obtained.

One of the advantages of this control approach is the ability to switch the control between position-dominated control and force-dominated control by simply changing the gain values of the controller in real-time, as indicated in Fig. 3.4. For instance, if burrs are small and grinding forces remain below allowed maximum forces  $F_{limit}$ , then position accuracy remains dominant, and motion control will be applied by setting large position gains and zero force control gain. Once large burrs are encountered and grinding forces, measured with a force sensor approach limits, gains may be switched to control the grinding forces below specific limits with position gains set to relative small values.

However, such gain changing in real time to switch control between position-dominated and force-dominated control may cause stability problems if such switches are frequent. We assume that gains for the two modes have been chosen such that the system is stable with good performance while operating in either mode. Then if switches occur during near steady state response of the previous control mode, control may remain stable. On the other hand, if switches occur during the transient response of the previous control mode, instability may result. Such situations could occur in practice when burrs are extremely sharp and frequent. In such cases, multiple passes of deburring and grinding, with relatively small variations of burr heights for each pass, may be required to avoid frequent switches of control modes.

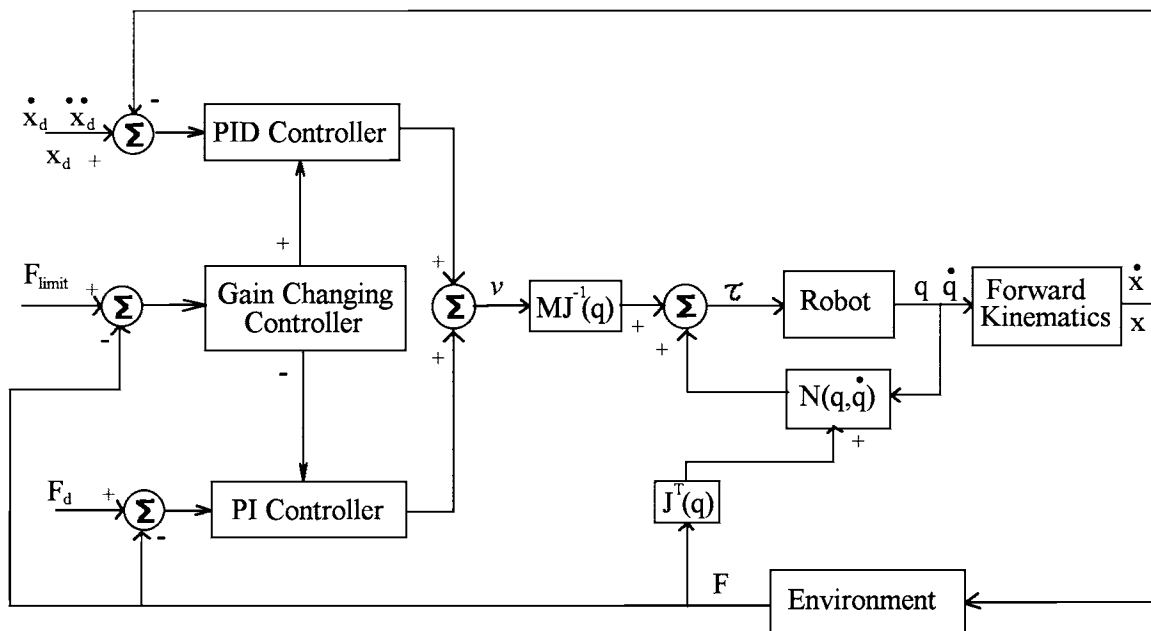


Figure 3.4 Control Diagram of Simultaneous Position/Force Control

We have discussed and proposed several control approaches which may be suitable for robotic deburring and grinding. To test the performance of these controllers in Chapter IV, we will simulate robotic deburring and grinding by employing different

controllers discussed in this chapter. The results of these simulations will be use to evaluate each controller type.

## CHAPTER IV

### SIMULATIONS AND RESULTS

#### Simulations

Simulations in this study were implemented using the Berkeley model SCARA robot, whose dynamics were presented in Chapter II. This model robot was selected because its size and weight seemed appropriate for light-duty deburring and finishing small parts. The values of parameters for this robot used in Eq. (2.31) are [31] :

$$I_1 = 0.2675 \text{ kg.m}^2, I_2 = 0.36 \text{ kg.m}^2, I_3 = 0.0077 \text{ kg.m}^2, I_4 = 0.051 \text{ kg.m}^2,$$

$$I_{3c} = 0.04 \text{ kg.m}^2, I_p = 0.046 \text{ kg.m}^2;$$

$$m_1 = 73 \text{ kg}, m_2 = 10.6 \text{ kg}, m_3 = 12 \text{ kg}, \text{ and } m_4 = 4.85 \text{ kg}, m_p = 6.81 \text{ kg};$$

$$l_1 = 0.36 \text{ m}, l_2 = 0.24 \text{ m}, l_{1c} = 0.139 \text{ m}, \text{ and } l_{2c} = 0.099 \text{ m};$$

$$th_1 = 5.5 \text{ N-m}, \text{ and } th_2 = 0.9 \text{ N-m}.$$

The maximum torques for motor 1 and 2 are 245.0 N-m and 39.2 N-m, respectively.

These torque limits were applied as a saturation function in the simulation program to avoid overloads of robot actuators.

The Berkeley SCARA robot has been verified in [31] as a benchmark for evaluating various control algorithms. To assist validation of our simulation of this robot in task space, we used results from our simulation to drive an animation of the two-arm Berkeley robot motion, as shown in Fig.4.1. Smooth and continuous motion of both arms indicated reliable modeling and programming. However, more complete validation of the

dynamic model was obtained during simulations evaluating different control approaches described later in this chapter.

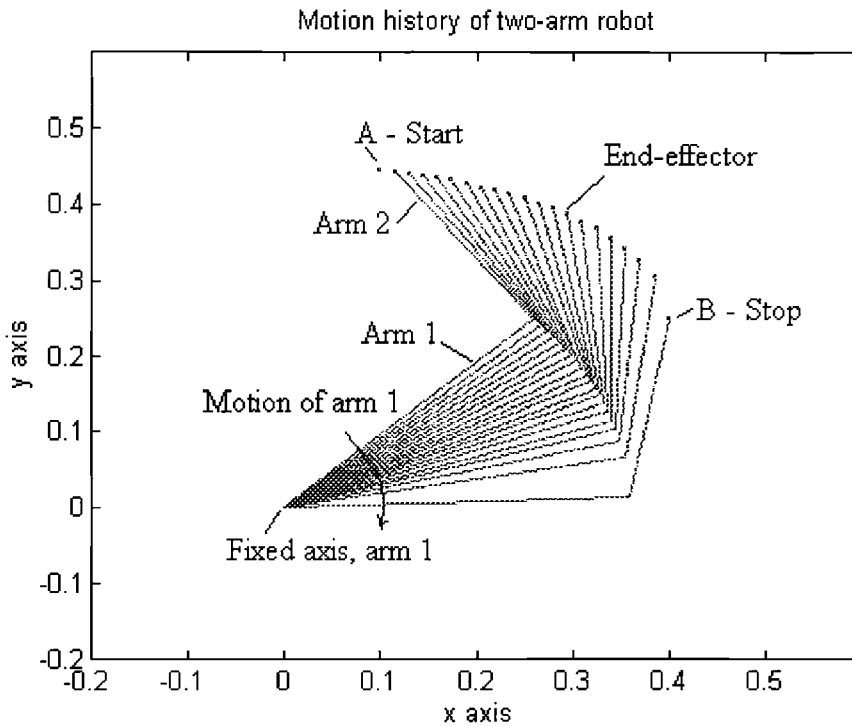


Figure 4.1 Motion History of Two-arm Berkeley SCARA Robot

The workpiece to be deburred and finished in our example is a steel plate with a thickness of 10 mm, which we take as the active width of cut  $b$ . We assume the grinding wheel diameter is large compared to both burr heights and the thickness of the workpiece. The diameter of grinding wheel is selected as 50.8 mm (2 inches), and we also assume that grinding conditions, wheel dressing, and rotary speed of the grinding wheel are the same as described for experiments in [29]. Thus we use values for the metal removal parameter  $\Lambda_m$  obtained from these experiments, which ranged from  $1.2644423 \times 10^{-7}$  to  $1.0115538 \times 10^{-9}$  m<sup>3</sup>/min. kg (0.00035 to 0.0028 in<sup>3</sup>/min. lb). For simplicity, in all the simulations in this study, we chose  $\Lambda_m = 1.0 \times 10^{-8}$  m<sup>3</sup>/min. kg and grinding friction coefficient  $\mu=0.7$ .



In the simulation examples herein, two types of desired edge contours for the workpiece were selected, namely, a straight line and an elliptical curve. These selections arose because most complex edges are combinations of lines and arcs. Using these desired contours, position trajectories in reference space were generated within the active workspace of the manipulator so as to avoid singularities of the Jacobian matrix describing manipulator dynamics. For straight line contours, most simulations employed a constant tangential speed of the end-effector in task space. However, impulse acceleration is required at the start and finish of such a trajectory. Thus for some simulations, we generated tangential position using linear segments with parabolic blends (LSPB) [6], given by

$$\mathbf{x}_t = \begin{cases} \mathbf{x}_{t_0} + \mathbf{a}_t t^2 / 2 & 0 \leq t \leq t_b \\ (\mathbf{x}_f + \mathbf{x}_{t_0} - V_t t_f) / 2 + V_t t & t_b < t \leq t_f - t_b \\ \mathbf{x}_f - \mathbf{a}_t t_f^2 / 2 + \mathbf{a}_t t_f t - \mathbf{a}_t t^2 / 2 & t_f - t_b < t \leq t_f \end{cases} \quad (4.1)$$

where

$\mathbf{x}_t$ ,  $\mathbf{x}_{t_0}$ , and  $\mathbf{x}_f$  = positions in the tangential direction with subscripts  $0$  and  $f$  representing starting position and finishing position.

$t$ ,  $t_0$  and  $t_f$  = time, starting time, and finishing time, respectively.

$V_t$  = desired velocity in tangential direction.

$t_b$  = blending time, determined by  $t_b = (\mathbf{x}_{t_0} - \mathbf{x}_f + V_t t_f) / V_t$

$\mathbf{a}_t$  = tangential acceleration, calculated by  $\mathbf{a}_t = V_t / t_b$ .

For the elliptical contour, we also desire constant tangential velocity in task space. This desired velocity is mapped into reference space to obtain the corresponding velocities as the elliptical arc is traversed. From this mapping, the desired position in reference space can be calculated.

Burrs on the plate edge were numerically generated from assumed size and shapes. We employed two types of simulated burrs shown in Figure 4.2: (a) randomly generated burrs with limited average height of burrs, and (b) burrs with regular variation in the height.

Size and shapes of burrs measured on aircraft engine parts were described by Kazerooni et al in [9]. In this investigation, the average height  $h_b$  of burrs varied from 0.25 to 0.75 mm (0.01 to 0.03 in), and the thickness  $t_c$  varied from 0.025 to 0.075 mm (0.001 to 0.003 in.). In our studies, the thickness of all burrs is taken to be the thickness of the plate  $b = 10$  mm. As shown in Figure 4.2, we used burrs with height  $h_b$  varying from 0 to 0.1 mm, with an average height  $h_a$  of 0.05 mm. The frequency of burrs  $f_b$  was chosen as two burrs per millimeter. While the burr frequency remained constant at this value, the burr height varied between 0 and 0.1 mm using a random function. Since burrs are usually sharp and small, we used a sinusoidal function to generate an individual burr, shown in Figure 4.2 c, with the magnitude generated by a uniform random number generator based on the linear congruential method [36]

$$y_{burr} = h_b(rand) \times \sin(2\pi f_b x_t) \quad 0 \leq x_t \leq 0.5mm$$

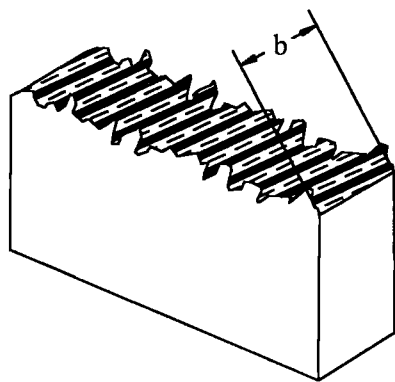
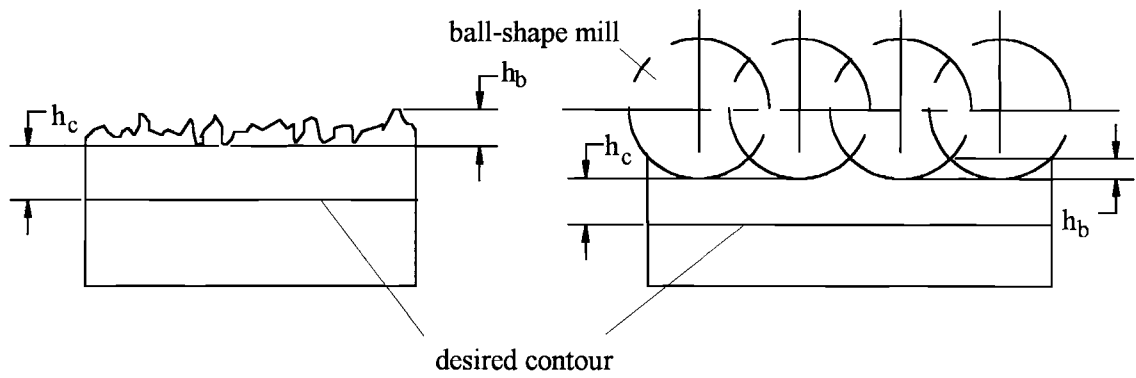
where

$y_{burr}$  is y-coordinate of burr edge.

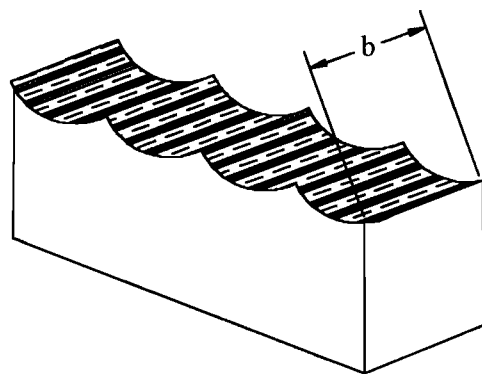
$h_b(rand)$  = burr height randomly generated, and held constant over each 0.5 mm interval.

To remove burrs completely and produce a good finishing surface, we also assumed a desired cut  $h_c$  of 0.5 mm below the lowest burr valley.

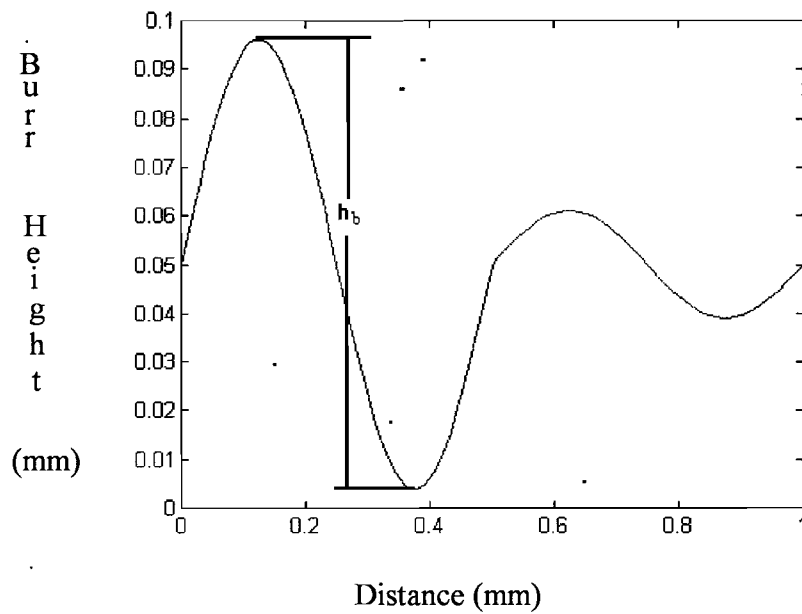
Another type of surface roughness occurs in the scallop produced by a ball-shaped end mill machining surfaces of complex parts, such as certain automobile parts [34]. This kind of surface exhibits regularity in the scallop pattern. The size and frequency of scallops are dependent on the tool dimension and the number of passes per unit width of



(a)



(b)



(c)

Figure 4.2 Schematic Diagram of Geometry of Burrs

surface. In our simulations, we generated an artificial "edge scallop" by assuming the diameter of the ball-shaped mills as 30 mm, with a 5 mm span of tool passes. Simple geometry shows that this results in a 0.25 mm scallop height  $h_b$ , with a frequency of 200 scallops per meter.

Using these artificial surfaces, we simulated robotic deburring and grinding using different controllers described in the following sections. The purposes of our simulations were to investigate (1) stable interaction between the end-effector and the workpiece, (2) achievable performance including position errors and contact forces, and (3) ability to accommodate to sudden large burrs. All the simulations were accomplished in MATLAB [36] using the automatic step size, Range-Kutta 45 algorithm. Except for Simulation 10, all simulations began and ended with the robot arms positioned with respect to the workpiece, as shown in Figure 4.3(a).

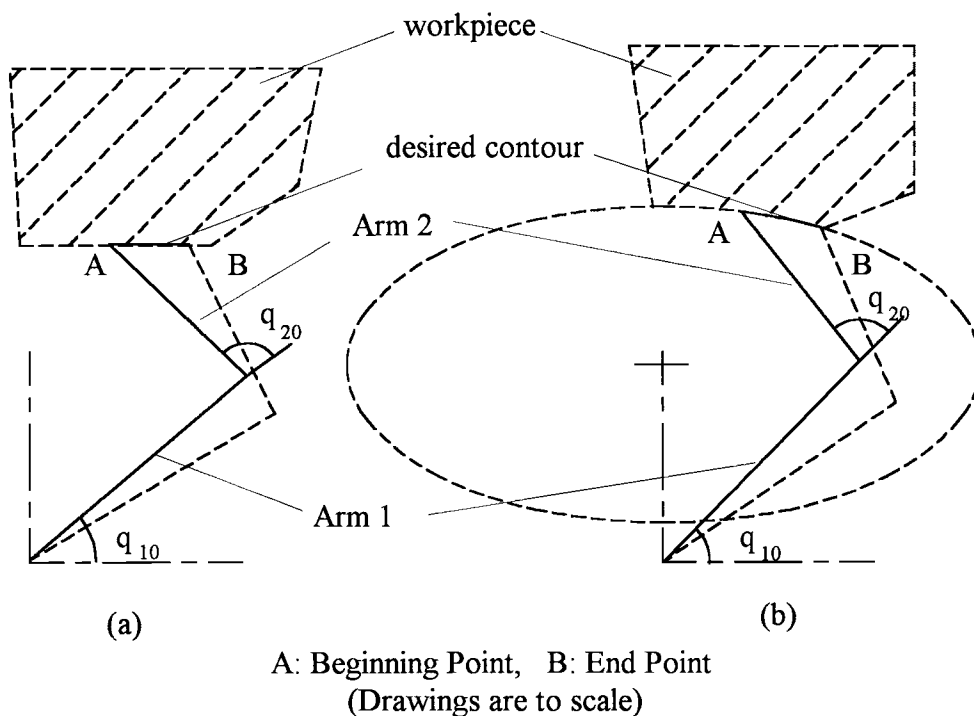


Figure 4.3 Schematic Diagram of Robot Configuration in Deburring

## Simulations for Impedance Control

We examine three simulations of an impedance controller to test the performance of impedance control for robotic deburring and grinding.

### Simulation 1 :

1) Simulation of deburring a straight edge starting from (0.1m, 0.4m) to (0.2m, 0.4m) in reference space. Total simulation time was set at 10 sec.

2) Employing impedance control law (3.6), the target impedance matrices were chosen as

$$M_d = [2.5 \text{ kg}, 0; 0, 2.5 \text{ kg}], B = [200 \text{ N.s/m}, 0; 0, 45 \text{ N.s/m}],$$

$$K = [4000 \text{ N/m}, 0; 0, 200 \text{ N/m}]$$

A large stiffness was selected for the normal direction while a small stiffness was selected for the tangential direction according to our earlier deburring analysis.

3) Desired workpiece contour: straight edge, parallel with x axis and located at  $y = 0.4$  m in reference space. Accordingly, the desired trajectories in the normal direction are:  $y = 0.4$  m,  $v_n = a_n = 0$ ;

4) Burr height and shape: randomly generated burrs with shaped as shown in Figure 4.2a; average burr height  $h_a = 0.05$  mm; desired cut  $h_c = 0.5$  mm; burr frequency  $f_b = 10000$  burrs/m.

5) Assume a constant tangential speed of  $V_t = 0.01$  m/s.

6) Simulation results showing position error and measured forces in the normal and the tangential directions are given in Figures 4.4 and 4.5.

### Simulation 2 :

In this simulation, we modified the target impedance relationship as in (3.14) by considering a desired contact force at desired position trajectories. For convenience, we repeat (3.14) here as

$$M_d \ddot{X} + B(\dot{X} - \dot{X}_d) + K(X - X_d) = -(F - F_d) \quad (4.2)$$

$$X = \begin{bmatrix} n \\ t \end{bmatrix}$$

where  $F_d$  is the desired force vector when the end-effector tracks the desired trajectories. The desired force  $F_d$  is the nominal grinding force at the desired depth of cut and the desired traverse velocity of the grinding wheel. To obtain the actual desired force  $F_d$ , we would need complete knowledge of the geometry of burrs, admittedly a difficult requirement in practice.

Except for the impedance matrices, we use the same simulation conditions as in Simulation 1. The nominal grinding force was chosen as  $F_d = [5.5; 5.5\mu]$  kg, an approximation calculated from (2.6) and (2.15) using  $V_t = 0.01$  m/s,  $V_n = 0$  m/s,  $d = 0.55$  mm, and  $D = 50.8$  mm. The grinding friction coefficient was selected as 0.7 [29]. After some initial trials, the target impedances were chosen as

$$M_d = [2.5 \ 0; 0 \ 2.5] \text{ kg}, \quad B = [200 \ 0; 0 \ 45] \text{ N.s/m}, \quad K = [4000 \ 0; 0 \ 200] \text{ N/m};$$

Simulation results are presented in Figures 4.6-4.7

### Simulation 3 :

We repeated Simulation 1, except that we changed the desired tangential velocity to that generated by LSPB described in (4.1), with  $V_t = 0.015$  m/s. The other parameters in (4.1) were  $t_0 = 0$ ;  $t_f = 10$  s;  $x_{t0} = 0.1$  m;  $x_{tf} = 0.2$  m, and the remaining parameters were calculated as indicated in (4.1). This simulation was run to evaluate the controlled performance, when the traverse desired velocity profile of the grinding wheel spindle was generated in a more realistic manner. Simulation results are shown in Figures 4.8-4.9.

## Results and Analysis for Impedance Control

The results of Simulation 1-3 given in Figures 4.4 - 4.9 indicate that impedance control was able to achieve stable performance as long as the impedance parameter

matrices are positive definite. Overshoot and oscillation exist in the transient response due to the nature of impedance control. Force feedback in the impedance control law acts as a high position feedback gain when the environment is very stiff. This large virtual gain results in underdamped response as shown in the Figures 4.4-4.9. However, if high impedance parameter values are selected, steady state is reached quickly.

In Simulation 1, we used the target impedance relationship (3.7) proposed by Hogan [18]. The results in Figures 4.4 and 4.5 illustrate large steady state position errors and small contact forces in the normal direction. Changing the impedance parameters seemed to change only the transient response, without significantly affecting steady state response. Notice that small forces in steady state indicate the grinding wheel barely removed materials, yet remained in contact with the workpiece. This is confirmed by observing position errors in the normal direction. These steady state position errors in the normal direction are approximately equal to the deviation of the average rough edge position from the desired normal position. In other words, the grinding wheel performed edge-following with little cutting. This is an expected consequence of impedance control, consistent with what others have reported [18, 19]. The results from Simulation 3 illustrate a similar edge-following phenomenon when the tangential velocity is generated by LSPB.

In Simulation 2, we modified the target impedance relationship by employing grinding force-motion relation (2.21) derived in Chapter II. This requires knowledge of the geometry of burrs, such that the desired depths of cut are known and Eq (2.6) and (2.15) may be used to obtain the nominal grinding forces, which is commanded in the target impedance relationship (4.2). Simulation results in Figures 4.6 and 4.7 show that steady state position errors in the normal direction were eliminated, though small steady state tangential position errors remained. Contact forces in steady state remained close to commanded forces, which were required to remove materials to reach the desired edge contour. These results indicate that if surface roughness geometry is measured or

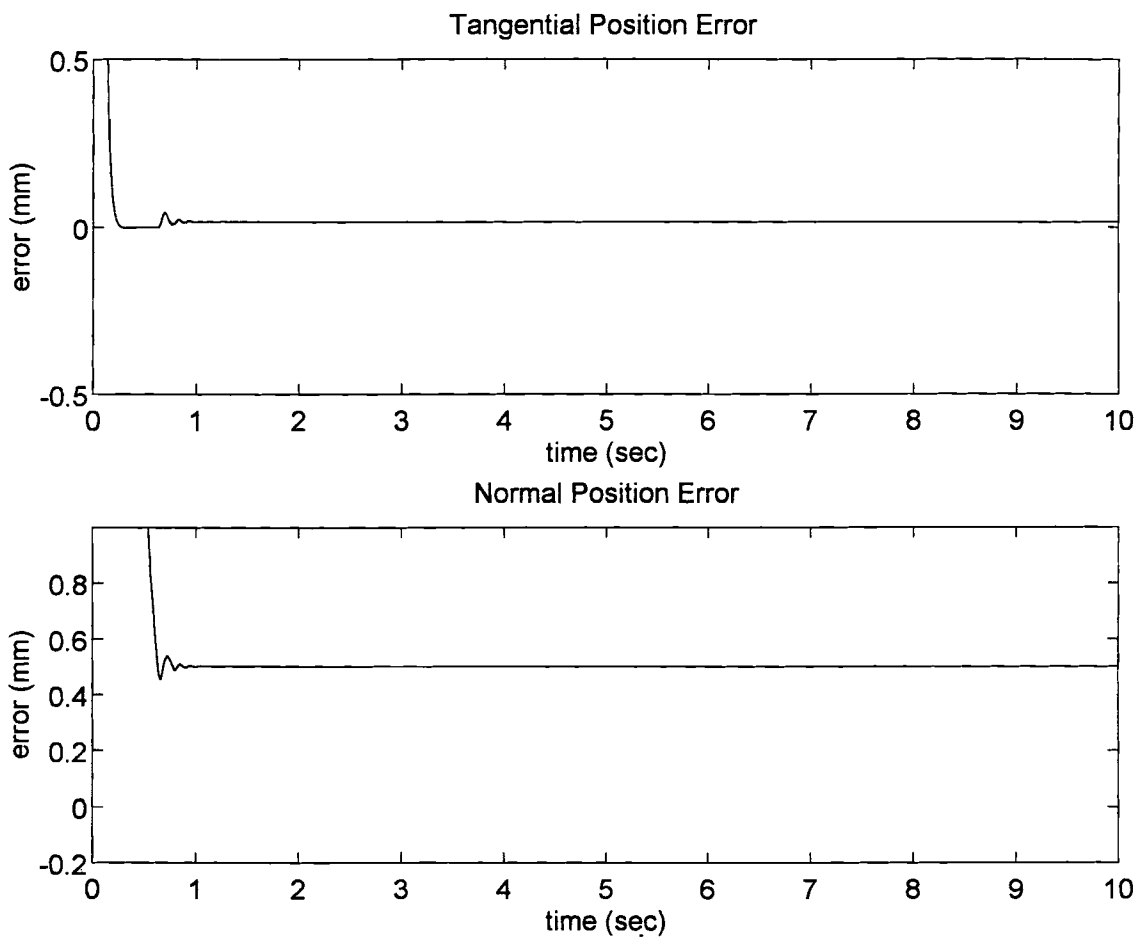


Figure 4.4 Results of Simulation 1 with Impedance Control: (a) Position Error



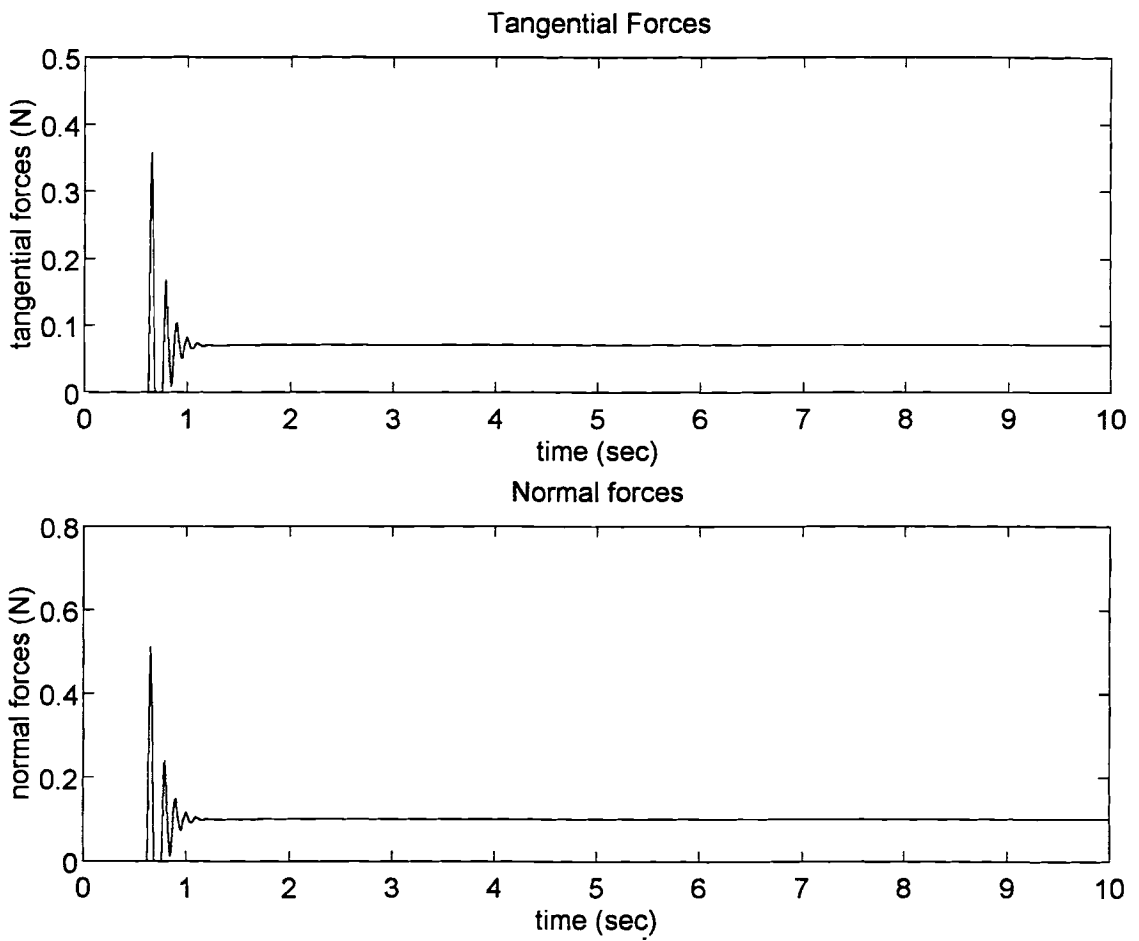


Figure 4.5 Results of Simulation 1 with Impedance Control: (b) Forces

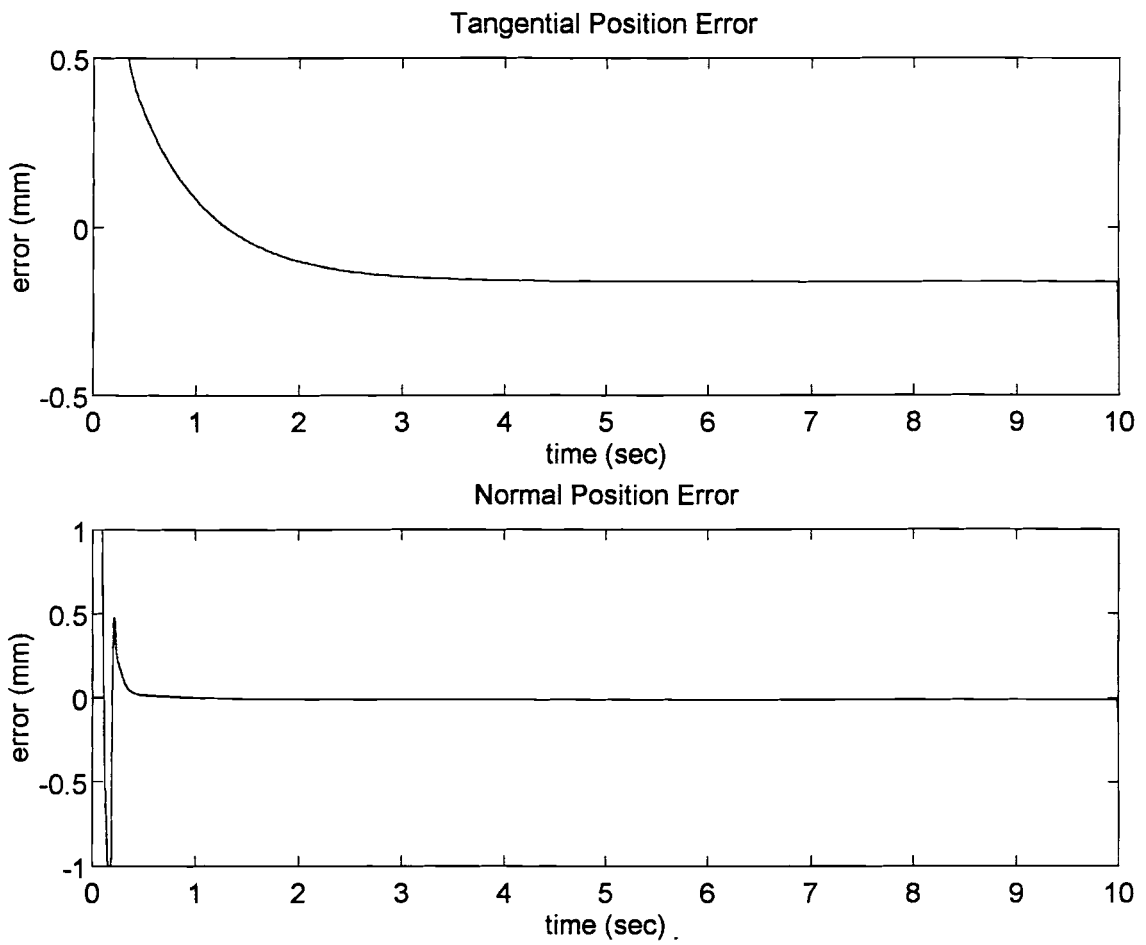


Figure 4.6 Results of Simulation 2 with Impedance Control: (a) Position Error

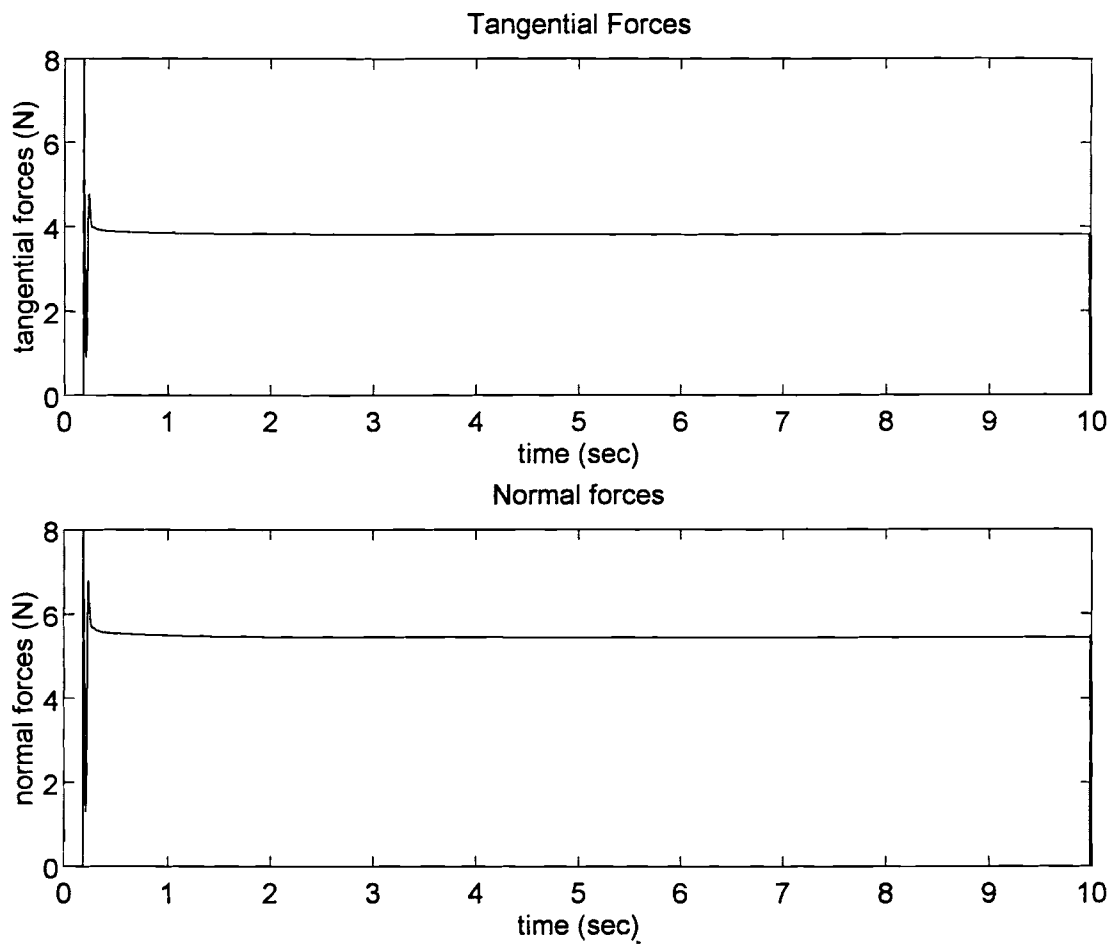


Figure 4.7 Results of Simulation 2 with Impedance Control: (b) Forces

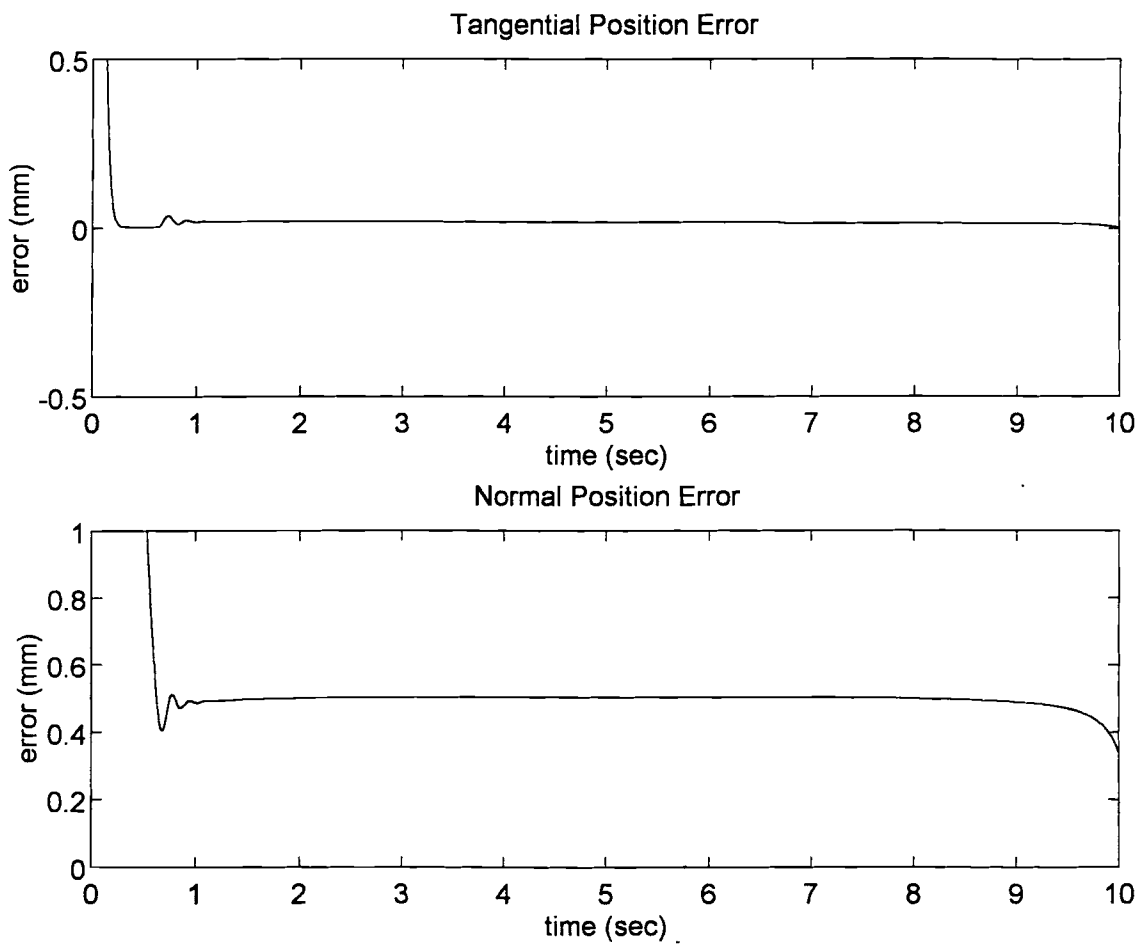


Figure 4.8 Results of Simulation 3 with Impedance Control: (a) Position Error

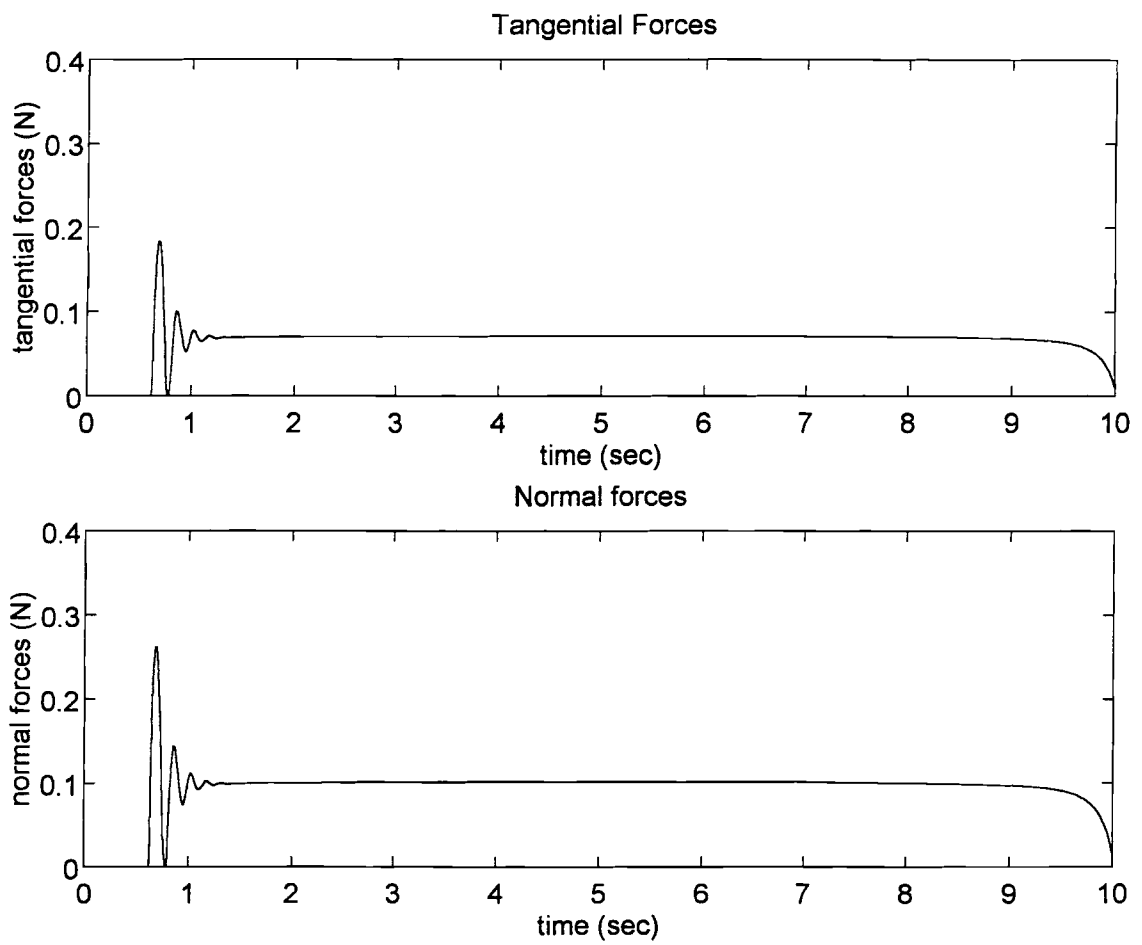


Figure 4.9 Results of Simulation 3 with Impedance Control: (b) Forces

predicted, then modified impedance control defined by (4.2) may achieve good performance for robotic deburring and grinding. Unfortunately, since burrs are highly irregular and unpredictable in practical deburring, it is likely very difficult to calculate and command desired grinding forces accurately. In such cases, impedance control could degrade or become unstable.

Based on these simulation results, we conclude that an impedance controller may be suitable for edge following or other tasks requiring a small amount of contact force between the end effector and environment. If large interaction forces are expected between the end-effector and its environment, a specified constant desired force should be commanded by employing (4.2). For deburring and grinding, with large and varying contact forces, impedance control is impractical for achieving desired performance.

### Simulations for Hybrid Impedance Control

#### Simulation 4 :

The hybrid impedance control law of (3.4) and (3.18), with position control in the tangential direction and force control in the normal direction, was used in this simulation. After some initial trials, impedance parameters were selected as:  $m_t = 10$  kg,  $b_t = 200$  N-s/m,  $k_t = 1000$  N/m;  $m_n = 100$  kg,  $b_n = 100$  N-s/m. The target force in the normal direction was set at  $f_n = 4$  kg. Other conditions were the same as those in Simulation 1. Results are presented in Figures 4.10 and 4.11.

### Results and Analysis for Hybrid Impedance Control

Various trial simulations, in addition to that in Simulation 4, were conducted to investigate hybrid impedance control for deburring and grinding. We studied controlled performances of the manipulator under different elements in the gain matrices ranging

from as small as 2 to large values in the thousands. Selected results are given in Figures 4.10 and 4.11. As can be seen, oscillations of both positions and velocities, and thus contact forces, occurred during the interaction between the grinding wheel and workpiece. We found that large values of  $m_n$ ,  $b_t$ , and  $k_t$  improved motion tracking in the tangential direction, while small values caused fluctuations in the tangential velocity. For force control in the normal direction, changing  $b_n$  affected impact of the end effector at the beginning of contact with the workpiece due to its effect on velocities approaching the workpiece. This may be better understood from the following analysis. Since the contact force is zero before contact, from (3.16) we obtain

$$m_n \ddot{n} + b_n \dot{n} = F_{dn} \quad (4.3)$$

The solution of (4.3) for constant  $F_{dn}$  and zero initial velocity is

$$\dot{n} = \frac{F_{dn}}{b_n} (1 - e^{-b_n t / m_n}) \quad (4.4)$$

Since  $m_n$  and  $b_n$  are positive, we observe that

$$\dot{n} < \left| \frac{F_{dn}}{b_n} \right|$$

That is, the normal velocity approaching the workpiece is bounded by zero and  $|F_{dn}/b_n|$ , such that  $b_n$  determines the upper limit. Thus, large  $b_n$  results in low impact of the end-effector as it contacts the workpiece.

The parameter  $m_n$  is critical in obtaining stable control because it essentially acts as a force feedback gain. Small values for  $m_n$  result in high oscillations, which lead to unstable contact. However, large values of  $m_n$  will slow and degrade motion tracking in the normal direction. Our simulation showed that, if  $m_n = 1600$  kg,  $b_n = 1600$  N-s/m, the manipulator requires the entire simulation time (10 sec) to approach and contact the workpiece.

Through simulations, we concluded that hybrid impedance control is not appropriate for deburring and grinding, although previous investigators [24] reported that

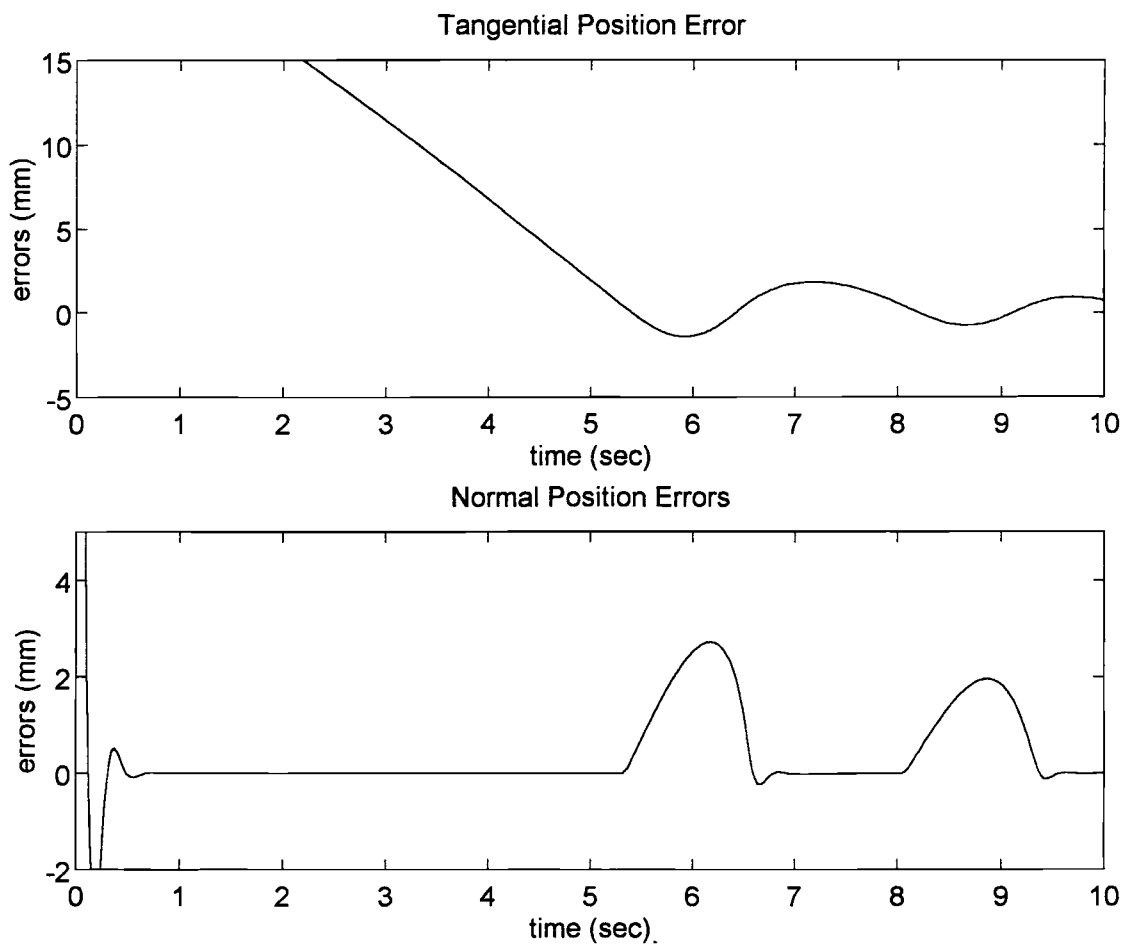


Figure 4.10 Results of Simulation 4 with Hybrid Impedance Control: (a) Position Error



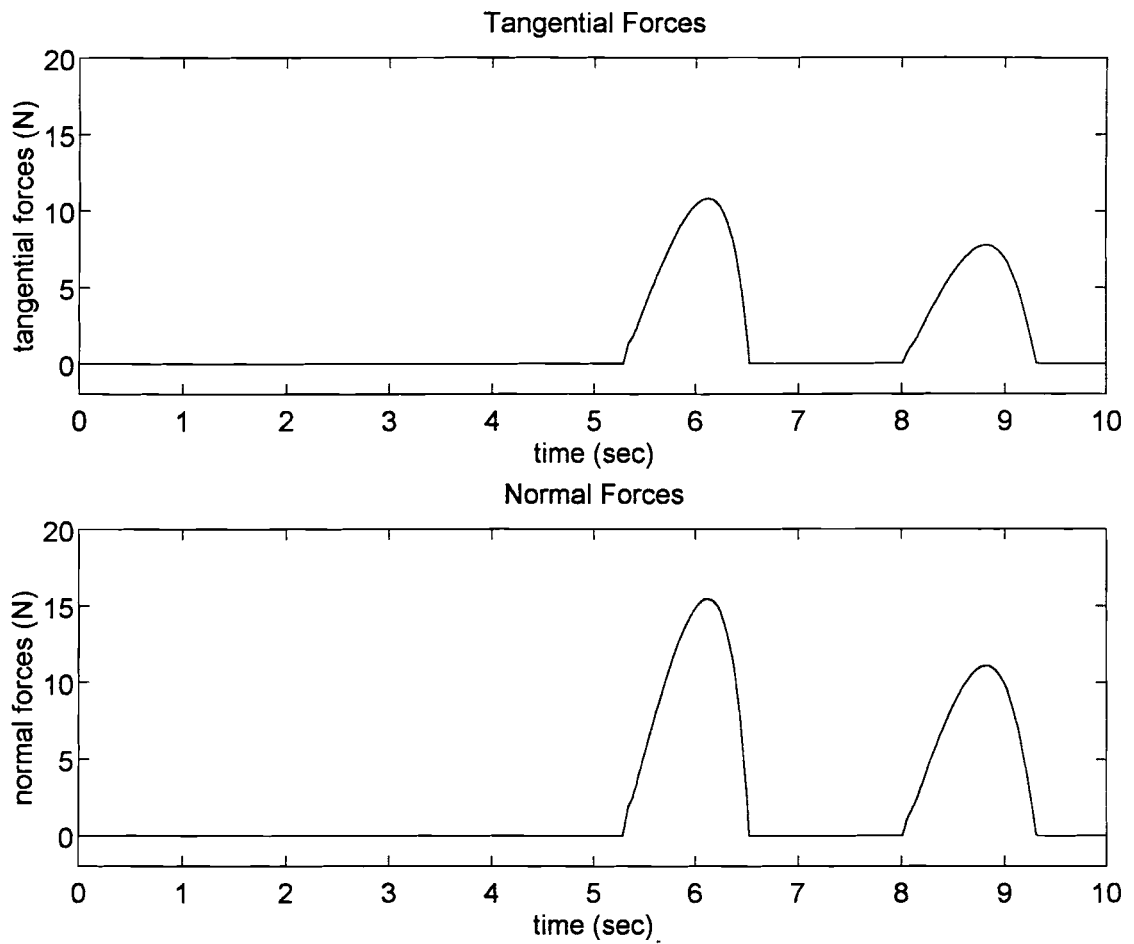


Figure 4.11 Results of Simulation 4 with Hybrid Impedance Control: (b) Forces

hybrid impedance control was successfully employed for force control in simple assembly tasks. In such tasks no friction force existed in the tangential direction, and a linear relationship between motion and force in the normal direction was assumed. In other words, dynamics and control in two orthogonal directions were decoupled. In deburring and grinding forces, the coupling of cutting and normal forces degrades the performance of the hybrid impedance controller. Because the controller acts so as to achieve the desired forces, dynamic effects of impacts cause fluctuations in position, or depth of cut, in the normal direction due to the absence of position control in this direction. Oscillations in depth of cut, through the grinding force relationship, will cause fluctuations in the velocity in the tangential direction. In turn, motion oscillations in both directions lead to large force fluctuations. These phenomena appear throughout the entire simulation run, as shown in Figures 4.10 and 4.11.

### Simulations for Simultaneous Position/Force Control

#### Simulation 5 :

- 1) Simulation of deburring a straight edge from (0.1m, 0.4m) to (0.2m, 0.4m) in reference space. Total simulation time was 10 sec.
- 2) Employ the simultaneous position/force controller (3.4), (3.19), and (3.20). In this simulation, we investigated the controller for cases where high position accuracy is required and the robot and tooling are sufficiently strong to accommodate the large grinding forces generated. Position control is more important here than force control.
- 3) Desired workpiece contour: straight horizontal edge, located at  $y = 0.4$  m in reference space. Accordingly, the desired trajectories in normal direction are:  $y = 0.4$  m,  $v_n = a_n = 0$ ;
- 4) Burr height and shape: randomly generated burrs as in Simulation 1, shown in Figure 4.2a; average burr height  $h_a = 0.05$  mm; desired cut  $h_c = 0.5$  mm, burr frequency  $f_b = 2000$  burrs/m.

5) Assume a constant desired tangential speed of  $V_t = 0.01$  m/s.

6) After some initial trials, gain values were selected as:

$$K_p = [400, 0; 0, 400] \text{ 1/s}^2, K_d = [40, 0; 0, 40] \text{ 1/s}, K_i = [0, 0; 0, 0] \text{ 1/s}^3,$$

$$K_f = [0, 0] \text{ m/(s}^2\text{.N)}, K_{fi} = [0, 0] \text{ m/(s}^3\text{.N)}.$$

Simulation results are presented in Figures 4.13 and 4.14.

Simulation 6 :

1) Simulation of deburring a straight edge starting from (0.1m, 0.4m) to (0.2m, 0.4m) in reference space. Total simulation time was 10 sec.

2) Employ the simultaneous position/force controller (3.4), (3.19), and (3.20). In this simulation, we investigated force control ability with the simultaneous position/force controller. Contact forces are controlled to track desired forces, while positions are allowed to deviated from desired trajectories. Force control is more important here than position control.

3) Desired workpiece contour: straight edge, located at  $y = 0.4$  m in reference space. Accordingly, the desired trajectories in the normal direction are:  $y = 0.4$  m,  $v_n = a_n = 0$ .

4) Assume a constant desired tangential speed of  $V_t = 0.01$  m/s.

5) Burr height and shape: randomly generated burrs as in Simulation 1 and shown in Figure 4.2a; average burr height  $h_a = 0.05$  mm, and burr frequency  $f_b = 2000$  burrs/m. However, in this simulation we desired a deeper cut, with  $h_c = 1.5$  mm, which would require a normal force of about 15.5 kg, calculated from (2.17). However, we assume that the maximum allowable normal force is 12 kg, such that we must control normal force to remain below 12 kg.

6) After initial trials, gain matrix elements were selected as

$$K_p = [45, 0; 0, 45] \text{ 1/s}^2, K_d = [6\sqrt{5}, 0; 0, 6\sqrt{5}] \text{ 1/s}, K_i = [0, 0; 0, 0.5] \text{ 1/s}^3,$$

$$K_f = [0.05, 0] \text{ m/(s}^2\text{.N)}, K_{fi} = [0.0000595, 0] \text{ m/(s}^3\text{.N)}.$$

Simulation results are presented in Figures 4.15 and 4.16.

### Simulation 7 :

If an abrupt large burr is encountered during the grinding process, normal forces exceeding the allowed maximum force may occur. The controller should be able to contain the normal force below the allowed limits in such a situation. In this simulation, we investigated the controlled performance of the manipulator when a large burr was suddenly encountered.

- 1) Simulation of deburring a straight edge starting from (0.1m, 0.4m) to (0.2m, 0.4m) in reference space. Total simulation time was 10 sec.
- 2) Employ the simultaneous position/force controller (3.4), (3.19), and (3.20), with the addition that the elements in the gain matrices were changed from position-dominated control to force-oriented control when large burrs were encountered.
- 3) Desired workpiece contour: straight edge, located at  $y = 0.4$  m in reference space. Accordingly, the desired trajectories in normal direction are:  $y = 0.4$  m,  $v_n = a_n = 0$ ;
- 4) Assume a constant desired tangential speed of  $V_t = 0.01$  m/s.
- 5) Burr height and shape: randomly generated burrs as in Simulation 1 and shown in Figure 4.2a. At the beginning and end portions of the workpiece edge, burrs are small with average burr height  $h_a = 0.05$  mm, and burr frequency  $f_b = 2000$  burrs/m. However, we add a large "rectangular" burr on the edge in the region in reference space  $0.14 \text{ m} \leq x \leq 0.17 \text{ m}$ , with burr height  $h_b$  ranging from 1 mm to 1.1 mm, with an average height  $h_a = 1.05$  mm, and burr frequency  $f_b = 2000$  burrs/m. The same random burr height generator was used as in Simulation 1. The rough edge is depicted in Figure 4.12a. We desired to remove burrs while grinding deep into the workpiece, with  $h_c = 0.5$  mm to produce a finished contour. By using Eq. (2.17), it can be shown this requires a normal force of about 5.5 kg for removing small burrs, while for the large burrs, expected normal forces may reach 15.5 kg. Assuming that our system allows a maximum force of only 10 kg, we desired to control normal force at levels below this value.

6) We used a position-dominated controller for deburring the small burrs because small normal forces were required in such cases, and position accuracy was deemed predominant. If the measured normal force approached the maximum allowed force, a force-dominated controller was applied. The switch of controllers was accomplished by changing gain values. By trial and error, gain values for the position-dominated controller were selected as

$$K_p = [400, 0; 0, 400] \text{ 1/s}^2, K_d = [40, 0; 0, 40] \text{ 1/s}, K_i = [0, 0; 0, 0] \text{ 1/s}^3,$$

$$K_f = [0, 0] \text{ m/(s}^2\text{.N)}, K_{fi} = [0, 0] \text{ m/(s}^3\text{.N)}.$$

For the force-dominated controller, gain values were selected as

$$K_p = [10, 0; 0, 10] \text{ 1/s}^2, K_d = [2\sqrt{10}, 0; 0, 2\sqrt{10}] \text{ 1/s}, K_i = [0, 0; 0, 0.005] \text{ 1/s}^3,$$

$$K_f = [0.005, 0] \text{ m/(s}^2\text{.N)}, K_{fi} = [0.0000598, 0] \text{ m/(s}^3\text{.N)}.$$

Simulation results are presented in Figures 4.17 and 4.18.

#### Simulation 8 :

In Simulation 7, we generated a large rectangular-shaped burr with a rough top edge. This represents a very abrupt, and perhaps unrealistic burr geometry. Considering the comparatively large diameter of the grinding wheel, actual large burr height changes would be approached more gradually. To simulate a more gradual change, we generated a large trapezoidal-shaped burr in this simulation, as illustrated in Figure 4.12b. The trapezoidal burr lies in the interval  $0.13 \text{ m} \leq x \leq 0.19 \text{ m}$ . The base shape of the trapezoidal burr and its dimensions are given in Figure 4.12c. On this base shape, we superimposed a randomly generated signal, similar to that in Simulation 1, yielding height  $h_b$  varying from 1.0 mm to 1.1 mm and average height  $h_a = 1.05 \text{ mm}$ . Gains were the same as in Simulation 7, and simulation results are presented in Figures 4.19 and 4.20.

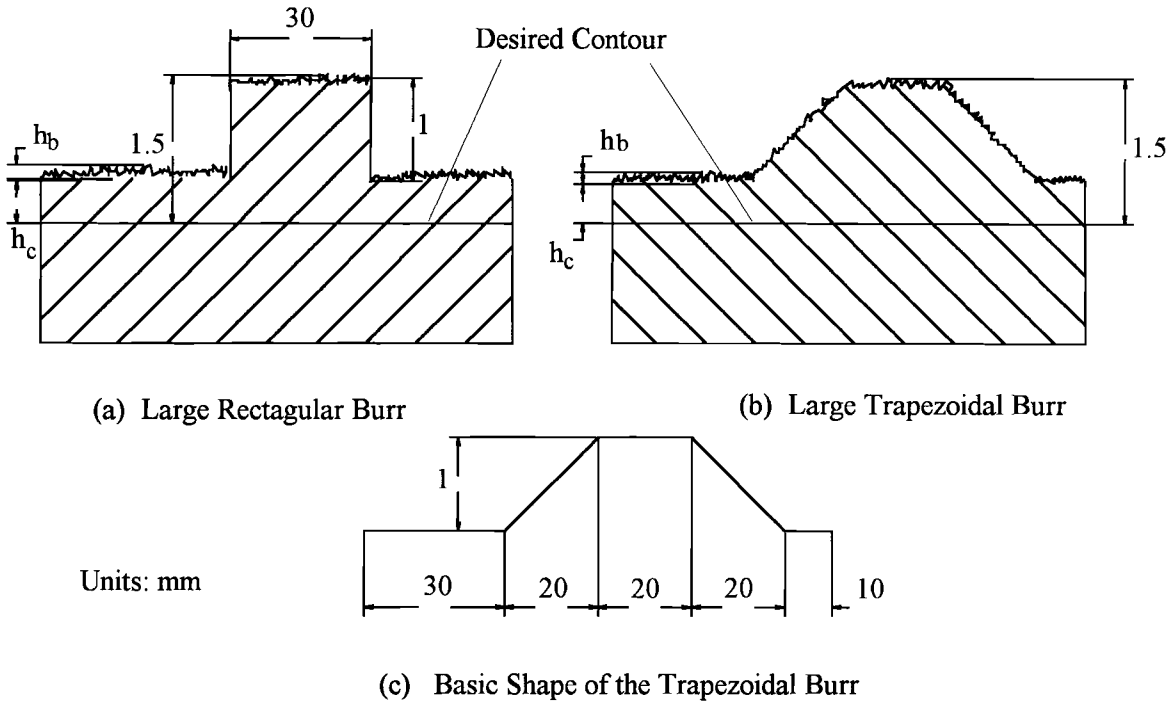


Figure 4.12 Schematic of Large Burrs

Simulation 9 :

- 1) Simulation of deburring a straight edge from (0.1m, 0.4m) to (0.2m, 0.4m) in reference space. Total simulation time was 10 sec.
- 2) Employ the simultaneous position/force controller (3.4), (3.19), and (3.20).
- 3) Desired workpiece contour: straight edge, located at  $y = 0.4$  m in reference space.  
Accordingly, the desired trajectories in normal direction are:  $y = 0.4$  m,  $v_n = a_n = 0$ ;
- 4) Burr height and shape: scallop-type of burr with shape shown in Figure 4.2b, with a 0.25 mm scallop height and a frequency of 200 scallops per meter.
- 5) Assume a constant desired tangential speed of  $V_t = 0.01$  m/s.
- 6) Gain matrix elements were the same as in Simulation 5, namely

$$K_p = [400, 0; 0, 400] \text{ 1/s}^2, K_d = [40, 0; 0, 40] \text{ 1/s}, K_i = [0, 0; 0, 0] \text{ 1/s}^3,$$

$$K_f = [0, 0] \text{ m/(s}^2\text{.N)}, K_{fi} = [0, 0] \text{ m/(s}^3\text{.N)}.$$

Simulation results are presented in Figures 4.21 and 4.22.

### Simulation 10 :

We evaluated the simultaneous position/force controller for our manipulator deburring a more complex contour, namely that of a workpiece having an interior elliptical contour.

1) Simulation of deburring an elliptical edge in reference space region  $0.1 \text{ m} \leq x \leq 0.2 \text{ m}$ . Total simulation time was 10 sec.

2) Employ the simultaneous position/force controller (3.4), (3.19), and (3.20).

3) Desired workpiece contour: a section of an elliptical curve described by (3.25) with parameters:

$$a = 0.4 \text{ m}, b = 0.2 \text{ m}; g = 0 \text{ m}, h = 0.25 \text{ m}; 0.1 \text{ m} \leq x \leq 0.2 \text{ m}.$$

The total perimeter of this ellipse is 1.938 m, such that our simulation contour covers only approximately 6.5% of this perimeter. Figure 4.3b shows the workpiece contour with the robot arm positions at the beginning and end of the simulation.

4) Burr height and shape: randomly generated burrs as in Simulation 1, with shape shown in Figure 4.2a. The maximum height of burrs is 0.04 mm and minimum height is zero, with average burr height measured in the normal direction was  $h_a = 0.02 \text{ mm}$ . To remove the burrs and grind deep into the workpiece, we used  $h_c = 0.5 \text{ mm}$ ,

5) Because the desired contour section of the workpiece is approximately flat in the  $x$  direction, we selected position and velocity trajectories in reference space, and then mapped them into task space. Velocity along the  $x$  axis in reference space is chosen constant at  $V_x = 0.01 \text{ m/s}$ . Desired position and velocity in the  $y$  direction is derived from the kinematic constraint equation (2.35). If the contour were not approximately flat, the desired trajectories should be commanded in task space directly, such that spurious commands caused by mapping between the different spaces will not occur.

6) Gain matrices were chosen by trial and error as

$$K_p = [900, 0; 0, 900] \text{ 1/s}^2, K_d = [60, 0; 0, 60] \text{ 1/s}, K_i = [0.1, 0; 0, 0.1] \text{ 1/s}^3, \\ K_f = [0, 0] \text{ m/(s}^2\cdot\text{N)}, K_{fi} = [0, 0] \text{ m/(s}^3\cdot\text{N)}.$$

Simulation results are presented in Figures 4.23 and 4.24.

### Results and Analysis for Simultaneous Position/Force Control

We ran Simulation 5 and 6 under the same conditions as Simulations 1 and 2 for impedance control in order to compare results from the two controllers. If the gains are properly selected, simultaneous position/force control is able to achieve good transient and steady state response. The oscillations in transient response and non-zero steady state error observed with impedance control were eliminated by this new control. The results of these simulations showed that simultaneous position/force control is superior to impedance control.

Figures 4.13 and 4.14 illustrate a very accurate position control was achieved in Simulation 5 by this control approach. In cases where a strong robot is employed to remove a small amount of material, as recommended in [35], an accurate finished contour can be obtained. Results from simulation 5 indicate that PD control may be able to achieve good performance, provided accurate and fast sensors can feedback measured signals to cancel nonlinear effects in the system dynamics, and efficient real-time computation is available to perform the model-based calculations. The integral portion of position control is required only when force control is simultaneously employed, or to eliminate steady state errors caused by dynamic modeling and nonlinear compensation errors.

Simultaneous position/force control is also able to achieve good force control, as shown by the results of Simulation 6 in Figures 4.15 and 4.16. In force control, the integral gain of force control portion played a critical role in achieving good force performance. Large values of force integral gain led to instability and loss of contact. Thus very small gains were used in this simulation. As seen in Fig. 4.16, contact forces were effectively controlled to track the desired forces. However, Fig. 4.15 shows that



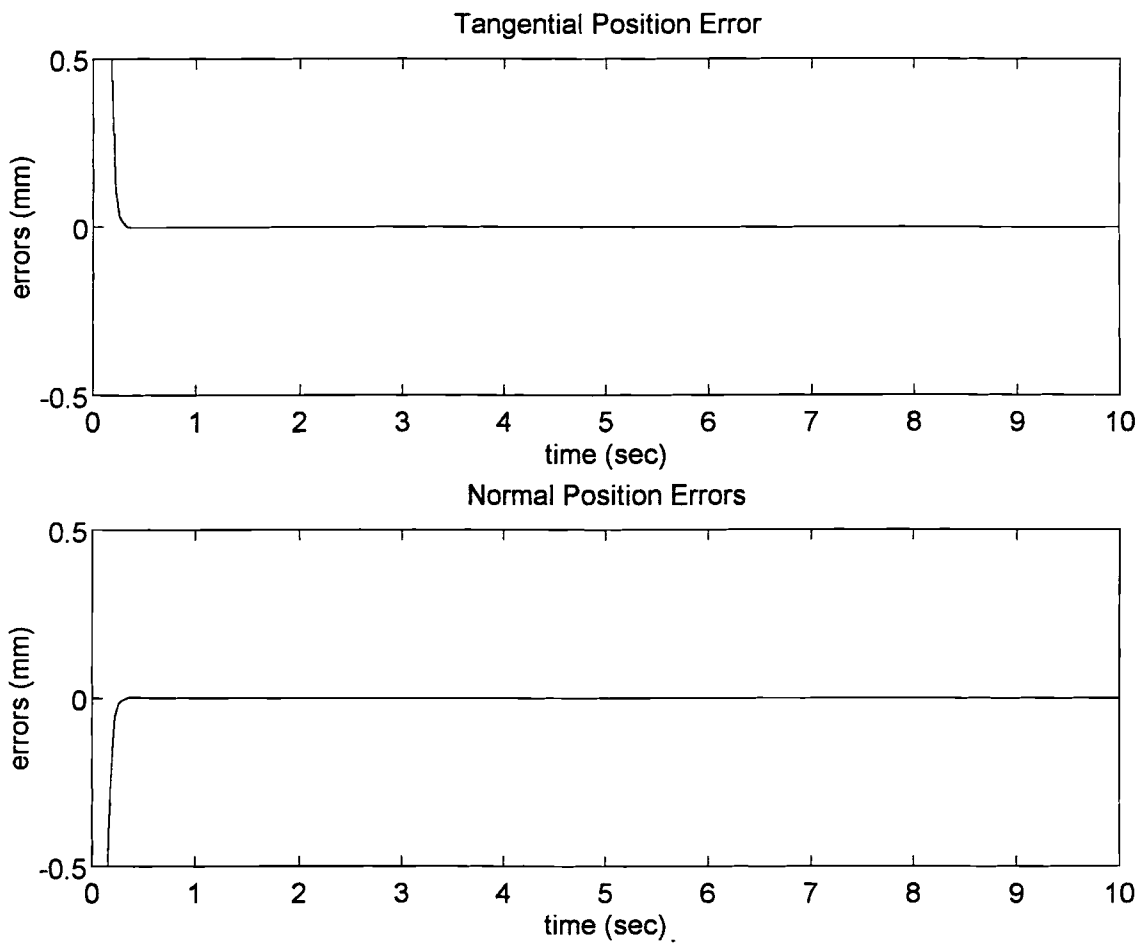


Figure 4.13 Results of Simulation 5 with Simultaneous Position/Force Control:  
(a) Position Error

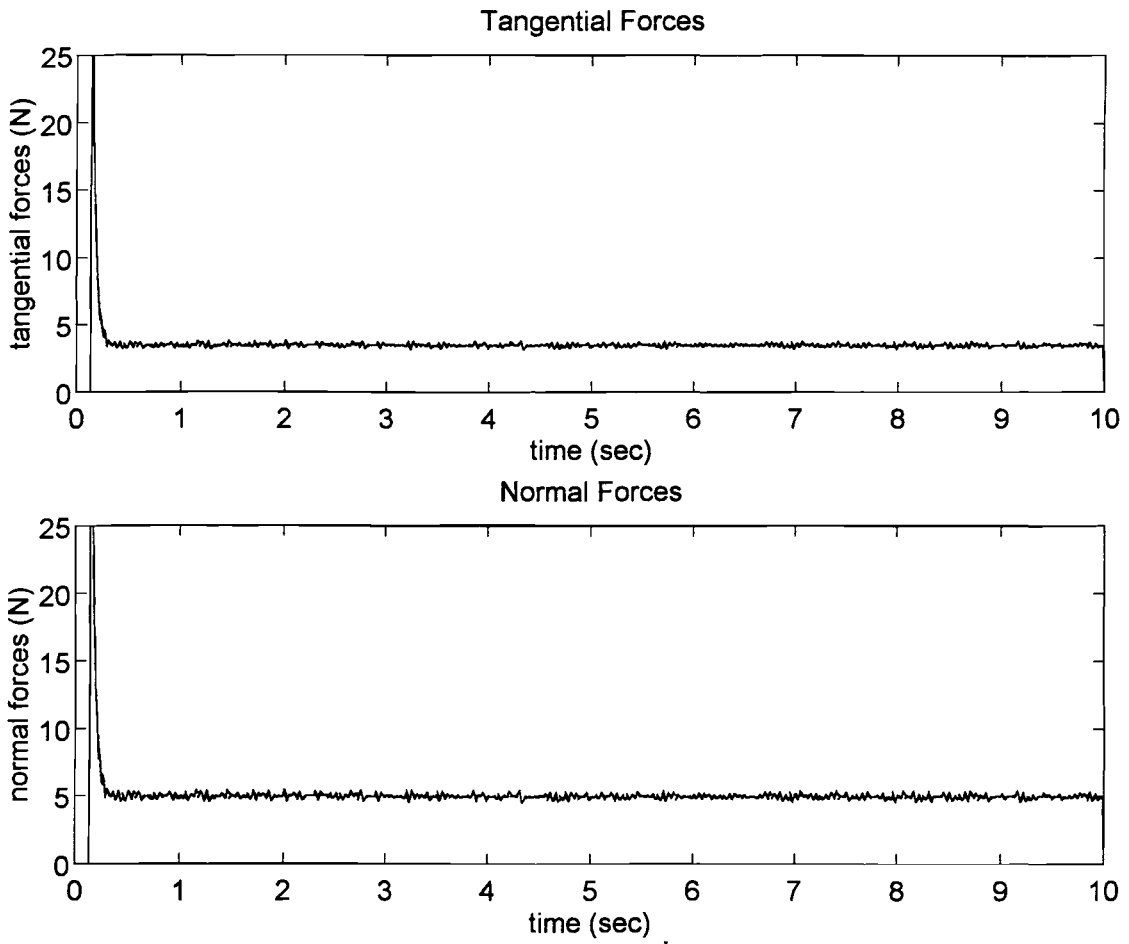


Figure 4.14 Results of Simulation 5 with Simultaneous Position/Force Control:  
(b) Forces

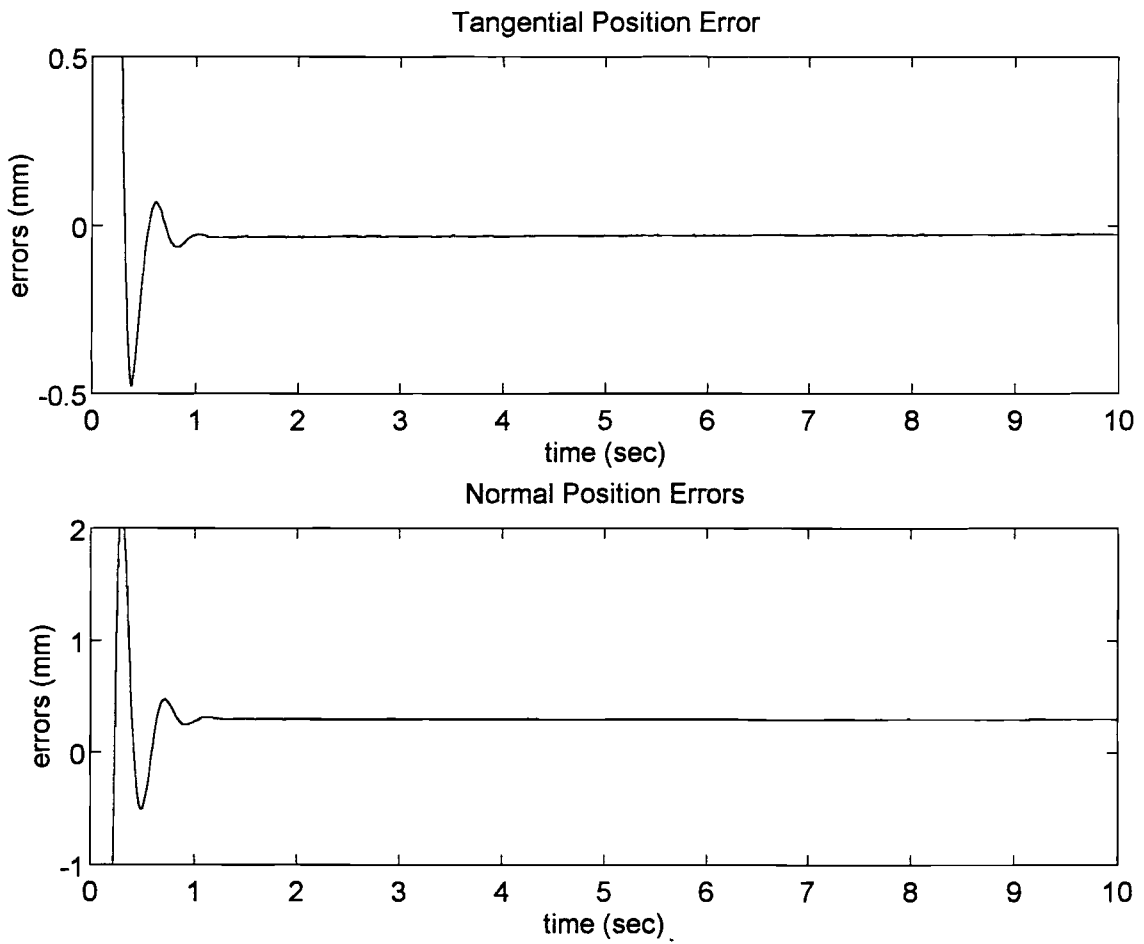


Figure 4.15 Results of Simulation 6 with Simultaneous Position/Force Control:  
(a) Position Error

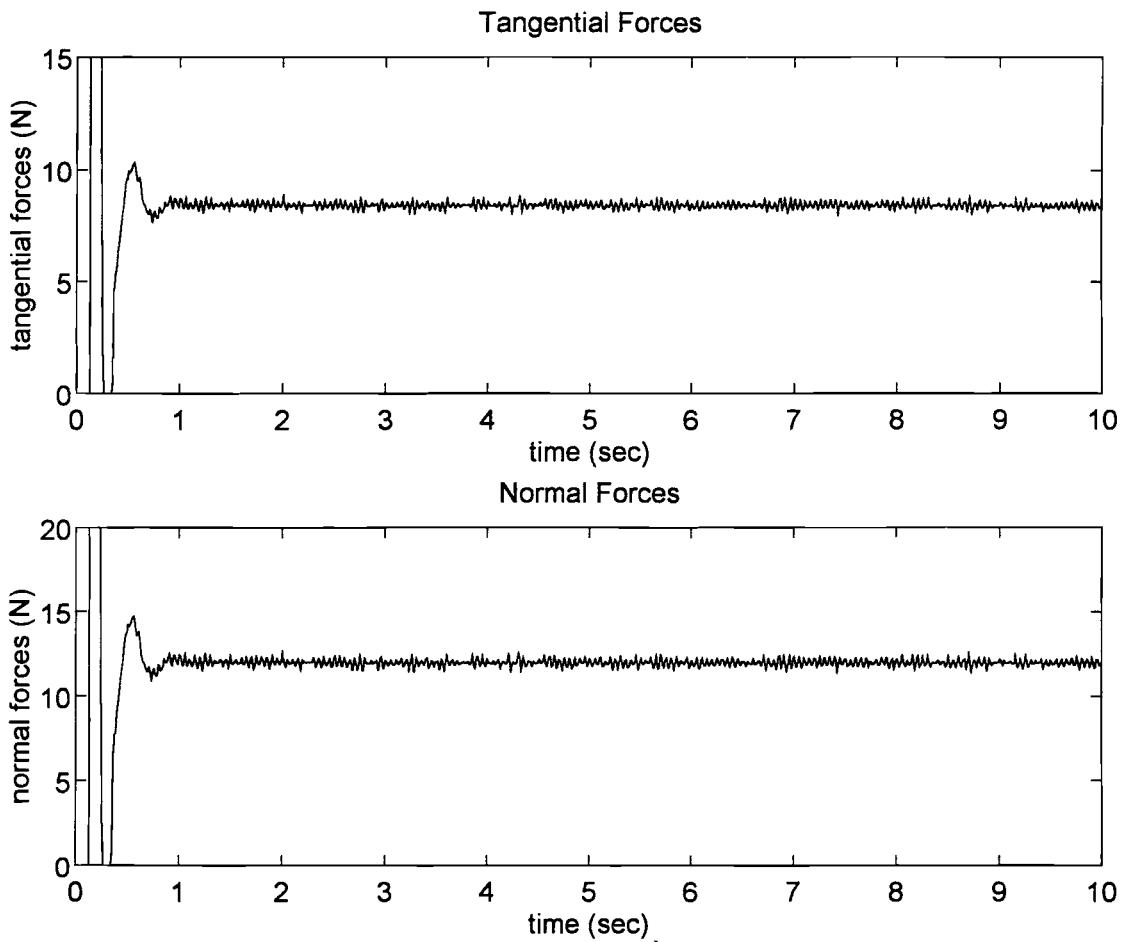


Figure 4.16 Results of Simulation 6 with Simultaneous Position/Force Control:  
(b) Forces

position errors were significant. This is due to physical impossibilities in robot structure, rather than the control algorithm, because it is impossible for the robot to simultaneously have large compliance for good force control and large stiffness for good position control. In contrast, we found earlier that impedance control could not achieve good force control.

One of advantages of simultaneous position/force control is that the control law allows the designer, or an automatic gain changer, to switch the control from position-control-dominated to force-control-dominated by simply changing the gain values without any change of control structure. As discussed in Chapter II, position accuracies are more important when deburring small burrs as long as contact forces are below the allowed force limits. Once large burrs are encountered, the normal force must be maintained below forces limits, such that force control now becomes more important than position control. Such situations require that the controller adapt during deburring. In Simulation 7, we employed a simultaneous position/force controller to deburr a complex rough edge with a mix of small and large burrs. The results showed simultaneous position/force control was able to achieve good manipulator performance and finishing results for this situation. Figures 4.17 and 4.18 show position errors were very small during the initial 4 seconds of deburring with the normal force below the allowed limit of 10 kg. Once the large burr was encountered, normal forces initially exceeded this limit, but were then effectively held below this limit, although results also show that there were jumps at the beginning and end of the large burr due to the switch of gain values and sudden change of burr size. To examine the effects of more gradual changes in bur sizes, we generated a large trapezoidal-shaped burr for Simulation 8. The results in Figures 4.19 and 4.20 indicate the jump in position error and force at the beginning of the large burr was not significantly affected, but the jump at the end was significantly decreased. We expect such large transients in force may be further decreased in practical deburring because the size of the grinding wheel would likely moderate some of the sudden plunging into a large burr. We observe that obtaining performance this good would be impossible for an impedance

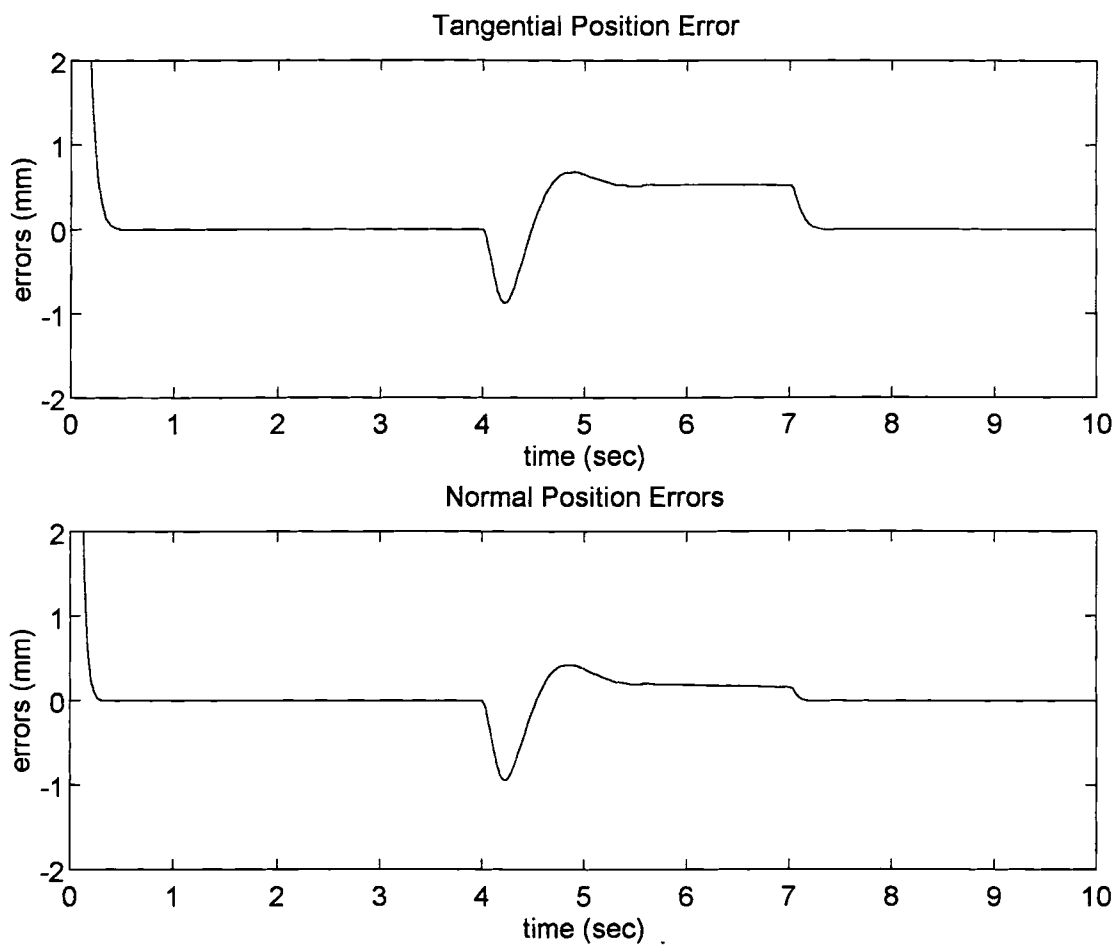


Figure 4.17 Results of Simulation 7 with Simultaneous Position/Force Control:  
 (a) Position Error

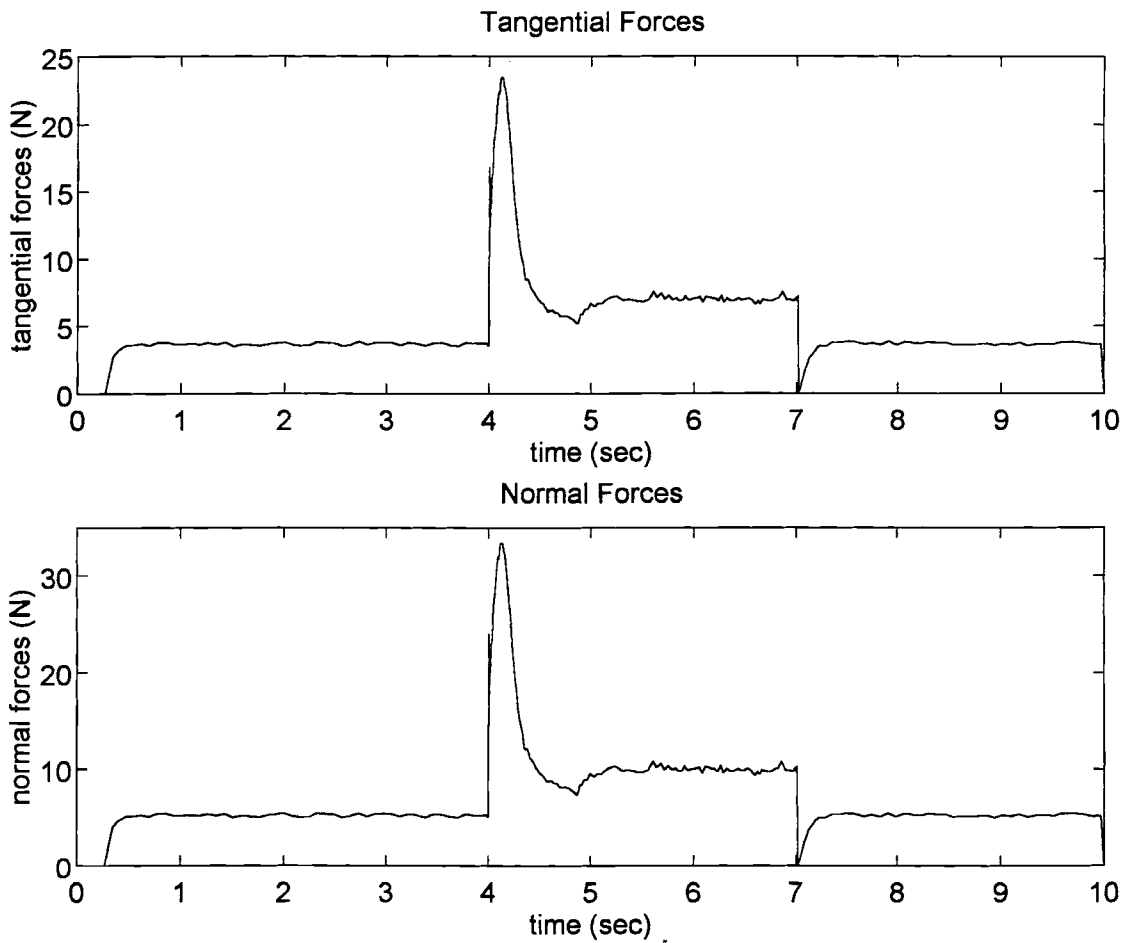


Figure 4.18 Results of Simulation 7 with Simultaneous Position/Force Control:  
(b) Forces

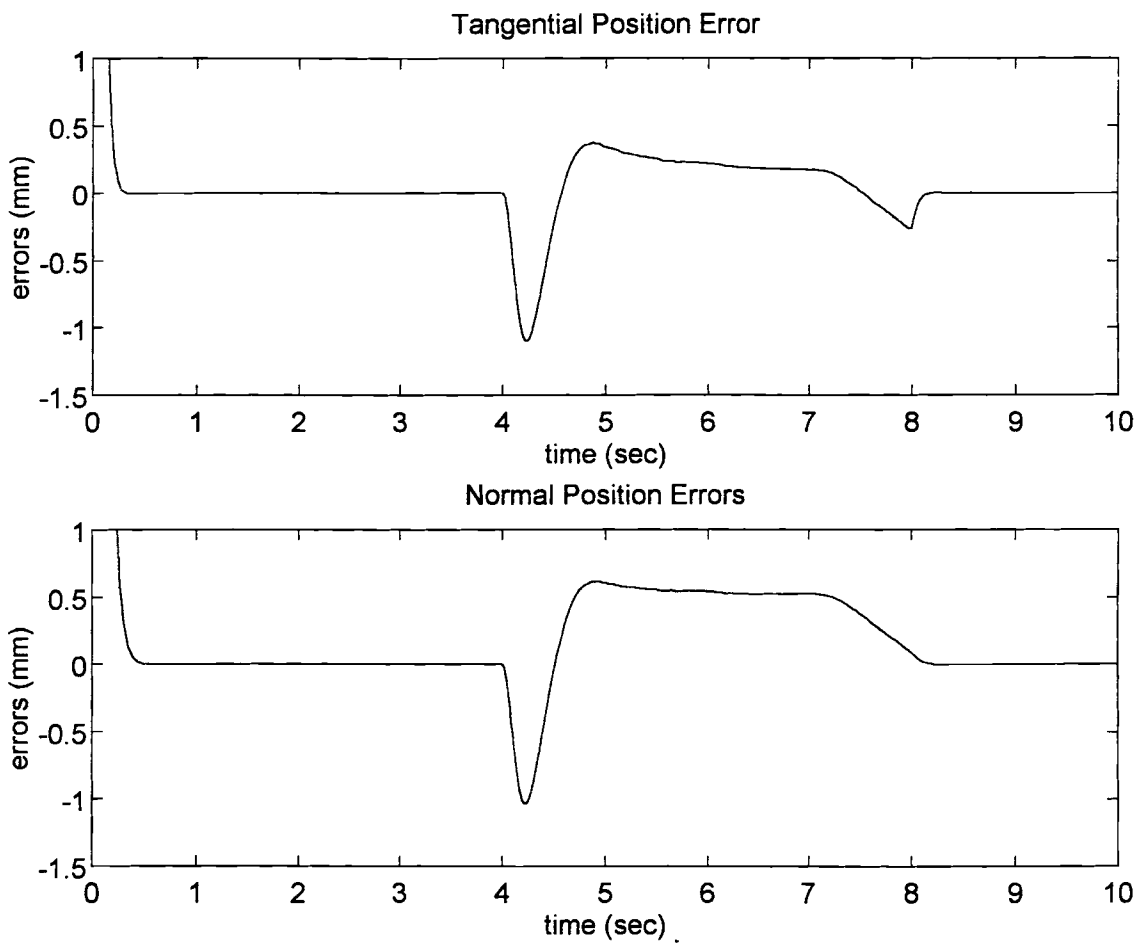


Figure 4.19 Results of Simulation 8 with Simultaneous Position/Force Control:  
 (a) Position Error



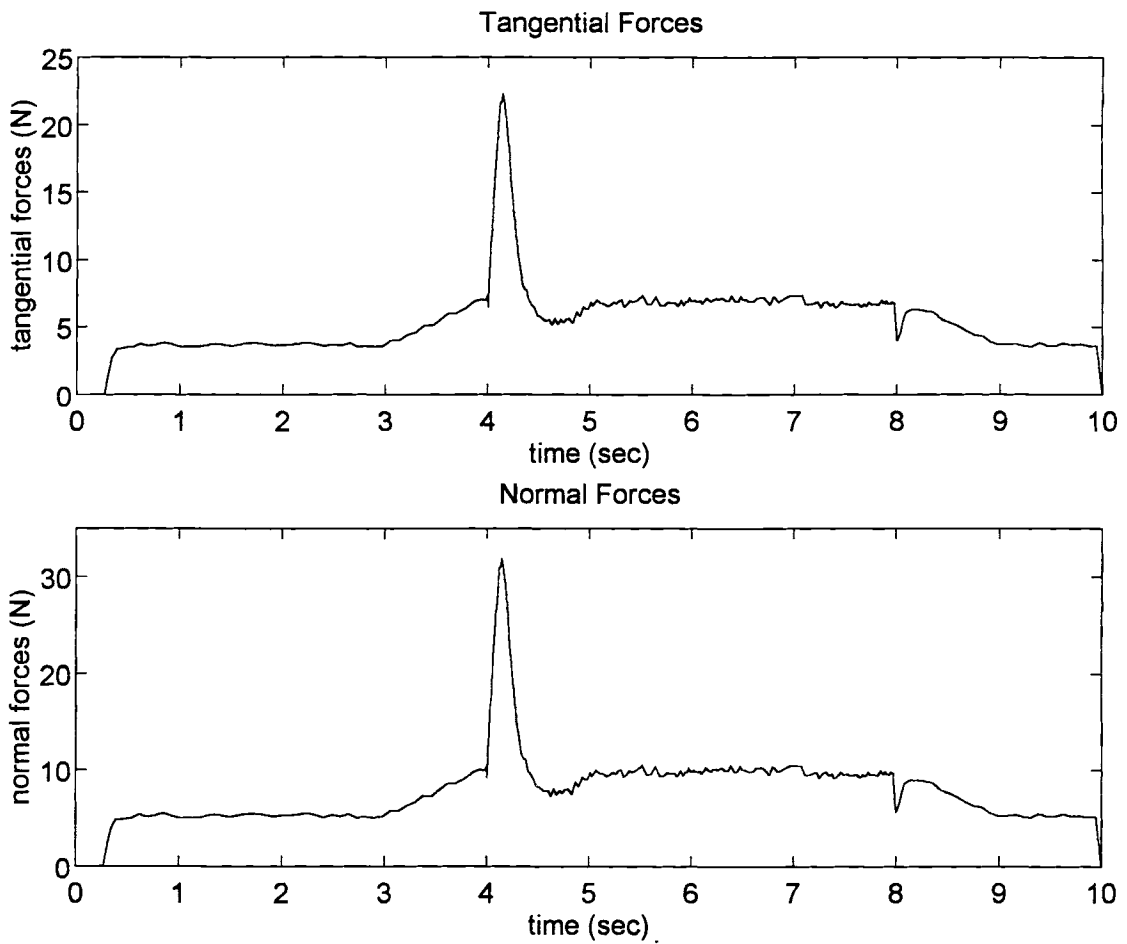


Figure 4.20 Results of Simulation 8 with Simultaneous Position/Force Control:  
(b) Forces

controller. A similar simulation using an impedance controller was conducted, but several hours of simulation time produced no results. We suspect that the dynamics were sufficiently complicated that our Rung-Kutta solver was unable to cope with them.

Simultaneous position/force control was also applied to the scallop-type burrs shown in Figure 4.2b. The results in Figures 4.21 and 4.22 of Simulation 9 show this control approach is also able to achieve good performance for deburring this kind of burr.

Our final simulation was completed to evaluate simultaneous position/force control in deburring a portion of an elliptical curve. For simplicity, in this simulation, commanded inputs were described in reference space because of the small curvature of the desired elliptical contour. Results of Simulation 10 in Figures 4.23 and 4.24 show that this control scheme applied to a curved geometric surface is as effective as when applied to a straight edge contour. The normal and tangential forces in Fig. 4.24 gradually decrease with time because setting desired velocity constant in the  $x$  direction in reference space actually causes the tangential velocity in task space to gradually decrease as the ellipse is traversed from point A to B in Fig. 4.3b.

In summary, our simulation results indicate simultaneous position/force control is effective and superior to impedance or hybrid impedance control. This control scheme can achieve good results in deburring tasks when the normal force is required only to remain below specified limits. In the next chapter, we present recommendations for further work.

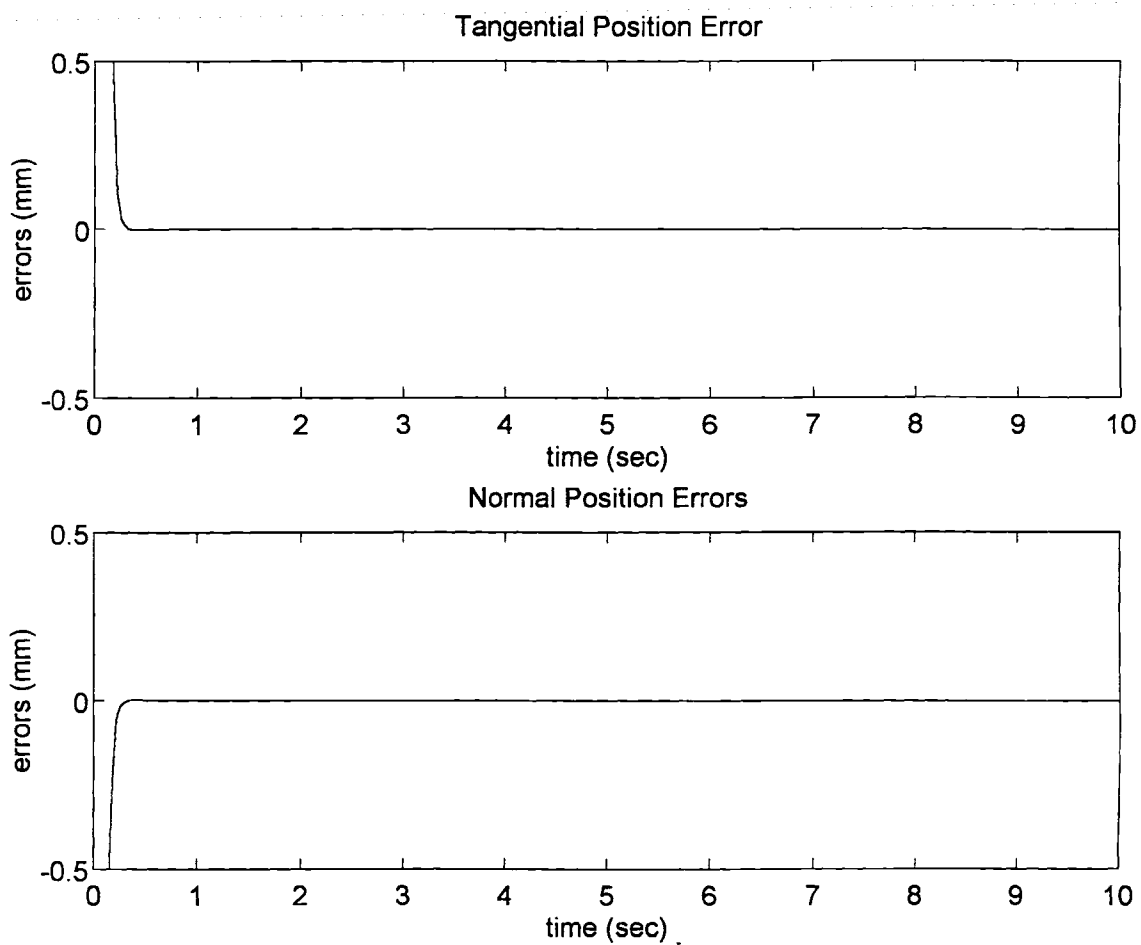


Figure 4.21 Results of Simulation 9 with Simultaneous Position/Force Control:  
(a) Position Error

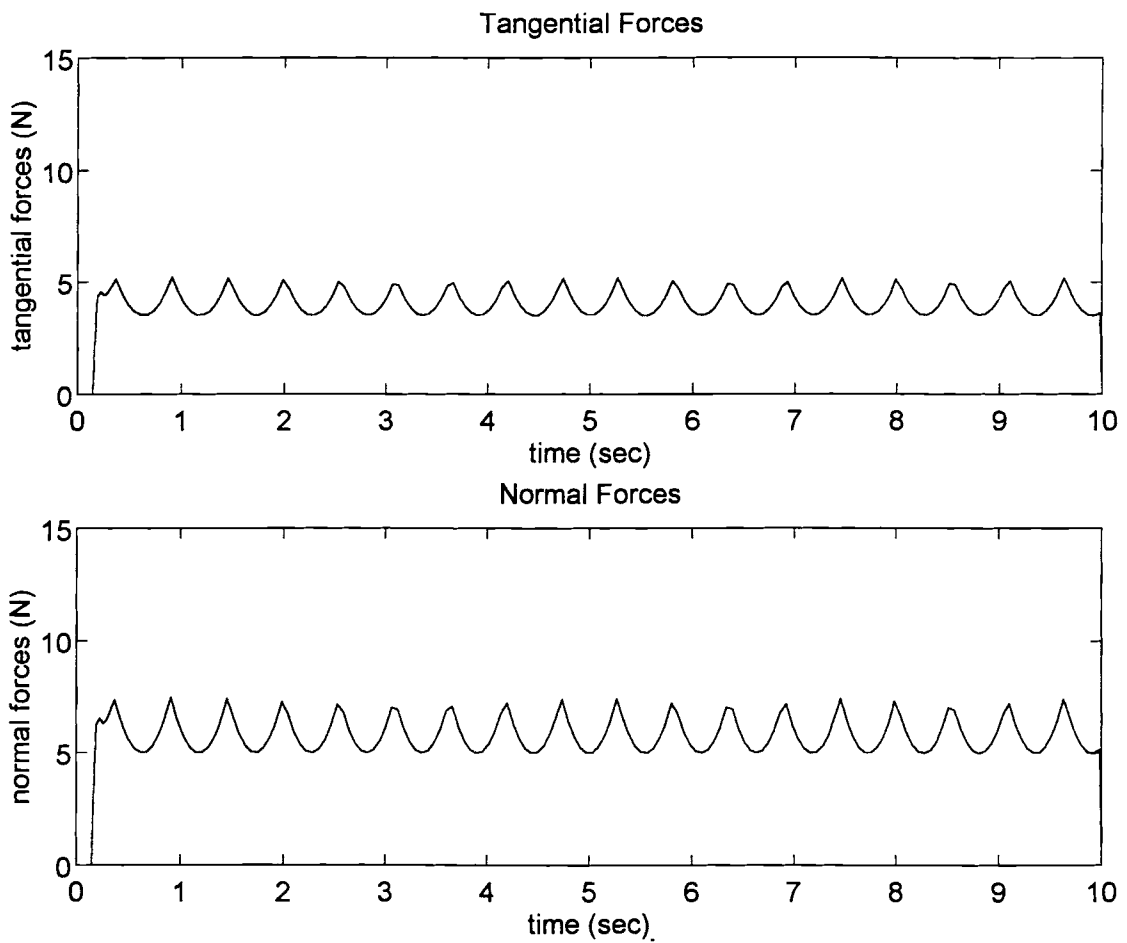


Figure 4.22 Results of Simulation 9 with Simultaneous Position/Force Control:  
(b) Forces

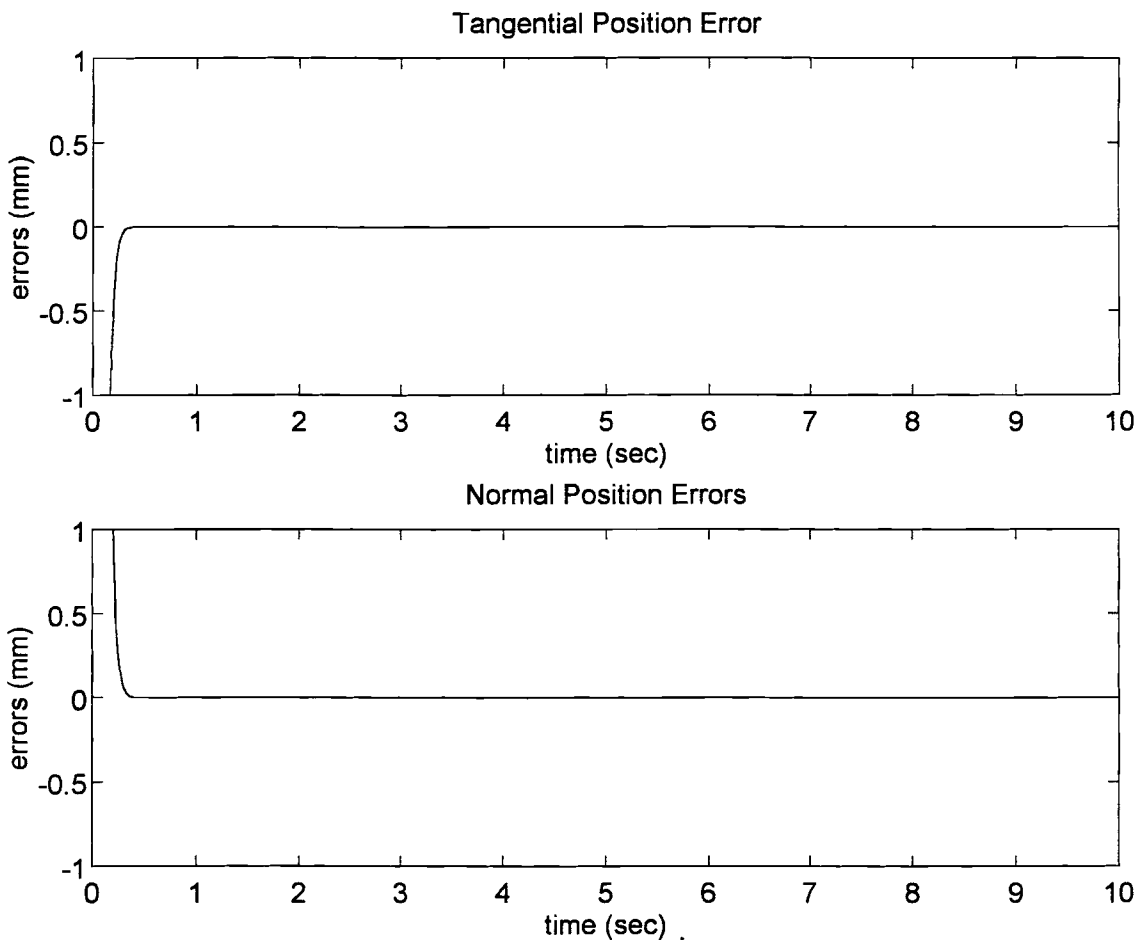


Figure 4.23 Results of Simulation 10 with Simultaneous Position/Force Control:  
(a) Position Error

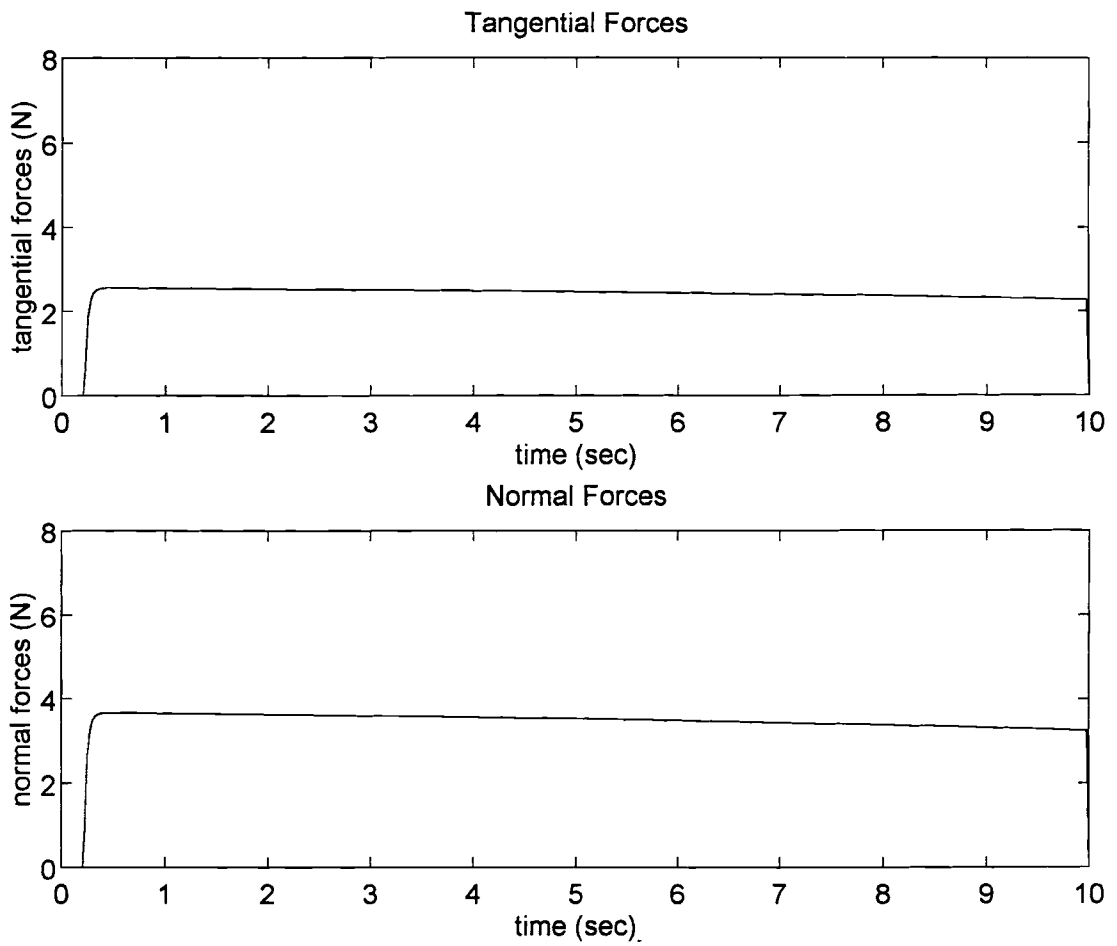


Figure 4.24 Results of Simulation 10 with Simultaneous Position/Force Control:  
(b) Forces

## CHAPTER V

### CONCLUSIONS AND RECOMMENDATIONS

#### Conclusions

We have focused, in this study, on the dynamic modeling and control of robotic deburring and grinding. The major contributions of this thesis are summarized as follows:

1. A relatively accurate model of the interaction force for robotic deburring and grinding was developed based on conventional grinding mechanics. It was shown that the interaction of robotic deburring and grinding can be modeled as a contact task of a robot with a rigid environment. Nonlinear coupling characterizes the dynamic behavior of the interaction between the end effector and its environment. An approximate linearization of the nonlinear relationship between the grinding force and the end effector motion was used to help analysis and understanding of the dynamic behavior of the robotic deburring and grinding process.
2. Mechanical implementation of robotic deburring and grinding involves different tasks. The Jacobian matrix is used to relate the motion of manipulators in different spaces. We developed the 2-dimensional Jacobian matrix between the joint space and the task space of elliptical surfaces for SCARA manipulators. This formulation is necessary to control the SCARA manipulator with complex geometric constraints.

3. A new controller, called simultaneous position and force control, was proposed to effectively control a manipulator contacting a rigid environment. The control scheme was developed based on the analysis of impedance control and hybrid impedance control, and it may be considered either an extension of impedance control or a new version of hybrid impedance control. However, this control strategy offers a more intuitive means to deal with position and force control of manipulators undergoing constrained motions. Using this control method, designers can modulate control between the force-oriented or motion-oriented control by selecting gain values properly.
4. Using simultaneous position and force control, we are able to control robotic deburring and grinding with irregular and unpredictable burrs to achieve good position accuracy under specified, maximum contact forces. This strategy is different from previous work on deburring and grinding, where constant contact forces are desired. The method proposed herein for robotic deburring and grinding is unique in that conventional grinding mechanics is used to model contact forces.
5. Two common control strategies in force control of manipulators, impedance control and hybrid impedance control, were also investigated for robotic deburring and grinding. The results showed that impedance control may achieve good performance for edge-following tasks, which require small contact forces between the end-effector and the environment. Once engaged with deburring and grinding, control of manipulators requires a target impedance integrated with a command force planned carefully. Otherwise, significant position errors occur with this scheme. In contrast, hybrid impedance control provides independent force and position control in two orthogonal directions and results in significant oscillations due to the nonlinear coupling dynamics of the interaction.



## Recommendations

Simulation results have shown that the model and control algorithm developed in this thesis are able to produce successful robotic deburring and grinding. Further investigations following this study are recommended as follows:

1. Investigate the effects of modeling errors and measurement noise on the stability and robustness of the proposed simulations position/force control.
2. Develop experiments to test and verify the results of this research. Sensor dynamics should be considered in further studies so as to achieve more realistic results.
3. Because an accurate model of the dynamics of the interaction between the manipulator and environment during grinding or deburring is difficult, a controller integrated with on-line estimates of material removal parameters and other system parameters, such as masses and inertial moment of the links (include those of the tools), may result in more robust control performance. Adaptive control combined with the control scheme developed in this study may be applied to complete these tasks.
4. Since fuzzy control is known to provide good control of complex, nonlinearly coupled dynamic systems, better performance may be possible if a fuzzy controller is used in a hierarchical structure, together with our proposed controller, to generate desired forces and positions. Accordingly, we recommend investigation of fuzzy control concepts for this problem in further researches.
5. In addition to grinding wheels, other material removal tools may be investigated to achieve good results in deburring various materials.

## REFERENCES

1. Maus, Rex and Allsup, Randall, *Robotics: A Manager's Guide*, John Wiley & Sons 1986.
2. "Pletized Production Pleases People Packing Pepperoni Pizzas," *The Industrial Robot*, vol.19, no.5, pp. 39-40, 1992.
3. Stephan, P., "Robots in the Press Shop," *Robotics Today*, vol.6, no.1, pp. 3-4, 1993.
4. Vaccari, J., "Arc-Welding Robots Reap Large Savings" *American Machinist*. v136, pp. 43-44, 1992.
5. Schreiber, Rita R., "Portrait of a Painting Robot," *Manufacturing Engineering*, vol. 107, pp. 55-59, Nov. 1991.
6. Spong, Mark W. and Vidyasagar, M., *Robot Dynamics and Control*, John Wiley & Sons 1989.
7. Cook, Nathan H., *Manufacturing Analysis*, Addison-Wesley Company 1966.
8. Kramer, B. M., et al., "Robotic Deburring," *Robotics & Computer-Integrated Manufacturing*, vol.1, no. 3/4, pp. 365-374, 1984.
9. Kazerooni, H., Bausch, J. J., and Kramer, B. M., "An Approach to Automated Deburring by Robot Manipulators," *ASME J. Dynam. Sys. Meas. Control*, vol.108, pp.354-359, December1986.
10. Whitney, D. and Nevins, J., "What is the Remote Center Compliance(RCC) and What Can It Do?", *Proceedings of the 9th International Symposium on Robotics*, March 13-15, 1979, Washington D.C., pp135-152.

11. Koelsch, J., "Taking on Tough Burrs," *Manufacturing Engineering*, vol.107, pp.35-38, Oct. 1991.
12. Whitney, Daniel E., "Historical Perspective and State of the Art in Robot Force Control," *The International Journal of Robotic Research*, vol. 6, no.1, 3-14, 1987.
13. Mason, M. T., "Compliance and Force Control for Computer Controlled Manipulators," *IEEE Trans. Syst., Man, Cybern.*, vol. SMC-II, No.6, pp. 418-432, June 1981.
14. Raibert, M., and Craig, J., "Hybrid Position/Force Control of Manipulators," *ASME J. Dynam. Sys. Meas. Control*, vol.102, no. 2, pp.126-133, June 1981.
15. Yoshikawa, T., Sugie, T., and Tanaka, M., "Dynamic Hybrid Position/Force Control of Robot Manipulators -- Controller Design and Experiment," *IEEE J. Robotics and Automation*, vol. 4, no. 6, pp. 699-705, December 1988.
16. Salisbury, J, Kenneth, "Active Stiffness Control of a Manipulator in Cartesian Coordinates," *Proceedings of the 19th IEEE Conference on Decision and Control*, pp. 95-100, December 1980.
17. Whitney, D. E., "Force Feedback Control of Manipulator Fine Motions," *ASME J. Dynam. Sys. Meas. Control*, vol.99, pp.91-97, June 1977.
18. Hogan, N., "Impedance Control: an Approach to Manipulation, Part I: Theory, Part II: Implementation, Part III: Applications," *ASME J. Dynam. Sys. Meas. Control*, vol.107, no.1, pp.1-24, March 1985.
19. Hogan, N., "Stable Execution of Contact Tasks Using Impedance Control," *Proc. IEEE Int. Conf. Robot. Autom.*, pp. 1047-1054, Raleigh NC, March 1987.
20. Hogan, N., "On the Stability of Manipulators Performing Contact Tasks," *IEEE J. Robotics and Automation*, vol.4, no.6, pp. 677-686, December 1988.
21. Kazerooni, H., Sheridan, T., and Houpt, P., "Robust Compliant Motion for Manipulators, Part I: The Fundamental Concepts of Compliant Motion, Part II:

- Design Method," IEEE J. Robot. Automation, vol. RA-2, no.2, pp.83-91, June 1986.
22. Kazerooni, H., "On the Robot Compliant Motion Control," ASME J. Dynam. Sys. Meas. Control, vol.111, pp.416-425, September 1989.
  23. Kazerooni, H., Kim, S., and Waibel, B. J., "Theory and Experiment on the Stability of Robot Compliance Control," ASME Winter Annual Meeting at Chicago, DSC-vol. 11, pp. 87-101, November 1988.
  24. Anderson, R., and Spong, M., "Hybrid Impedance Control of Robotic Manipulators," IEEE J. Robot. Automat., vol. 4, no.5, pp. 549-556, Oct. 1988.
  25. An, C. H., and Hollerbach, J. M., "Dynamic Stability Issues in Force Control of Manipulators," Proceedings of the American Control Conference, pp. 821-825, 1987.
  26. Colgate, E., and Hogan, N., "Robust Control of Dynamically Interacting Systems," Int. J. Control, vol.48, no.1, pp.65-88, 1988.
  27. McCormick, W., and Schwartz, H. M., "An Investigation of Impedance Control for Robot Manipulators," The International Journal of Robotics Research, vol.12, no.5, pp.473-489, 1993.
  28. King, R. I., and Hahn, R. S., "Handbook of Modern Grinding Technology," Chapman and Hall, New York, 1986.
  29. Hahn, R. S., and Lindsay, R. P., "Principles of Grinding," 5 part series in Machinery, July-Nov. 1971.
  30. Craig, John J., *Introduction to Robotics Mechanics & Control*, Addison-Wesley Publishing Company, Inc., 1986.
  31. Kang, C. G., Kao, W. W., Boals, M., and Horowitz, R., "Modeling Identification and Simulation of a Two Link Scara Manipulator," The Winter Annual Meeting of ASME, Chicago. 1988, v11, 393-407.

32. Craig, J. J., Hsu, P, and Sastry, S. S., "Adaptive Control of Mechanical Manipulators," *The International Journal of Robotics Research*, vol.6, no.2, pp.16-28, 1987.
33. Slotine, J.-J. E., and Li, W, "On the Adaptive Control of Robot Manipulators," *The International Journal of Robotics Research*, vol.6, no.3, pp.49-59, 1987.
34. Lucca, D, Private Conversation. Feb., 1995.
35. Graf, T. L., "Deburring, Finishing and Grinding with Robots," *SME Machining Technology*, vol. 5, no. 3, pp. 1-7, 1994.
36. *MATLAB Reference Guide*. (1992). Natick, Mass.: The Math Works, Inc.

## **VITA**

**Duli Hong**

Candidate for the Degree of

Master of Science

**Thesis: POSITION/FORCE CONTROL OF MANIPULATORS USED FOR  
DEBURRING AND GRINDING**

**Major Field: Mechanical Engineering**

**Biographical:**

**Personal Data:** Born in Jiazhi, Guangdong, China, August 6, 1963, the son of Xiangyou Hong and Yuqiong Fang.

**Education:** Graduated from Jiazhi High School, Guangdong, China, in July 1979; received a diploma in Mechanical Engineering from Nanjin Navigation Engineering College, Nanjin, China, in July 1982; received Master of Science Degree in Mechanical Engineering in Chongqing University, Chongqing, China, in April 1988; completed requirements for the Master of Science Degree at Oklahoma State University in May 1995.

**Professional Experience:** Mechanical Engineer, Guangzhou Mechanical & Electrical Engineering company, Guangzhou, China, from August, 1982, to August, 1985; Project Engineer, Guangzhou M&E Equipment Tendering Corp., Guangzhou, China, from May, 1988, to December, 1992; Graduate Research Assistant, Department of Mechanical Engineering, Oklahoma State University, from September, 1993, to May, 1995.